UNIVERSITY OF OKLAHOMA

GRADUATE COLLEGE

PROGRESS TOWARDS PRODUCING AND TRAPPING COLD NITRIC OXIDE

A DISSERTATION

SUBMITTED TO THE GRADUATE FACULTY

in partial fulfillment of the requirements for the

Degree of

DOCTOR OF PHILOSOPHY

By

PARSHURAM DAHAL
Norman, Oklahoma
2012

PROGRESS TOWADS PRODUCING AND TRAPPING COLD NITRIC OXIDE

A DISSERTATION APPROVED FOR THE
HOMER L. DODGE DEPARTMENT OF PHYSICS AND ASTRONOMY

BY

_____
Dr. Eric. R. I. Abraham, Chair

_____
Dr. Neil E. Shafer- Ray

_____
Dr. Deborah Watson

_____
Dr. John Furneaux

_____
Dr. John Albert

© Copyright by PARSHURAM DAHAL , 2012
All Rights Reserved.

This dissertation is dedicated to my loving mother, who always encouraged me to pursue higher education and dedicated her life for my future. With her help, support, and encouragement, I am here today.

Acknowledgements

This thesis is the end of my long journey started from Nepal in obtaining my Ph.D. degree in experimental Atomic, Molecular and Optical (AMO) Physics. There are some people who made this journey easier and successful. First and foremost, I want to offer my sincerest gratitude to my supervisor Eric Abraham who has guided me throughout my thesis with his patience and knowledge. He also allowed me to use his lab to work independently. I would like to appreciate his contributions of time, ideas, motivation and funding to make my graduate student life productive and stimulating. I would also like to thank to Dr. Neil Shafer-Ray for his constant encouragement and effort and without his help, this thesis would not have been completed or written in this shape. I would like to thank Prof. John Furneaux for his great help during my activated carbon experiment, who guided me in the initial setup process of experiment. My sincere gratitude also goes to rest of my Ph.D. committee, Prof. Deborah Watson, and Prof. John Albert (Department of matematics) for their willingness to be in my committee. I would like to thank all my professors at The University of Oklahoma, Depatment of Physics and Astronomy.

I would also like to gratefully acknowledge the support, encouragement, friendship and help of some special individuals such as Dr. Jason Alexander, James Coker, Thomas Akin, Dr. Priyanka Milinda Rupasinghe, Dr. Sivakumar Poopalasingham, and Dr. Christopher McRaven. I would also like to acknowledge the machine shop staff such as Joel Young, Barry Bergeron, Sean Attebury in the machine shop for designing and building our magnetic trap experimental apparatus. I would also like to thank

Adrienne Wade in the electronic shop for providing me a much better environment to work there. I would also like to acknowledge office staff Danette Loyd, Debbie Barnhill, Bill See, and Sharon Widner.

I would like to thank my parents especially my mother, my sisters and my brothers who have always supported me and encouraged me during my educational life. I would like to thank my children, Prasamsha and Prajwal, for playing with me during my Ph.D work. I am indebted to my loving wife for her encouragement and dedication in my life. Finally, I would like to thank all of my relatives, friends, brothers and sisters, and villagers in Nepal for their unforgettable encouragement during my high school and higher level study.

Table of Contents

List of Tables

List of Figures

Abstract

I present the experimental results of a new source of cold molecular production using activated carbon and the design of the necessary apparatus. This new source may eliminate the need for laser ablation loading in buffer gas cooling experiments. I also analyze the relative signal amplitude of rotational lines of cold Nitric Oxide (NO) molecules in its lower fine structure state. Experimental results showing the effects of the hexapole velocity filter on the production of lowest ro-vibrational low field seeking states of a cold molecular sample of NO is also discussed. The sample is produced by the extraction of the cold fraction of the Maxwell-Boltzman distribution of a thermal source.

I also present a computer simulation method for filtering, guiding and magnetic trapping of cold molecular NO. In the filtering process, the low field electric seeking molecules interact with an inhomogeneous electrostatic field of a hexapole guide which is exploited to select the slow molecules from a cold molecular source. Given my computer simulation work, I assert that the resulting cold fraction in the non-magnetic $^2\Pi_{1/2}$ ground state can be directed into a permanent magnetic trap where it could be optically pumped into the $^2\Pi_{3/2}$ fine structure state which can be magnetically trapped. I present the full simulation of the procedure and progress toward getting experimental results regarding the magnetic trapping of NO.

Chapter 1

General introduction

Cooling of atoms/molecules is the compressing of the velocity distribution and suppression of the phase space density. The phase space density is defined by $n\lambda^3$, where n is the number density and the λ is the de Broglie wave length. It is given by the relation Eq.(1.1) for the atom of mass m and temperature T.

$$\lambda = \frac{\hbar\sqrt{2\pi}}{\sqrt{mk_BT}} \tag{1.1}$$

Where $\hbar$ is the Planck constant and k_B is the Boltzmann constant. With ultra-cold atoms, Bose-Einstein condensate occurs when $n\lambda^3 \gg 2.612$[2] for spin-zero particles confined in a box. On the other hand, for an ideal Bose gas, $n\lambda^3 \gg 1$.

The field of atomic and molecular physics has been advanced since the invention of the laser in the 1960s. With the help of the laser, physicists could probe internal studies of matter with better precision. Cooling and trapping are the techniques that have enabled the scientists to achieve very low temperatures and high phase-space densities, which lead to a revolution in atomic and molecular physics. By cooling and trapping particles in a particular region of space, physicists can study and control them for further study. Because of this, cooling and trapping processes led to innovative experiments in experimental physics such as the observation of Bose-Einstein condensation [3], Fermi degeneracy in a gas[4], super fluidity in atomic vapors[5], and atom lasers[6]. The trapping and cooling of atoms/molecules is important to open up for advanced ultra-cold atomic/molecular spectroscopy. Molecules are not spherical,

and they have both rotational and vibrational degrees of freedom. They also have both even and odd electric and magnetic multipole moments. Dense samples of cold molecules have been obtained since the 1990s using methods such as, direct cooling and electric trapping of polar molecules [7], photoassociated laser-cooled atoms in a magneto-optical trap [8], molecule formation by magnetic Feshbach resonances in an optical dipole trap [9], and others [10, 11, 12, 13, 14, 15, 16, 17, 18]. We will describe some of the cooling and trapping methods of atoms and molecules in the following sections.

1.1 The production of cold atoms

1.1.1 Laser cooling

Laser cooling is the most widely used process of cooling neutral atoms. Laser cooling is commonly used to prepare atoms for magnetic trapping[19, 20]. Laser-cooled atoms can be used to provide a high-intensity and low velocity source of neutral atoms for a wide variety of atomic physics experiments. In laser cooling, nearly resonance laser light from an atomic transition illuminates an atom. If the light frequency is below the natural atomic resonance frequency, the Doppler shift will cause hot atoms to absorb counter - propagating photons. Since the emission of photons is random, the net effect is that the momentum of the atom is reduced and thus cooling the atoms. Laser cooling has been used to load a number of species into magnetic traps, and has become the most important tool for low temperature atomic physics. Because of the complicated rotational and vibrational internal structure of molecules, the laser

cooling process is very hard to use to cool molecules. The laser cooled atoms are those which have the simplest energy level structures such as the alkali metals, metastable noble gases, and all alkaline-earth-metal atoms. Also, because of the inelastic collisions between ground state and excited - state atoms, the number and density of atoms obtainable through laser cooling is limited. Laser cooling and trapping allow the preparation of cold atoms at a range of μK with density of $10^{10} cm^{-3}$, where K is kelvin.

1.1.2 Buffer-gas cooling

Cooling by collisions with a gas is a common cooling method to produce cold atoms and molecules that depend on elastic collisions between a hot sample of atoms/molecules and a cold gas. The sample of the atoms/molecules to be cooled are seeded into the helium gas and are introduced into a pressurized, room temperature auxiliary gas and forced through a nozzle to expand into vacuum to promote cooling. The cooling depends on the carrier gas such as He, Ne or Ar. Rotation and vibration freedom of molecules are also cooled during expansion. It is not useful for trapping experiments because additional beam is required to slow and trap the beam [21, 22, 23, 24].

A atomic or molecular gas can be cooled by bringing into thermal contact with something else that is already cold. Buffer-gas cooling is the most general cooling process that is carried out with the thermalization of atomic and molecular species with cold buffer gas. The molecules of interest are produced by laser ablation of a suitable precursor target inside a buffer gas cell containing helium gas at low temperature.

The particles are then allowed to escape through a hole in the wall of the cell and transported to an experiment where they are guided or trapped. This technique can produce high fluxes of low speed cold atoms/molecules. This process is a good starting point to further cooling of the species by other techniques, such as evaporative cooling. The first experiment of this process for CaH was done in 1998 [25]. Also, Doyle *et al* has successfully applied the buffer-gas method in order to trap atomic chromium and europium [10, 11] as well as several other atoms [26]. They have also applied buffer-gas cooling to VO and PbO [27] molecules. Almost all buffer gas cooling groups produced the molecules or atoms by laser ablation from a solid precursor. These groups directed and tightly focused the laser light pulses onto the precursor solid targets. The solid targets were glued to the top of the buffer-gas cell. After ablation, the molecules or atoms are cooled by the helium buffer-gas atoms by thermalization. These groups use ^{3}He or ^{4}He because it has a higher vapor pressure at the temperature of T<1 K. This process has been used in a number of studies as it is used to cool paramagnetic species and to load them into a magnetic trap.

1.1.3 Evaporative cooling

All current experiments that have produced degenerate quantum gases have used evaporative cooling. Evaporative cooling helps in gaining the phase space density. Evaporative cooling of a magnetically trapped atomic sample was first considered by [12] and it was experimentally demonstrated in 1988 taking spin-polarized atomic Hydrogen [13]. In a trapped ensemble of atoms in thermal equilibrium, the energy

distribution is given by the Boltzmann distribution. In evaporative cooling, like cooling in a cup of tea, the high-energy tail of the thermal distribution is continuously removed and the remaining atoms/molecules would relax by elastic collisions in order to be in thermodynamic equilibrium. There are no dissipative external forces to cool the particles. The efficiency of evaporative cooling is a function of elastic and inelastic scattering rates between the trapped atoms/molecules. Elastic collisions help to attain equilibrium while inelastic collisions lead to the loss of atoms and increase the temperature of the trapped atoms. As a result, the remaining particles in the trap shifted to lower energies. The evaporation time depends on the duration of the thermalization, elastic collision rate, the density, and on the trap depth compared to the energy of the trapped gas. In a magnetic trap, the ratio of the elastic and elastic collision rates determines the success or failure of getting quantum degeneracy using evaporative cooling. Evaporative cooling is applied to a laser-cooled atomic sample in experiments that led to Bose-Einstein condensation [3, 28, 29]

1.2 The production of cold molecules

There are two distinct approaches to the production of cold molecules. The indirect methods are the generation of cold molecules from cold atoms through photoassociation and using Feshbach resonances. The direct approach works to cool molecules that are initially hot (room temperature) are Stark deceleration and buffer gas cooling. Velocity filtering is the selection of the cold molecules from the thermal distribution. The buffer gas cooling is already described above. In the following sections, rests of

these methods are described briefly.

1.2.1 Photoassociation

Photoassociation (PA) is the process in which two colliding cold atoms in a dense and cold atomic cloud absorb a photon of the right frequency to form an excited molecule[30, 31, 32, 33, 34]. This process was first suggested in [35]. The excited state molecules may decay to one or more ro-vibrational ground state by spontaneous emission or stimulated by laser fields. PA spectroscopic studies have been performed for all alkali atoms from Li to Cs, where the first studies were for Na_2 [30] and Rb_2 [36]. The PA spectroscopy explores molecular dynamics at distances well beyond those usually associated with chemical bonds. PA process not only offers techniques for molecular spectroscopy, but it also allows us to form ultra-cold molecules in the ground-state [32]. Polar molecules such as KRb, NaCs, RbCs and LiCs were also created by photoassociation using two species clouds of ultra-cold atoms[37, 38, 39, 40, 41, 42]. But, these photoassociated molecules populate many electronic ground rovibrational states by spontaneous decay. A laser stimulated transfer scheme was employed by [43, 44] to achieve cold molecules in a single rovibrational state.

1.2.2 Stark deceleration

To control a polar molecule's motion, the force due to the interaction of a dipole with an inhomogeneous electric field [45] is used. This force provides the means to alter the velocity of polar molecules and to simultaneously select the molecular internal

states. Stark deceleration was first implemented by the Meijer group in 1999 with the deceleration of CO [14, 15]. In this process, the time dependent inhomogeneous fields generated by a series of high-voltage electrodes, which are switched on and off in a dedicated timing sequence, is used to repetitively alter the Stark potential energy of the low- field seeking (LFS) states [15, 46]. In this process, the potential energy and thus the kinetic energy is decreased at each decelerator stage.

As the molecules are decelerated over 63 synchronously pulsed electric field stages [15], the decelerated beam is obtained. Transverse focusing and transverse stability is also guaranteed for the molecules moving synchronously with the switching of the electrodes. Decelerated and slowed molecules have been loaded into an electric trap [7, 47], into a storage ring [48] or a molecular synchrotron [49, 50].

1.2.3 Velocity filtering

New methods are being developed to produce the cold samples of polar molecules as the laser cooling of molecules is impossible in general because of their complex rovibrational structure. The first effort to produce slow cold polar molecules were made by Zacharias *etal* in the 1950s in which the effusive molecular beams were directed upwards like a fountain [51, 52]. It was expected that slow molecules reverse their direction of travel after ascending a small height because of the gravitational field. But no slow molecules were detected at the base of the fountain because of two reasons. (1)After leaving the effusive source, the beams were diluted by spreading out in large solid angles so that the density of the slow molecules at the detector was very

small. (2)The slow molecules were bombarded by the fast molecules from behind so that slow molecules gain so much energy and the momentum in the forward direction that almost no molecules come back to the detector. Despite this result, it is possible to obtain slow molecules by velocity filtering. Latters, strong permanent magnets were used to efficiently guide slow lithium atoms from the distribution of atoms that provide the cheap source of slow atom[53]. The electric guides can be used for velocity filtering and guiding cold polar molecules.

The demonstration of the velocity filtering was done for the molecules such as formaldehyde (H_2CO) and deuterated ammonia (ND_3)[16, 17]. The flux of low field seeking molecules was 10^{10}/sec and peak density of $10^9/cm^3$ was achieved at the guiding field of 100kV/cm. To extend the velocity-filtering technique to molecules in high-field-seeking states, the electric guide is switched between two dipolar configurations in a periodic manner so that molecules in low-field seeking and high-field-seeking states can simultaneously be trapped in a time-averaged potential. It was shown experimentally that guiding of polar molecules in such alternating electric fields is possible [16]. An electric trap for neutral rubidium atoms was set up to show that high field seekers can actually be trapped by alternating fields [54]. Using electrostatic-guiding and velocity-filtering technique, cold guided beams of deuterated water (D_2O) was produced [55]. Recently, these methods of velocity filtering and guiding was extended to include all the water isotopologues H_2O, D_2O and HDO[56]. Filtering on longitudinal velocity was carried out by bending the guide. Transnationally cold and slow ND_3 was prepared by filtering the slow molecules using a curved electrostatic

hexapole guide combined with a straight hexapole guide, and independent high-voltage supplies are employed to allow for velocity filtering [57]. The Rempe's group at Max-Planck Institute [16, 17, 54, 55, 56] used a quadrupole field to extract slow molecules from a room temperature source. Since this technique is central to this dissertation, it will be explained in more detail in chapter 4.

1.3 Trapping atoms/molecules

To study the properties and interactions of molecules, they need to be trapped. Traps allow long interaction times as well as high resolution for spectroscopic and other types of measurements. A system needs to meet two requirements in order to be a trap. First, the force on the molecules needs to be nearly zero in the center of the trap and second, for small displacements the force has to restore the molecules towards the center of the trap. This force is generated only if the internal energy levels of the molecules are changed as a function of position. Shifting the energy levels takes place because of the Zeeman Effect and the Stark effect in which the molecules interact with a magnetic/electric external field. Using static inhomogeneous electric and magnetic fields, traps for neutral molecules can be formed. In these traps, low-field seekers experience a force toward the center of the trap where the field has a minimum value.

1.3.1 AC trap

An example of an AC electric trap is described in [47]. The trap is loaded by slow molecules from a Stark decelerator. In this implementation, using a microwave pulse,

the molecules are pumped into the high-field seeking state (the ground state of para-ammonia). They also studied the stability of the AC electric trap as a function of switching frequency. They also characterized the spatial distribution and temperature of the trapped cloud of molecules. Gerard Meijer's group was the first to demonstrate AC electric trapping of molecules using ND_3 [58]. The trap depth was 5 mK and the trap volume was $20mm^3$. Since Maxwell's equations do not allow a maximum of the electric/magnetic field in free space, polar molecules in high-field seeking states cannot be trapped in static traps. It is possible to generate an electric field that has a saddle point by superposing an inhomogeneous electric field to a homogeneous electric field. Molecules are focused along one direction, while being defocused along the other. The focusing and defocusing directions can be reversed by reversing the direction of the inhomogeneous electric field. A net focusing force in all directions can be produced when the fields are being switched back and forth at the appropriate rate. Since the ground state of a system is always lowered by an external perturbation, the absolute ground state of any molecule is high-field seeking. Trap loss due to inelastic collisions is absent in the ground state so that it is possible to cool these molecules further using evaporative or sympathetic cooling.

1.3.2 Magnetic trap

There has been rapid progress in techniques for trapping neutral particles in order to attain higher densities and lower temperatures[18, 59, 60, 20, 6]. Electrons, protons, neutrons, and electrons all have intrinsic magnetic moments. As a result, magnetic

field gradients can be used to exert forces on these particles. In the case of atoms and molecules, the overall magnetic moment of the particle is due to the combination of the intrinsic moments of the constituents as well as a contribution from the electron's orbital angular momenta.

When a particle moves in the inhomogeneous field of a magnetic trap, low field seeking particle experiences a slowly rotating magnetic field and the particles precess around the local direction of the magnetic field. This is called adiabatic approximation. The adiabatic approximation holds whenever $\omega_L = \frac{\mu_B.B}{\hbar} >> \frac{d\theta}{dt}$, where B is the magnetic field, μ_B is Bohr's magneton, $\frac{\mu_B.B}{\hbar}$ is Larmor precession frequency, θ is the angle between the magnetic dipole and the electric field lines, and $\frac{d\theta}{dt}$ is the rate of change of the direction of the magnetic field. At this condition, on average, the low field seeking particle's magnetic moment points' antiparallel to the local magnetic field lines. When the strength of the magnetic field has a minimum at the center of the trap, the potential becomes attractive near that minimum for low field seeking particles, and the potential acts as a magnetic trap. If the minimum in B (= 0) field in the center of the trap, the Larmor precession frequency of the particle passing through the zero is less than the orbital frequency so that the spin flip transition from low field trapping state to high field seeking untapped state is very large. This is called Majorana transition. Majorana transitions cause trap loss. Trap losses limit the lifetime of atoms/molecules in the trap. To prevent Larmor frequency of becoming zero, resulting in Majorana transitions, most magnetostatic traps include a bias field, so that the effective potential possesses a nonvanishing minimum at the center of the

trap. We have a quadrupole permanent magnets trap where the field is zero at the center of the trap. The magnetic trapping will be explained in more detail in chapter 5.

Chapter 2

Properties of molecular NO

2.1 Structure of diatomic molecules

Atomic electronic states are described using spectroscopic notations: s, p, d etc. that denotes electrons with orbital angular momentum quantum numbers corresponding to $l = 0$, 1, 2 etc. respectively. The component of orbital angular momentum along a quantization direction has a quantum number, m_l, where $m_l = l$, $l-1$, $l-2$, ... $-l$. Atomic states are commonly described using a spectroscopic notation: $^{2S+1}L_J$, where S is the total spin quantum number and L is the total orbital angular momentum quantum number given by Eqs.(2.1) and (2.2)

$$S = \sum_{i=1}^{N} s_i \tag{2.1}$$

$$L = \sum_{i=1}^{N} l_i \tag{2.2}$$

where s_i and l_i are the spin and orbital angular momentum of each individual electron respectively, 2S+1 is the spin multiplicity, and J is the total angular momentum quantum number. For each spin state S, there are 2S+1 different sub states with different energies. The symbols for L = 0, 1, 2, 3 are denoted by S, P, D, F respectively.

The electric field from the pair of nuclei is a cylindrically symmetric field in diatomic molecules. The molecular electrons are not moving in the spherically symmetric field. Their total angular momenta are not conserved. Since the electrons are moving in the cylindrically symmetrical field and there is no torque on the electrons about the

axis, the projection of the electron angular momentum along the inter-nuclear axis is conserved. The internal structure of the molecules is more complex than the atoms because of more complicated vibrational and rotational structures. Because of the large differences in mass between the nuclei and the electron, the nuclear motion and the electronic motion can be treated independently.

The spectroscopic notation of molecules uses Greek letters to represent the absolute value of the projection of the total orbital angular momentum L onto the inter-nuclear axis. The quantum number that represents this notation is Λ, where Λ=0, 1, 2, 3 correspond to $\Sigma, \Pi, \Delta, \Phi$ molecular states. For $\Lambda \neq 0$ states, molecular states which change sign under reflection in a plane containing the nuclei is denoted with -, those that do not change sign are assigned +. Both Eigen functions have the same energy. So, the electronic term with $\Lambda \neq 0$ are doubly degenerate. Each value of the energy corresponds to two states differing in direction of the projection of the orbital angular momentum along the inter-nuclear axis. For $\Lambda = 0$, the Σ state is non-degenerate. We can distinguish Σ^+ for which the wave function is left unchanged and Σ^- states for which the wave function is changed under reflection in a plane containing the nuclei. For homonuclear diatomic molecules, there is an extra symmetry. The index g or u denotes the existence of a center of symmetry at the midpoint of the distance between the two nuclei, and indicates the parity of the total wave function. States of even parity with respect to inversion are denoted g for gerade states and states of odd parity is denoted by u for ungerade states. The ground state is often labeled by the symbol X. Excited states of the same multiplicity as the ground states are usually

distinguished by the symbols A, B, C...

2.1.1 Hund's coupling cases

The absolute value of the projection of the total electronic angular momentum (spin plus orbital) on the inter-nuclear axis is denoted by Ω. For $\Lambda \neq 0$ states, the molecules have a magnetic field along the inter-nuclear axis so that spin can precess around the axis. The quantum number Σ is the projection of S onto the inter-nuclear axis. it has the value given by $\Sigma = -S, -S+1, -S+2, ...S$. So, in diatomic molecules, the spectroscopic notation for electronic term is ${}^{2S+1}\Lambda^{\pm}_{\Omega}$ where Ω is given by $|\Lambda + \Sigma|$. And the complete spectroscopic notation for homo-nuclear molecule is ${}^{2S+1}\Lambda^{\pm}_{\Omega\,\frac{g}{u}}$. For diatomic molecules with non-zero spin S, the molecules are classified by a system known as Hund's cases. Hund's coupling cases classifies the molecules by the strength of the coupling of certain angular momenta of the molecule. Different electronic terms fall into different Hund's cases. Also, some molecules have electronic terms that fall into an intermediate case.

Hund's case (a)

In Hund's case (a) shown in Figure 2.1, the interaction of the nuclear rotation with the electronic motion both spin as well as orbital is very weak but the electronic motion itself is coupled very strongly to the inter-nuclear axis. The electrostatic interaction has axial symmetry because of which $\vec{L}$ precess about the inter-nuclear axis with well-defined component $\vec{\Lambda}$. Since the spin orbit interaction is larger compared

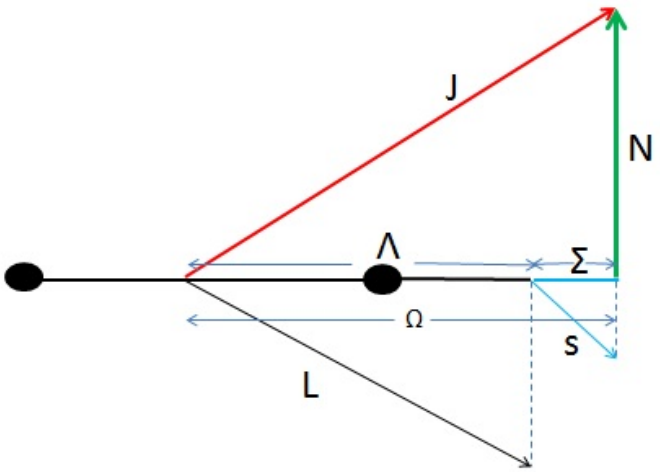

Figure 2.1: Hund's case (a)

to the rotational energy, the spin angular momentum $\vec{S}$ also precesses around the inter-nuclear axis with well-defined component $\vec{\Sigma}$. Then $\vec{\Omega}$=$\vec{\Lambda}$+$\vec{\Sigma}$. It means the sum of the two projections gives the total angular momentum of the electrons which takes the values given by

$$\Omega = \Lambda + \Sigma, \Lambda + \Sigma - 1, \Lambda + \Sigma - 2, ...\Lambda - \Sigma \tag{2.3}$$

Ω is integral or half integral depending on whether the number of electrons is even or odd. Angular momentum $\vec{N}$ of the nuclei rotation couple with $\vec{\Omega}$ to form total angular momentum vector $\vec{J}$. J cannot be less than its components Ω. So for a Ω, J = Ω, Ω+1, Ω+2,...levels but J < Ω never occurs.

Hund's case (b)

When $\Lambda = 0$ and S is not equal to 0, the spin vector $\vec{S}$ is not coupled to the inter-nuclear axis at all so that $\vec{\Omega}$ is not defined. Also, in this case as shown in Figure 2.2,

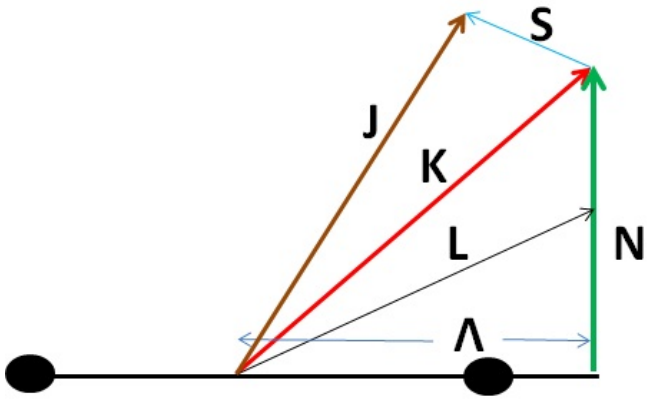

Figure 2.2: Hund's case (b)

the component of the total electron spin along the inter-nuclear axis, Σ, is not well defined. The total angular momentum quantum number apart from spin is denoted by N and rotational levels with the same value of N lie close together in energy. The total angular momentum quantum number is $J = N + S$. In Hund's case (b), vector $\vec{L}$ precesses about inter-nuclear axis with a well-defined component Λ along inter-nuclear axis , $\vec{N}$ couples with $\vec{\Lambda}$ to form $\vec{K}$. This $\vec{K}$ couples with $\vec{S}$ to form $\vec{J}$ as shown in Figure 2.2. The quantum number for K is given by

$$K = \Lambda, \Lambda + 1, \Lambda + 2, ... \tag{2.4}$$

where K is the total angular momentum without spin. If Λ =0, the angular momentum K is identical with $\vec{N}$ and K is perpendicular to the inter-nuclear axis. The possible value of J for a given K is given by

$$J = (K + S), (K + S - 1), (K + S - 2), (K + S - 3), (K + S - 4), ... |K - S| \tag{2.5}$$

Except J < S, each level with a given K consists of 2S + 1 components. J is a half integer for an odd number of electrons and is an integral for an even number of

electrons.

2.2 NO molecule

The NO molecule was chosen for the experiments because NO was studied thoroughly and has a well characterized spectroscopy having a well-established, sensitive detection scheme. NO is a polar molecule with large enough electric dipole moment. It is also a paramagnetic molecule with magnetic dipole moment of 1 Bohr magneton of $^2\Pi_{3/2}$ state at lower rotational quantum numbers. Magnetic traps make use of this quality. The electric dipole moment of ground vibrational state has been determined experimentally to be approximately 0.15 Debye (1 Debye = 3.336×10^{-30} cm). The freezing point of NO is 110.8 K. NO has a high-vapor pressure. At 54K, the vapor pressure of NO is 10^{-6} torr. Thus, NO can be cooled well below 100 K and still be a practical source for the experiments. The ionization energy of NO is $74607.7cm^{-1}$. NO is a stable molecule which has an electron configuration of $1\sigma^2 2\sigma^2 3\sigma^2 4\sigma^2 5\sigma^2 1\pi^4 2\Pi$, where the letters are the various electron orbitals similar to the description of atoms.

Because of the unpaired electron in NO, it possesses both S and L in its electronic ground state. $\Sigma_s = \pm 1/2$ and $\Lambda = 1$ for a Π ground electronic state and $\Sigma_s = \pm 1/2$ and $\Lambda = 0$ for a singly Σ excited state. The coupling of the total electronic spin Σ_s and the total angular momenta Λ are strong, represented by a total angular momentum vector Ω lying along the inter-nuclear axis which is given by $\Omega = |\Lambda + \Sigma_s|$. The inter-nuclear axis component of the total electronic angular momentum can thus take the value $\Omega = 1/2, 3/2$. The two components $^2\Pi_{1/2}$ and $^2\Pi_{3/2}$ of the NO molecule are

due to a spin-orbit interaction. $^2\Pi_{3/2}$ state has an energy $123cm^{-1}$ above than the $^2\Pi_{1/2}$ state. For multiplet states with $\Lambda \neq 0$, there is a further splitting in addition to the spin-splitting described above. This is due to the two directions possible for the electron orbital angular momentum Λ along the inter-nuclear axis. In the presence of rotation, the degeneracy between the two directions is broken and each rotational level is split into components with positive or negative parity. This is known as Λ-type (or parity) doubling. At low values of J, the coupling is described by Hund's case (a). As J increases, the spin-splitting decreases and the coupling goes towards Hund's case (b).

The total angular momentum J is quantized along the direction of the magnetic field as shown in Figure 2.3. We can evaluate the projection of J on magnetic field and the projection of Ω on J. The rotational contribution to the magnetic moment is relatively small so it is neglected here. Geometrically from Figure 2.3, the projection-of the magnetic dipole moment in the magnetic field direction is given by

$$\mu_B = \frac{(\Lambda + 2\Sigma)(\Lambda + \Sigma)M_J}{J(J+1)} \tag{2.6}$$

For the $^2\Pi_{3/2}$ state, the Zeeman effect is much more pronounced because of the addition of the projection of electronic orbital and the spin magnetic moments giving magnetic dipole moments. The magnetic dipole moment decreases with increase in rotational quantum number. But for the $^2\Pi_{1/2}$ state, the Zeeman effect is much smaller because the projection of electron orbital and the spin magnetic moment cancel each other.

As the rotational angular momentum N and J increase, the spin decouples from

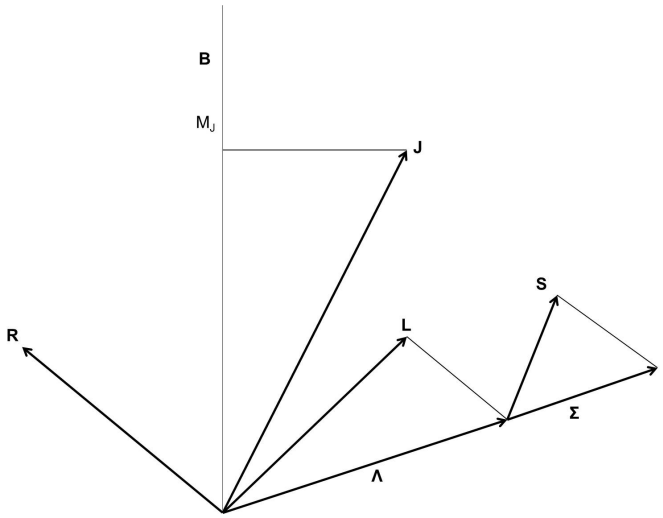

Figure 2.3: The precession of J along the magnetic field direction in Hund's case (a)

the inter-nuclear axis and interacts with the rotational angular momentum, N. The decoupling of the S at higher values is taken as mixing of the two electronic states. This means the $^2\Pi_{1/2}$ state gains magnetic moment at the expense of the $^2\Pi_{3/2}$ state, so that NO is paramagnetic in both ground states at higher J. The first excited state of NO is $A^2\Sigma^+$. The nuclear magnetic moment of NO is associated with the presence of nitrogen atoms in which the nuclear spin $\vec{I}$ couples to the angular momentum vector $\vec{J}$ to give the resultant $\vec{F}$. This vector $\vec{F}$ can take values J+I, J+1-1, J+I-2,...$|J - I|$. As each combination has slightly different energy, Λ doublet components are split into hyperfine patterns. The nucleus of nitrogen has a spin $\vec{I}$ of 1, each magnetic sublevel divided into 2I+1=3 hyperfine levels. The hyperfine splitting is due to the interaction of both the magnetic moment as well as the electric quadrupole moment of the nitrogen nucleus with the electrons.

2.3 Calculation of NO molecular transition energy

2.3.1 $X^2\Pi$ state

Since the angular momentum coupling systems for A and X states in NO is different, the rovibronic term values also differ for the X and A states. The $X^2\Pi$ state is intermediate between Hund's case (a) and Hund's case (b). It is because the uncoupling of S increases with increasing J until the total spin is totally decoupled from the inter-nuclear axis. The $^2\Pi$ state is the pure Hund's case (b) at large J. The quantum number J is the total angular momentum including the electronic spin S but excludes the nuclear spin: J $\equiv$ L + N + S = N + S (for Hund's case (b), $\Lambda = 0$). This rule gives J = N $\pm$ 1/2 for a doublet electronic state (S =$\pm$ 1/2). If N = 0, J = 1/2. For a Hund's case (a) electronic state $X^2\Pi$ of NO in the small J limit, we only need Ω, J, and e or f parity to describe rovibronic energy level. The parity of the rotational levels in the e or f parity notation are described in [61]. It is because the symmetry of the rotational wave function alternates with J. Rovibronic levels of both Hund's case (a) and Hund's case (b) electronic states are labeled according to their e or f parity. For a Hund's case (b) state, such as $A^2\Sigma^+$ state and the $^2\Pi$ state (high J limit) of NO, we need both quantum numbers, J and N. It is because for each N $>$ 0, there exist rovibronic states for J = N$\pm$1/2. If N = 0, the only allowed value of J is J = 1/2. The cause of the splitting between the e and f states for the $X^2\Pi$ state and for the $A^2\Sigma^+$ state are practically different. For the $X^2\Pi$ state, the e and f states are two Λ-doubled components. The total parity selection rule is + $\leftrightarrow$ -. The + and - sign

was proposed by [62].

The allowed electric-dipole transitions can be used for the selection rule on J which is given by

$$\Delta J = 0, \pm 1 \tag{2.7}$$

The spin multiplicity 2S + 1 is even in NO and the angular momentum quantum number J is half-integral. So, the parities of the e and f states that result from the Λ doubling interaction are $(-1)^{J-1/2}$ and $(-1)^{J+1/2}$. The three possible branches are the P, Q, and R branches. For electric dipole transitions, the selection rules are described as follows. For Q branches (ΔJ = 0), e $\leftrightarrow$ f, for P branches (ΔJ = -1), e $\leftrightarrow$ e or f $\leftrightarrow$ f, and for R branches (ΔJ = +1), e $\leftrightarrow$ e or f $\leftrightarrow$ f. All the electric dipole allowed transitions are shown in Figure 2.4.

2.3.2 $A^2\Sigma^+$ state

$A^2\Sigma^+$ state is pure Hund's case (b). In this case the new quantum number is N, which corresponds to rotations perpendicular to the inter-nuclear axis. All rotational levels of the A state separate into narrow doublets with the same value of N but different J as noted by [63]. This effect arises in the A state because of the interaction between the relativistic electron spin and the magnetic field created by nuclear rotation. Due to this interaction, the rovibronic energies of the $A^2\Sigma^+$ state of NO is changed. For the $A^2\Sigma^+$ state, the rovibrational energy levels for a given N > 0 is degenerate with respect to J while neglecting the spin-rotation interaction. But, if we include the spin-rotation interaction, the spin-rotation interaction splits each rovibronic energy level with N $>$

0 into energy sublevels with different values of J. Therefore, the resulting sublevels are frequently labeled as e and f levels. Each of $A^2\Sigma^+$ rovibronic sublevels with N > 0 is two-fold degenerate so the spin-orbit interaction results in two rovibrational levels for each N > 0: J = N - 1/2 for f levels and J = N + 1/2 for e levels. The energy of the J = N + 1/2 sublevel is lowered and the energy of the J = N - 1/2 sublevel is raised by the spin-rotation interaction. Thus, the lowest rovibronic sublevel of the $A^2\Sigma^+$ state of NO is an e state with N = 0, J = 1/2.

2.3.3 Molecular transition energy

Table 2.1 summarizes the values of the Hamiltonian matrix elements for NO $X^2\Pi$ [64]. In Table 2.1, T^{Π} is the electronic term values, AX is the spin orbit interaction term, B^{Π} is the rotational constants, D^{Π} is the centrifugal distortion constant, $p\nu$ and $q\nu$ are Λ doubling constants, and γ^{Π} is the spin rotation interaction term. Matrix elements in Table 2.1 can be expanded to calculate the ground state energies given below.

$$
\begin{aligned}
TX \;=\; & T^{\Pi}\begin{pmatrix} 1 & 0 \\ 0 & 1 \end{pmatrix} + AX\begin{pmatrix} 0.5 & 0 \\ 0 & -0.5 \end{pmatrix} + AD\begin{pmatrix} 0.5(z-1) & 0 \\ 0 & -0.5(z+1) \end{pmatrix} + B^{\Pi}\begin{pmatrix} z-1 & -z^{0.5} \\ -z^{0.5} & z+1 \end{pmatrix} \\
& + D^{\Pi}\begin{pmatrix} -(z-1)^2-z & 2zz^{0.5} \\ 2zz^{0.5} & -(z+1)^2-z \end{pmatrix} + p\nu\begin{pmatrix} 0 & -0.25z^{0.5} \\ -0.25z^{0.5} & 0.5(1\pm(J"+0.5)) \end{pmatrix} \\
& + q\nu\begin{pmatrix} 0.5z & 0.5z^{0.5}(-1\pm(J"+0.5)) \\ 0.5z^{0.5}(-1\pm(J"+0.5)) & 0.5(z+2\pm(J"+0.5)) \end{pmatrix} + \gamma^{\Pi}\begin{pmatrix} -0.5 & 0.5z^{0.5} \\ 0.5z^{0.5} & -0.5 \end{pmatrix}
\end{aligned}
$$

(2.8)

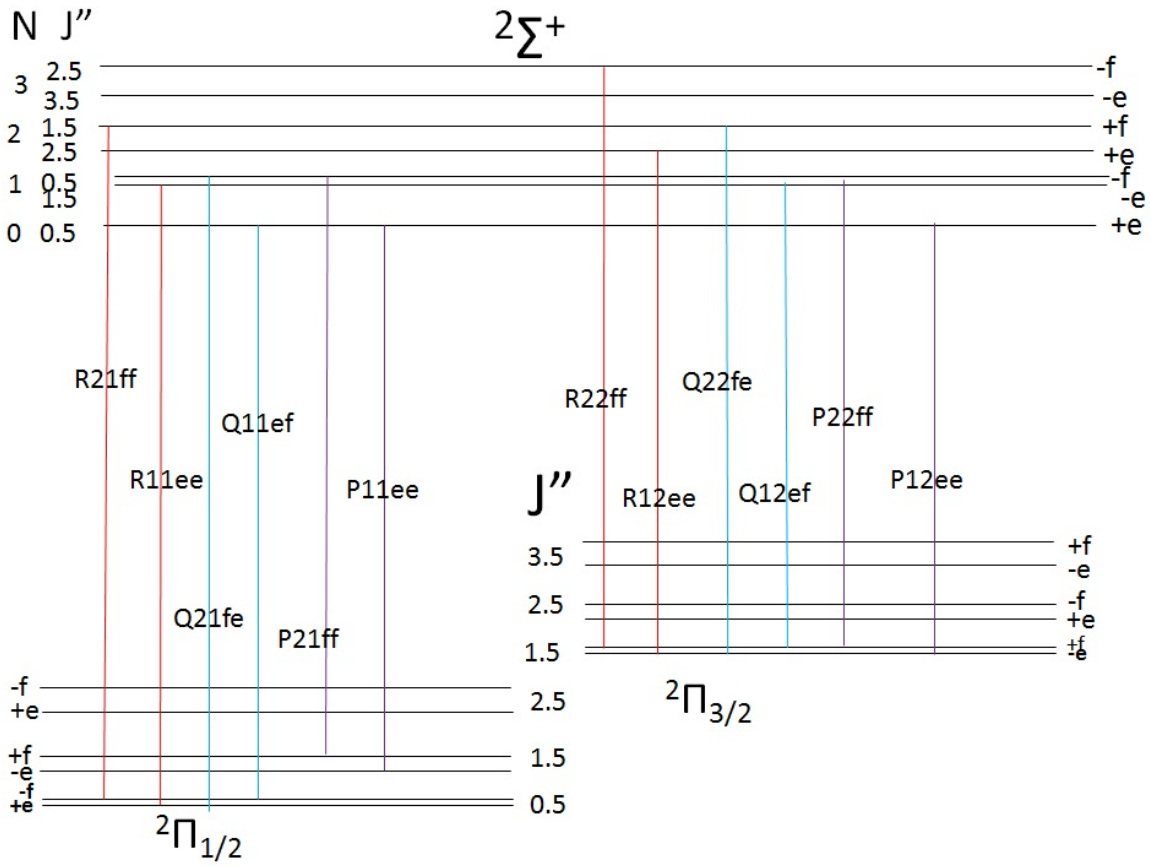

Figure 2.4: NO energy level diagram of the vibrational ground states of the electronic ground state $X^2\Pi$ and the first excited state $A^2\Sigma$. The Λ doublet splitting in the energy levels in the $X^2\Pi$ state and spin - rotation interaction splitting of the energy levels in the $A^2\Sigma$ state are also shown. Electric dipole allowed transitions with first few rotational transitions for all 12 branches are also sown in the figure.

Table 2.1: Hamiltonian matrix elements for NO $X^2\Pi$ including the Λ doubling. z=(J″-0.5)(J″+1.5). The upper signs are for e states and the lower signs are for f parity levels

.

$\Omega = \frac{3}{2}$	$\Omega = \frac{1}{2}$
$\mathrm{T}^{\Pi} + 0.5AX + 0.5AD(z-1) + B^{\Pi}(z-1) + D^{\Pi}(-(z-1)^2 - z) + 0.5q\nu z - 0.5\gamma^{\Pi}$	$-\mathrm{B}^{\Pi}z^{0.5} + 2D^{\Pi}zz^{0.5} - 0.25p\nu z^{0.5} + +0.5q\nu z^{0.5}(-1 \pm (J"+0.5)) + 0.5\gamma^{\Pi}z^{0.5}$
$-\mathrm{B}^{\Pi}z^{0.5} + 2D^{\Pi}zz^{0.5} - 0.25p\nu z^{0.5} + +0.5q\nu z^{0.5}(-1 \pm (J"+0.5)) + 0.5\gamma^{\Pi}z^{0.5}$	$\mathrm{T}^{\Pi} - 0.5AX - 0.5AD(z+1) + B^{\Pi}(z+1) + D^{\Pi}(-(z+1)^2 - z) + 0.5p\nu((1 \mp (J"+0.5)) + 0.5q\nu(z + 2 \mp (J"+0.5)) - 0.5\gamma^{\Pi}$

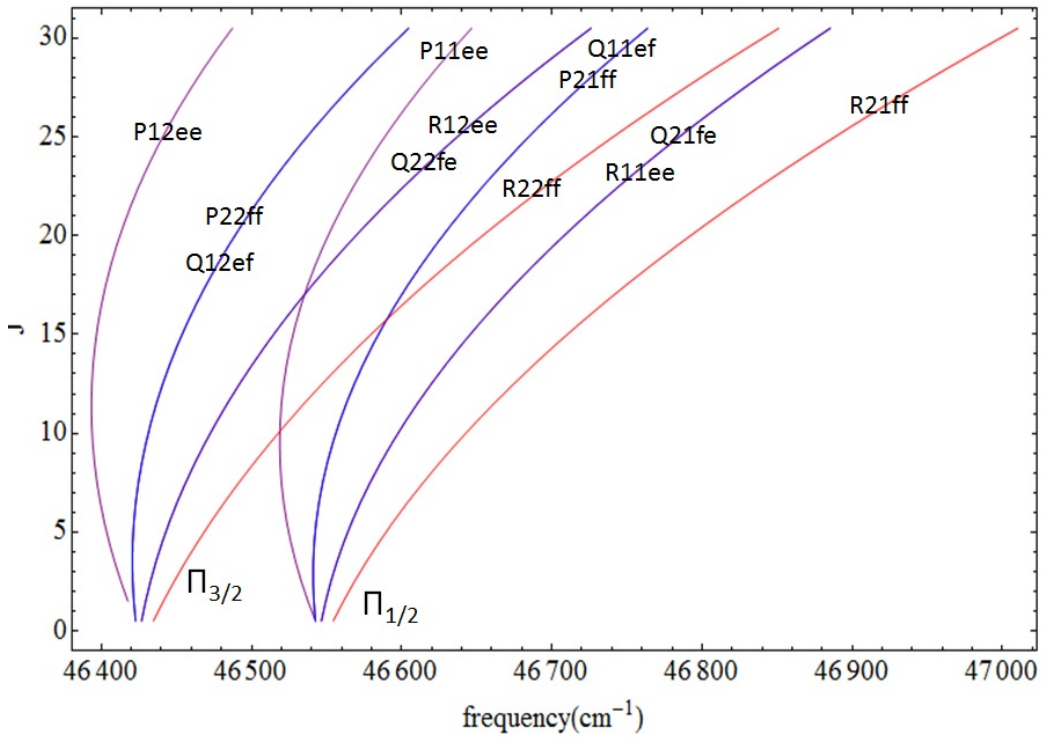

Figure 2.5: Theoretical branches showing $X^2\Pi(\nu'' = 0) \longrightarrow A^2\Sigma(\nu' = 1)$ band of NO.

The expression of the excited state energy $A^2\Sigma^+$ is given by Eq.(2.9) and all the constants are given in Table 2.2.

$$TA = T^{\Sigma} + B^{\Sigma}x(x \mp 1) - D^{\Sigma}x^2(x \mp 1)^2 + 0.5\gamma^{\Sigma}(1 \mp x) \tag{2.9}$$

where x= (J′+0.5) and the - sign refers to e states and the + sign refers to f states. We used rovibronic energy terms to calculate the transition energy in between the electronic states of $A^2\Sigma^+$ and $X^2\Pi$ of NO. For the transition to occur, the total parity of the final state should be opposite to the total parity of the initial state. The rovibrational levels of the first excited state have the total parity of $(-1)^N$.

Table 2.2 lists the constants that we have used to simulate the on resonance NO spectra for NO for $X^2\Pi(\nu'' = 0) \longrightarrow A^2\Sigma(\nu' = 1)$ transitions. The rotational line

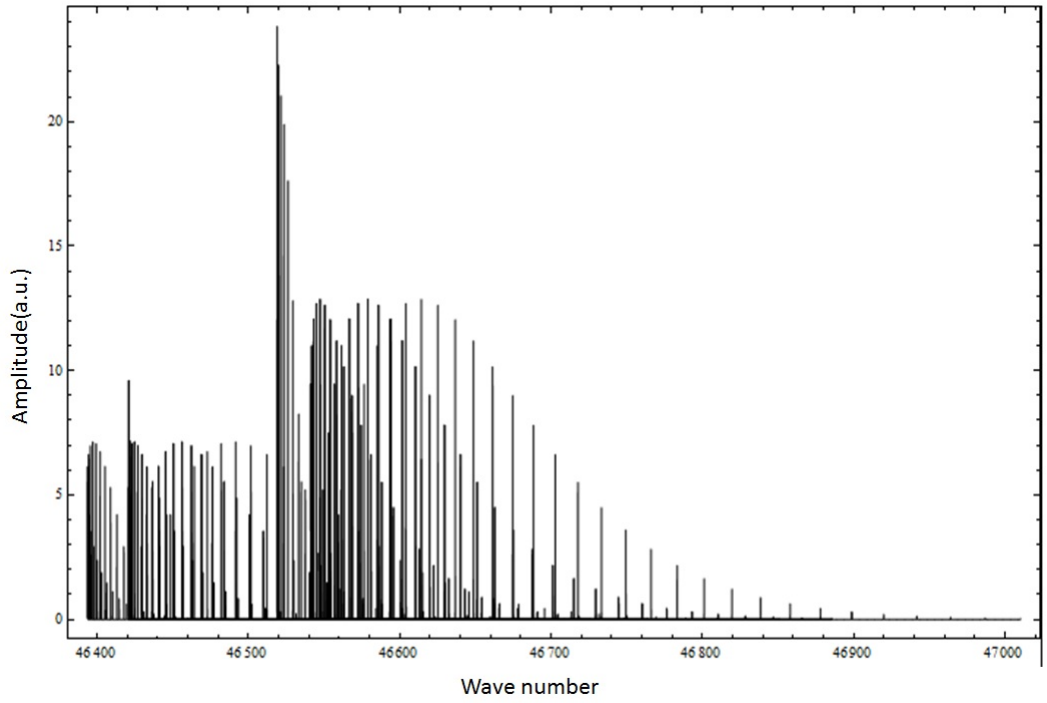

Figure 2.6: Theoretical NO spectra for $X^2\Pi(\nu'' = 0) \longrightarrow A^2\Sigma(\nu' = 1)$ transitions

Table 2.2: Spectroscopic constant for $X^2\Pi(\nu'' = 0) \longrightarrow A^2\Sigma(\nu' = 1)$ transitions of NO. All constants are given in cm^{-1}[1]

T^{Π}	0
B^{Π}	1.6960691
D^{Π}	$5.4722 * 10^{-6}$
AX	123.13582
AD	$1.792 * 10^{-4}$
$p\nu$	$1.1700 * 10^{-2}$
$q\nu$	$1.028 * 10^{-4}$
γ^{Π}	$-2.68 * 10^{-3}$
T^{Σ}	46482.7387
B^{Σ}	1.9674066
D^{Σ}	$5.6731 * 10^{-6}$
γ^{Σ}	$2.672 * 10^{-3}$

distribution at room temperature is the Boltzmann distribution. Theoretically, the rotational structure of the band of the $A^2\Sigma^+ - X^2\Pi$ system gives rise to 12 branches

out of which eight branches can be seen as shown in Figure 2.5. These are six main and six satellite branches designated as $A^2\Sigma^+ - X^2\Pi_{1/2}$: P11ee, P21ff, Q11ef, Q21fe, R11ee and R21ff and $A^2\Sigma^+ - X^2\Pi_{3/2}$: P12ee, P22ff, Q12ef, Q22fe and R12ee, respectively, as shown in Figure 2.4. The branches' name are described in [61]. The pairs of the branches P22ff, Q12ef and R12ee, Q22fe of the $A^2\Sigma^+ - X^2\Pi_{3/2}$ cannot be resolved into two separate branches because of the small spin rotation constant as shown in Figure 2.5. Similarly, the pairs of the branches P21ff, Q11ef and R11ee, Q21fe of the $A^2\Sigma^+ - X^2\Pi_{3/2}$ cannot be resolved into two separate branches because of the similar reason (Figure 2.5). We used the Mathematica programming to simulate this spectra as shown in Figure 2.6 using the known molecular constants of the NO A and X states given in [1]. The simulated theoretical spectra and experimental spectra at a normal temperature are shown in Figure 3.3.

Chapter 3

The feasibility of an activated carbon source for buffer gas cooling experiments

3.1 Introduction

Out of all the approaches mentioned in the chapter 1, the thermalization with a cold buffer gas is the most general process [10, 11] for cooling particles. Almost all buffer gas cooling groups produce the initial molecules or atoms by laser ablation from a solid precursor [10, 11]. These groups direct and tightly focused laser light pulses onto the precursor solid targets glued to the buffer gas cell. After ablation, the molecules or atoms are cooled by the helium buffer gas atoms by thermalization. In this chapter, I will describe a new laserless source of molecules for cold molecule experiments which may eliminate the need for ablation loading in buffer gas cooling experiments. This process will be especially useful for researchers that use dilution refrigerators that have little optical access.

The design of the new source was inspired by the need of the simple and cheap sources of the molecules. We have tested the release of the NO molecules from the activated carbon approximately at 11 K and at pressure of 10^{-6} torr. Under these conditions, the activated carbon absorbs the NO molecules. NO gas was released when a pulse of current was passed through activated carbon. When the NO released from the activated carbon after heating it by a pulse of current is passed to the buffer gas, it may be cooled up to the temperature of the buffer gas by elastic collisions with the

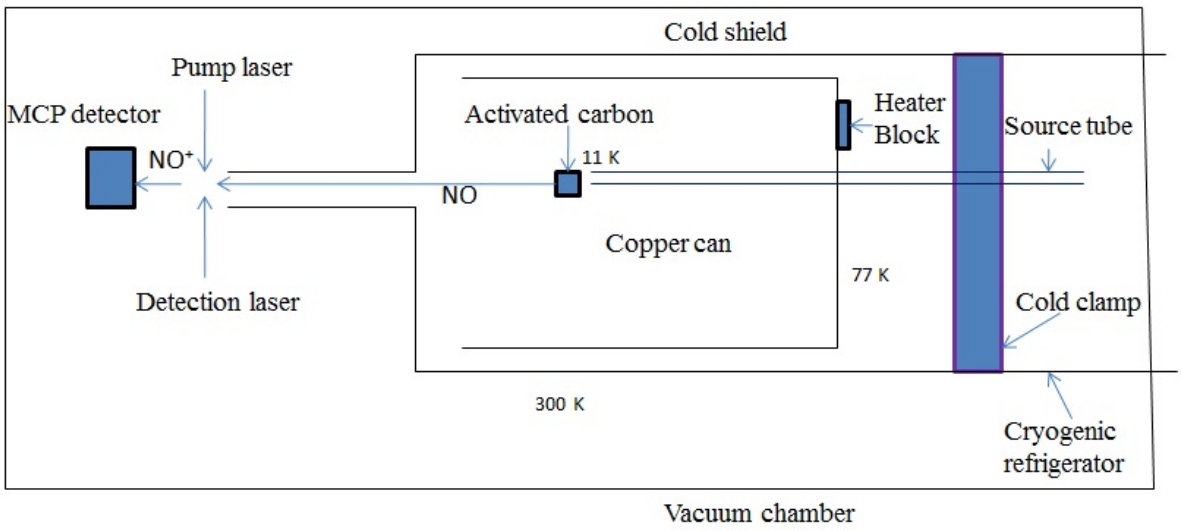

Figure 3.1: Experimental set up. Molecules are directly absorbed by the activated carbon at cold temperature and are released when the pulse of current is sent. The released molecules are detected by the detector.

buffer gas atoms. The cold NO thus produced may be trapped by the magnetic trap.

3.2 Apparatus

This section describes the apparatus that we used for the experiment. The current apparatus consists of two regions: the source chamber and the detection region. The parts of the source chamber and its principle of operation, such as the manifold, the cryogenic refrigerator (cryo pump), the radiation shield, the copper can assembly, the source chamber, a resistive heater, a pair of resistive temperature sensors, and a temperature controller manufactured by Lake Shore cryogenics are described in detail in the references[65, 66]. In this section, I will discuss only the modifications we have done. The experimental set up is shown in Figure 3.1. For the new source, we used a 1/8 inch outer diameter and 1/16 inch inner diameter stainless steel tube that transports the NO from the manifold to the copper can.

A problem with small inner diameter is *freeze out* of the NO when the tube is cooled. *Freeze out* occurs when enough NO gas condenses at cold temperature on the walls of the tube to cause the output to be clogged or blocked, limiting the flow of NO. The source tube and the manifold are connected using Teflon tubing so that heat transfer between the room and the source tube is reduced. The source tube is cooled by clamping it to the cryo pump with a circular double clamp constructed from aluminum. A problem with *freeze out* of the NO was solved by heating the copper tube by using the current as described in [65, 66]. The clamp is located between the two stages of the cryo pump. A resistive heater of 100 ohms is attached with the copper can using indium foil to control the temperature of the copper can. The copper can is wrapped with a pair of copper wires; one end of which is connected to the 3458A multimeter to measure the four wire measurement of the activated carbon resistance that I will discuss below. In our experiment, the carbon sat inside the copper can just in front of the stainless steel tube. One end of the copper can was removed. The other end of the can is attached to the cryo pump and has a 0.25 inch bore that allowed for the insertion of the NO source tube. During normal operation, the can reached a temperature of 11 K as measured on the face of the copper can. The can's main purpose was to enclose the activated carbon, to hold the source tube, and to maintain the equilibrium temperature of the carbon. It also controlled the flow of NO directly into the entire chamber. Machine drawing of the vacuum equipment is shown in Appendix H.

The detection region consists of the stainless-steel vacuum chamber equipped with

fused silica windows, which are constructed from an 8 inch cube and an 8 inch tee and the detector. The ultimate pressure is achieved in this chamber using a mechanical pump, a turbo pump, and a cryo pump is around 5×10^{-8} torr. This chamber holds the Micro Chanel Plate (MCP) detector to collect the experimental data. The first section of the detector consists of two 3 inch diameter stainless steel plates, each with a 0.5 inch bore at its center. These plates are approximately 1/16 inch in thickness. 1/2 inch ceramic spacers separate these two plates to electrically isolate them from one another. These plates are used to create pulsed fields of around 300 V that create and push ions. A third plate with similar dimensions is grounded and creates a field-free region where ions can drift. This field-free region is enclosed in a Faraday cage made from a cylinder of fine mesh screen. This cage prevents stray fields and stray particles from entering this region. The field free region ends at the collector. The collector contains a set of MCP that operates at -2000 V. The electric pulse that is produced in the MCP following the incidence of the ions overlaps and makes an ion current. As positive ions hit the plate, a signal is created, which is collected at the anode of the detector. The signal collected is plotted as a function of time. The MCP detector we have used is described in detail in [65].

3.3 Lasers

Figure 3.2 shows the schematic of the laser setup employed for two-color resonance-enhanced multiphoton ionization(REMPI) of NO. This consists of an Nd:YAG laser, a pulsed scanmate dye laser (Lambda Physik), two crystals, an optical path, and a

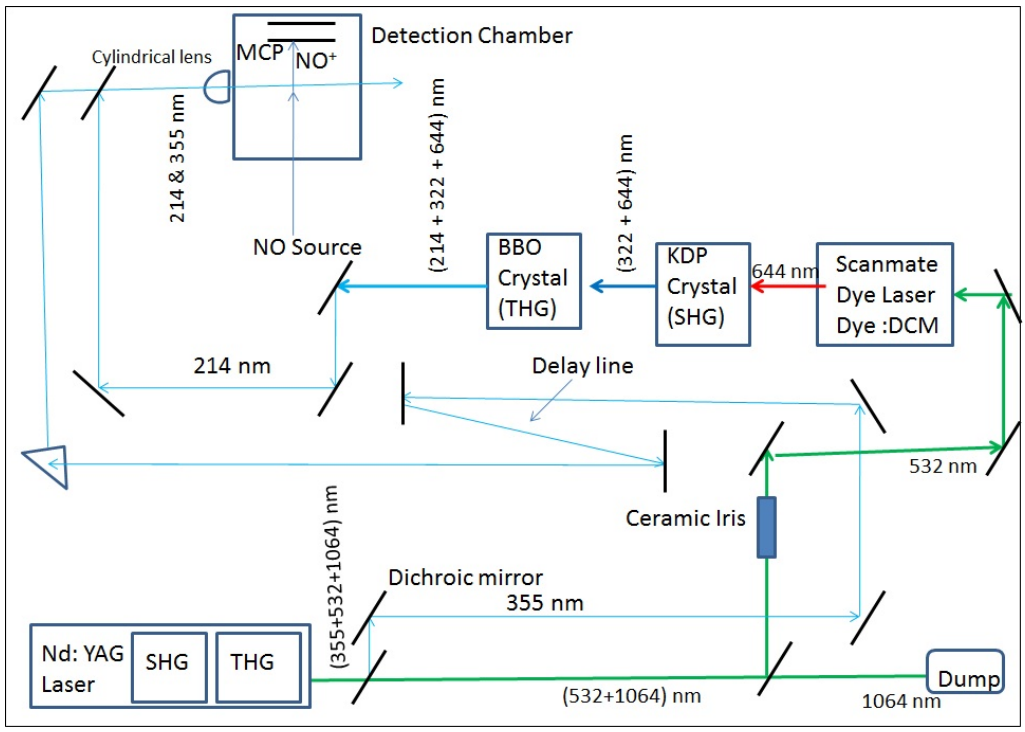

Figure 3.2: Schematic diagram of the experimental set-up.

variety of optics to shape and direct the beam. Nd:YAG laser which pulses with a repetition rate of 10 Hz, was used for nonlinear generation of 10 ns pulses Ultraviolet (UV) light. The Yag laser outputs were a mixture of 1064 nm, 532 nm and 355 nm because of second and third harmonic generation crystal. The 355-nm light was achieved through frequency tripling a laser beam with 1064 nm. A dichroic beam splitter divided the output of the Nd:YAG laser and created two beams of similar intensity. One beam was 532 nm and was directed to the scanmate dye laser, and the other 355 nm light was directed to the detection chamber. The laser dye used in scanmate dye laser was DCM. This particular dye is used because the center of the gain curve is near the wavelengths that we need (644 nm). The output of the scanmate dye laser was tuned to 644 nm, which had a peak power of around 19 mJ.

However, light with a wavelength of around 214 nm was needed for the experiments performed. A narrow bandwidth tunable to 214 nm laser light was obtained from a 644 nm due to frequency tripling the output of the scanmate dye laser through a Beta Barium Borate (BBO) second harmonic and Potassium Dihydrogen Phosphate (KDP) third harmonic generation crystal. The laser frequency from dye is doubled in a KDP crystal and the doubled and fundamental frequencies are mixed in a BBO crystal to produce the third harmonic light(214 nm).

Two step processes are used to produce 214 nm light from 644 nm light. The first step is to generate the 322 nm light using the KDP crystal. The second step is to generate the 214 nm by sum-frequency generation of the 644 nm light and 322 nm light by using third harmonic BBO crystal. To get the 214 nm light, the polarization of the 644 nm and 322 nm light should be in the same direction before they pass to the third harmonic crystal. But after passing through KDP crystal, they are polarized perpendicular to each other. This problem can be corrected by inserting a half wave plate between the two crystals. The plate is half wave plate for the 644 nm. Also, this plate can be used to rotate the polarization of the 644 nm to any anticipated angle. If the plate is a half wave plate for the 644 nm light, it will be a full wave plate for the 322 nm light, so that the 322 nm light is not affected. It is because the full wave plates do not disturb the polarization. The efficiency of this process was dependent on the intensity of the original laser beam and the angle on the incident face of the crystal makes with the beam. The scanmate dye laser is equipped with computer controlled auto tracking. The autotracker 11 was used to find the proper angle of the

incidence face of the crystal. The Autotracker II is designed for frequency mixing of pulsed lasers in nonlinear crystals such as KDP and BBO crystals. The autotracker 11 works by sensing the frequency mixed output of an angle tuned crystal. Once the lasing had been achieved in the scanmate dye laser, the output was directed into the chamber as shown in Figure 3.2. Since the three beams were collinear, a system of dichroic mirrors was used to filter away most of the 644 nm and 322 nm light. After each beam (215 and 355 nm) passed through separate dichroic mirror paths, the beams were sent through a cylindrical lens of 8 cm focal length that vertically stretched the beam at the center of the detection chamber. The 355 nm pulses were optically delayed by extending their beam path about 3 m longer than the 215 nm path as shown in Figure 3.2. Finally, the overlapped, cylindrically focused beams are centered between the two pulsed field plates with the focus at the center of the output of NO source. Furthermore, we used the lenses that control the size of the beam at the center of the detection chamber. The 355 nm beam has dimensions of 200 nm and 5 mm, respectively. These beams passed in and out of the detection chamber through sapphire view ports that transmit 75 percent of UV light.

We measured the pulse energy to be about 5 mJ and an approximate beam cross-section of 5 mm by 3 mm for 214 nm beam. The laser 214 nm light has a linewidth of $0.02cm^{-1}$. Nitric oxide has a low ionization potential of 9.26 eV($74686.25cm^{-1}$)[67]. The first electronic A state has a lifetime of about 200 ns [68], which leads to a high probability of ionization by absorbing further photons. High-resolution spectroscopic detection of NO can be done using simple one-and two-photon laser-induced fluores-

cence (LIF) as well REMPI techniques[69]. A two-color (1 + 1') REMPI scheme can be used (Figure 3.3) to achieve high spectral resolution of NO spectra. When the energy of one or more photons is in resonance with the real intermediate states of the species, the second photon is used to excite the species into the ionization state. This process is useful and more usable than other techniques for the state-resolved probing of NO. Since most of the molecules lie in $X^2\Pi(\nu'' = 0)$ state at room temperature. The ionization signals that correspond to $X^2\Pi(\nu'' = 0) \longrightarrow \mathrm{A}^2\Sigma(\nu' = 0, 1)$ are stronger than $X^2\Pi(\nu'' = 1) \longrightarrow \mathrm{A}^2\Sigma(\nu' = 0, 1)$. Because of this reason, we carried out the REMPI two color process with one fixed wavelength (355 nm) and scanned the second laser by wavelength in the desired region in order to pump the $X^2\Pi(\nu'' = 0) \longrightarrow \mathrm{NO}(\mathrm{A}^2\Sigma^+)$ transition. Experimentally, as shown in Figure 3.3, we have 8 branches out of which only 7 branches are within the range of our scan. We have assigned all the rotational lines using theoretical spectra as shown in Table 3.1.

In our experiment, NO (11 percent) seeded into helium (89 percent) passed through the 1/16 inch stainless steel tube into a high vacuum chamber at a pressure of around 10^{-7} torr. To create cold molecular beams, NO can be added to the seed gas in low concentrations. The target molecules in the ground state first absorbed the UV light at 215 nm, which leads to the population of $A^2\Sigma^+$ state given as: $NO(X^2\Pi) \overset{h\upsilon_1(\lambda=215nm)}{\rightarrow} NO(A^2\Sigma^+)$. When a second photon of 355 nm was absorbed by the excited molecule, leading to ionization given as follows: $NO(A^2\Sigma^+) \overset{h\upsilon_1(\lambda=355nm)}{\rightarrow} NO^+ + e^-$. The laser wavelength was scanned with 0.002 nm steps over $A^2\Sigma^+_{1/2}(\nu = 1) \leftarrow X^2\Pi_{1/2}(\nu = 0)$ band of the A - X transition during the data collection. An ionization signal is only

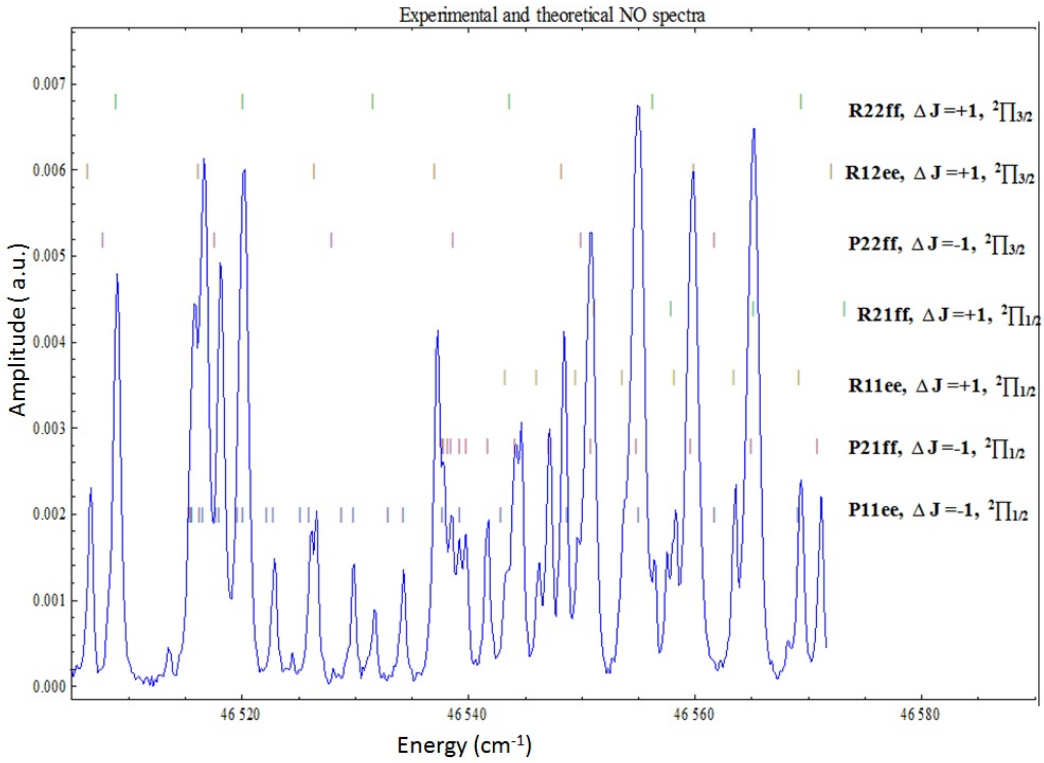

Figure 3.3: 1+1' REMPI spectra of transition in the ($X^2\Pi(\nu'' = 0) \longrightarrow A^2\Sigma(\nu' = 1)$)band of the NO as a function of pump laser frequency at room temperature. The dashed lines are the theoretical spectra as simulated in chapter 2.

Table 3.1: Observed rotational transitions energies within $A^2\Sigma^+_{1/2}(\nu = 1) \leftarrow X^2\Pi_{1/2}(\nu = 0)$ band of NO.

J″	**Observed energy** (cm^{-1})	**Branch**	**Residual (Cal-Obs)**
12.5	46508.0469	R12ee	-0.00981
9.5	46510.7461	R22ff	0.0139
8.50	46517.253	P11ee	-0.013
7.50	46518.119	P11ee	0.025
6.50	46519.563	P11ee	-0.017
5.50	46521.717	P11ee	-0.01
4.50	46524.199	P11ee	0.002
3.50	46527.5	P11ee	-0.002
2.50	46531.378	P11ee	-0.015
11.50	46533.278	R22ff	-0.02
1.50	46535.768	P11ee	0.002
0.50	46539.34	P11ee	0.016
5.50	46541.345	P21ff	-0.011
6.50	46543.245	P21ff	-0.01
7.50	46545.545	P21ff	-0.015
1.50	46547.6345	R11ee	0.0105
8.50	46548.449	P21ff	0.02004
2.50	46551.058	R11ee	-0.01
9.50	46552.243	P21ff	-0.011
3.50	4655.1781	R11ee	-0.0091
10.50	46556.3899	P21ff	0.0071
4.50	46559.716	R11ee	0.044
11.50	46561.1588	P21ff	0.0092
5.50	46564.978	R11ee	-0.017
12.50	46966.665	P21ff	-0.001
6.50	46570.7675	R11ee	-0.0025
13.50	46572.56756	P21ff	-0.01056

present if the energy of the first photon is resonant with an electronic transition from one of the $X^2\Pi_{1/2,3/2}$ states to the $A^2\Sigma^+$ state. And this ionization signal is proportional to the population in the ground state $X^2\Pi$. Thus, the distribution of population over the rotational and vibrational levels in the $X^2\Pi$ electronic ground state is probed. So, the REMPI scheme resolves the vibrational, rotational, and

spin-orbit structure of the $X^2\Pi_{1/2,3/2}$ state.

3.3.1 Activated carbon experiment and results

The rectangular piece of activated carbon of around 3.5 mm by 2.5 mm having 0.931 ohm resistance at normal temperature and the pressure was kept just in front of the source tube and inside the copper can as shown in Figure 3.1. The MCP was placed 30 inches away from the NO source. The pressure was reduced to 10^{-7} torr. The activated carbon was dried thus removing all gases from it by heating it to 95 degrees centigrade for about 10 minutes using a resistive heater that was attached to the copper can. Then, the cryo pump was turned on; it took around 7 hours to cool the copper can from a room temperature to around 11 K using the second stage of the cryo pump. Since the carbon is inside the copper can, it was also cooled by conduction from room temperature to around 11 K. The temperature of the copper can was monitored using the Silicon Diode sensors that were connected to the LakeShore 331 Temperature Controller. The temperature was noted using Labview code written for temperature controller.

Because of the high electrical conductivity and a relatively low temperature dependence of resistance from room temperature to helium temperatures of Phosphor Bronze wire (copper-tin-phosphor alloys), we used 38 Awg Phosphor Bronze wire for a four wire measurement of resistance of the Pt100 sensor, activated carbon and RuO_2 sensor. This wire is a good choice as it minimizes the pickup noise from induced currents through the leads. 3458A HP multimeter was used for the four wire measurement of resistance. In two wire measurement, an ohmmeter measures

all resistance in the circuit loop, which includes the resistance of the wires as well as the resistance of the component being measured. If the component to be measured has a low resistance, the measurement error introduced by wire resistance will be considerable. Our carbon has resistance of 0.9 ohms and the connecting wires have a resistance of about 2 ohms. So, two wire measurements were not practical. To correct it, we used four wire measurement of the resistance. In this process, 3458 A HP multimeter sends the current to the carbon and the voltage drop across the carbon is measured. From Ohm's law, the resistance is given by volt/current. This measurement avoids errors caused by wire resistance. 32 Awg copper wires were used to send the pulse of current to the carbon.

To measure the resistance of the carbon as a function of temperature after sending the pulse of current, we attached the Pt100 thermometer to the carbon using Teflon tape. But the Pt100 thermometer does not go linearly beyond 20 K, and our cryo pump could cool the copper can and carbon to 11 K. Also, when one pulse of current was sent to the activated carbon, the carbon was heated immediately but the Pt100 thermometer did not respond quickly to the temperature of the carbon. Because of these reasons, we could not measure the exact change in temperature, resistance, or the total exact amount of energy delivered to the carbon. Then, we used the RuO_2 sensor to measure the temperature of the carbon. First, we calibrated the RuO_2 sensor. The RuO_2 sensor and Silicon Diode sensor were insulated together using Teflon tape and was attached to the copper can using the screw. Then, the cryo pump was turned on. The temperature of the copper can gradually went down from room temperature

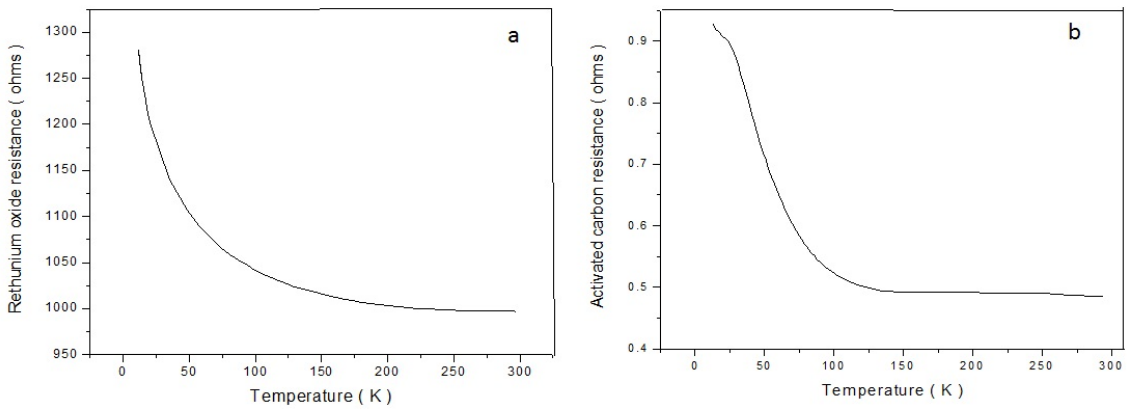

Figure 3.4: (a) Change in resistance of ruthenium oxide sensor as a function of silicon diode temperature.(b) Calibration of carbon.

to 11 K. The temperature of the RuO_2 sensor and the Silicon Diode sensor also went down gradually by conduction. The Labview program code was written to run simultaneously the 3458 A HP multimeter to measurement the resistance of the RuO_2 sensor, and temperature controller to measurement the temperature of the Silicon Diode sensor. Finally, the RuO_2 sensor was calibrated as a function of temperature. The calibration curve is shown in Figure 3.4(a). The RuO_2 sensor is accurate to below 20 K, and also we measured the resistance of the dried activated carbon at different temperatures using the calibration curve. But we saw that the RuO_2 sensor also did not respond immediately to the change in temperature of the carbon. So, this process of using this sensor was also not practical to measure the temperature of the carbon. Thus, we calibrated the dried activated carbon itself as a function of temperature. This is shown in Figure 3.4(b).

Again a Labview program was written for the 3458A multimeter, the 3457A power supply and the TDS oscilloscope so that they could run at the same time. At around

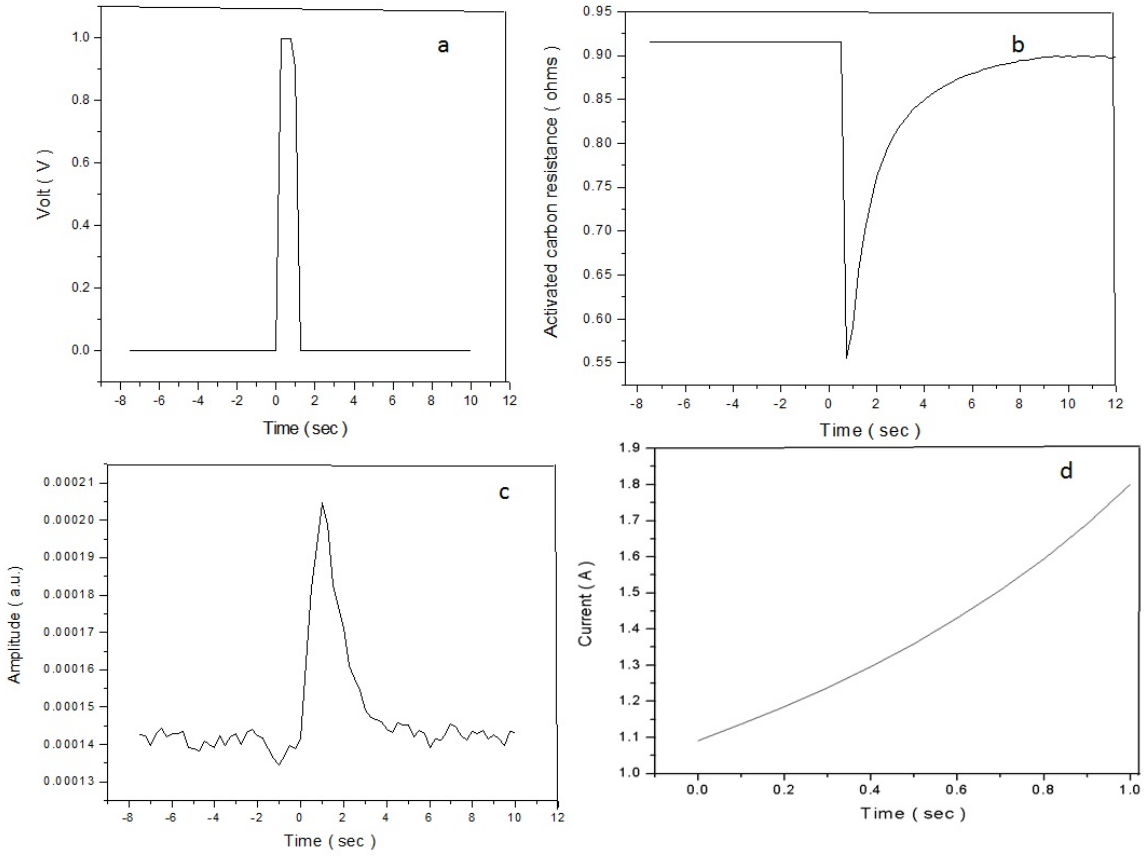

Figure 3.5: (a) The time of the pulse. (b) Change in resistance of the carbon for a pulse of current. (c) NO spectra detected by MCP just after the pulse of the current. (d) Change in current of carbon when a pulse of current is passed through carbon.

10^{-7} torr and 11 K, the activated carbon was charged with NO and the change in resistance of the dried activated carbon was 0.0543 Ohm. A pulse of current was sent through the carbon as shown in Figure 3.5(a), the carbon was heated and its resistance went down as shown in Figure 3.5(b). At the same time, the NO gas was released and the NO was ionized and the ions are detected by the MCP plate as shown in Figure 3.5(c). In this figure, background NO signal is seen before sending the pulse of current to the carbon. The probe laser was set to $46551.06cm^{-1}$ and corresponds to R11ee transition. The total energy delivered to the carbon in one second is given as: $E = \int_0^1 I^2 R\, dt = \int_0^1 V I\, dt$, where V is the potential difference and I is the current. The change of current as a function of time is given in Figure 3.5(d). The temperature change of the carbon during this time was calculated from the calibration curve, which is 71.17 K. Also, the total resistance change and total energy delivered during this time was calculated to be 0.373 ohm and 1.388 J respectively.

Pulse of current brings additional heat into the cryogenic cell. To solve this problem, we can decrease the size of the activated carbon. Some dilution refrigerator with high cooling power can handle this problem. Beam injection method could be the best method for loading of NO gas into the cell. In this method, there is an orifice in the side of the buffer-gas cell, millimeter to centimeter in size, where the carbon can be heated to release NO gas. This process was successfully implemented by Doyle group who have been able to show efficient beam injection loading and buffer-gas cooling of Rb, N, NH, and ND_3[70]. The probe laser was fixed at different frequencies. Shown in the Table 3.2, for each frequency, a pulse of current was sent, the NO is

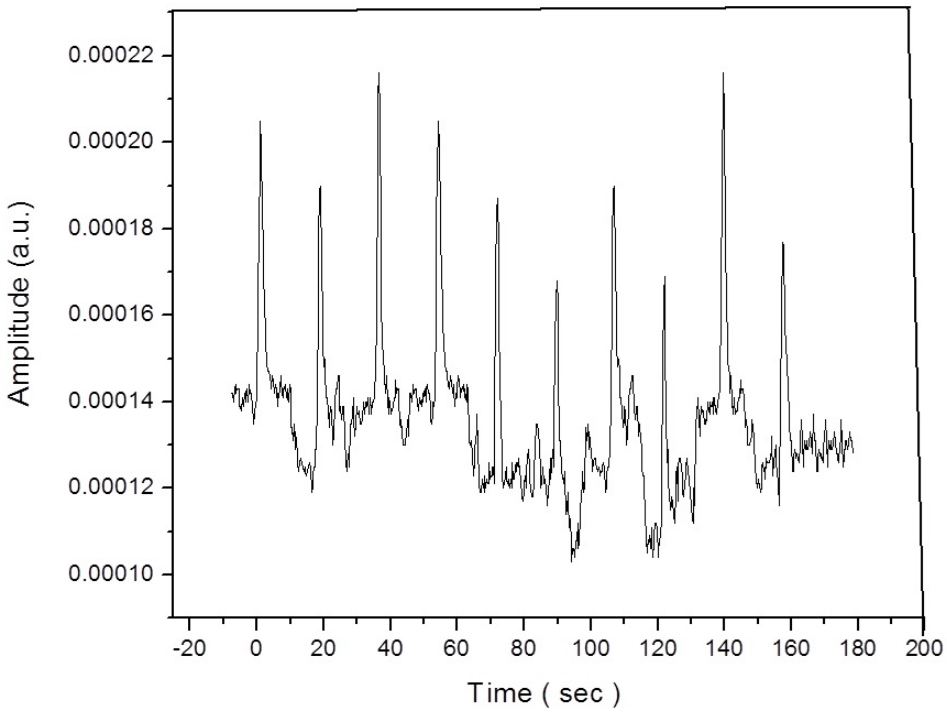

Figure 3.6: The NO is released from the activated carbon for each pulse of current and is detected by the MCP is shown. Each peak corresponds to different rotational levels of NO.

released and was detected as shown in Figure 3.6. Each peak of the line corresponds to different rotational transitions (Table 3.2). The resistance also changes for each pulses of current which is shown in Figure 3.7.

The population of the rotational levels in molecular species is given by the rotational temperature [63]. Each rotational level has a different statistical weight due to the 2J+1 fold degeneracy of each rotational state, where J is the total angular momentum of the molecule. Because of this, the thermal distribution of the rotational states will be given by the product of the Boltzmann factor exp $(-E_J/k_BT)$ and the statistical weight 2J +1. When the molecules in the initial state with rotational quantum number

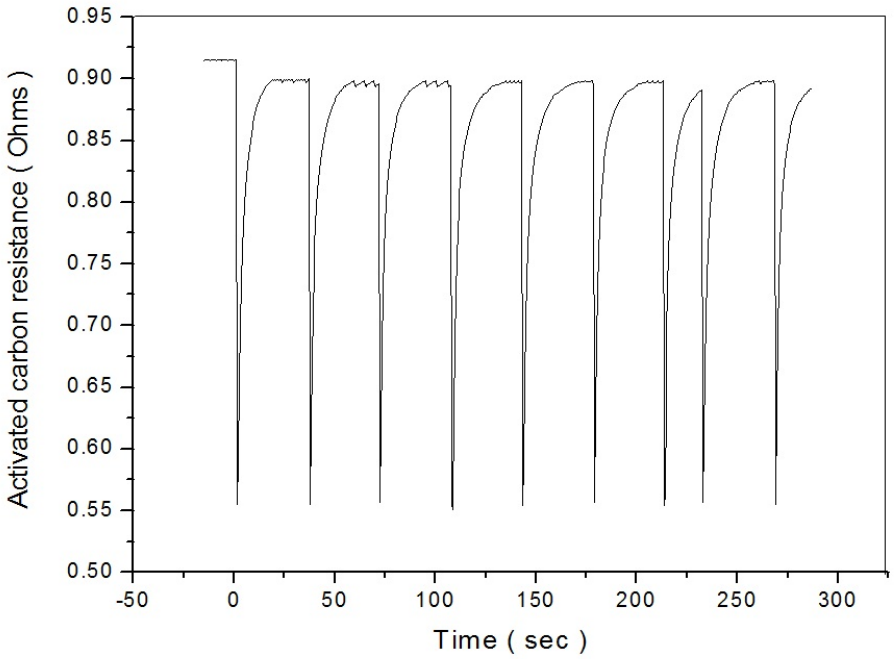

Figure 3.7: The resistance changes for each pulses of current is shown.

Table 3.2: Relative signal amplitude of rotational lines.

Probe laser (wave number)	Branch	J	Relative amplitude (a.u.)
46566.65	Q11ef,P21ff	12.5	0.000064
46564.92	Q21fe,R11ee	5.50	0.0001
46561.09	Q11ef,P21ff	11.50	0.000063
46556.53	Q11ef,P21ff	10.5	0.000071
46552.34	Q11ef,P21ff	9.50	0.000088
46545.55	Q11ef,P21ff	7.50	0.0001
46539.48	P11ee	0.5	0.000048
46535.72	P11ee	1.50	0.000067

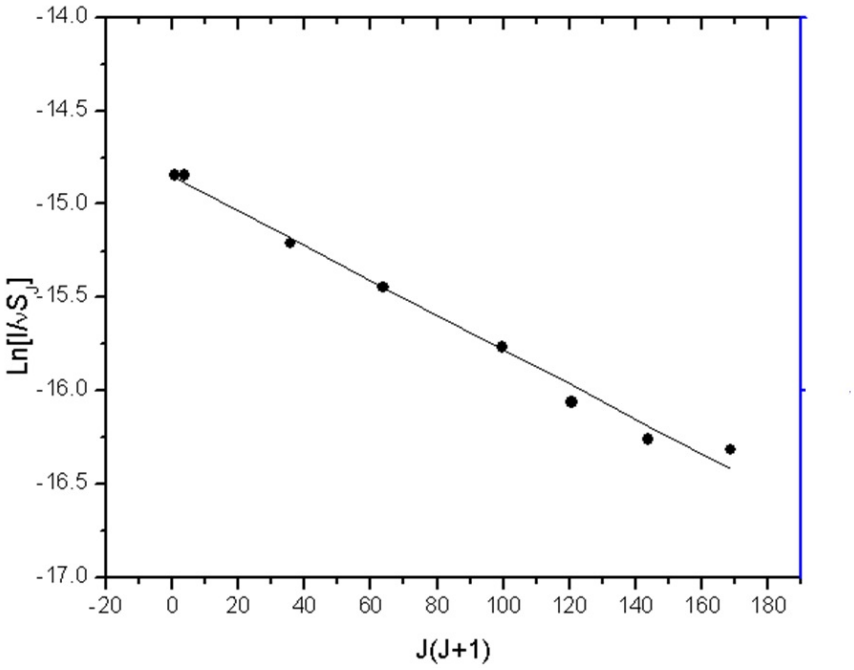

Figure 3.8: A plot of $\ln(\frac{I}{\nu S_J})$ vs J(J+1) to calculate the rotational temperature. The straight line is drawn by the method of the least square.

J absorb the photon with wave number ν, the relationship between the intensity of lines (I) of the vibrational band and the J(J+1) can be calculated from

$$\ln\left(\frac{I}{\nu S_J}\right) = \frac{Bhc}{k_B T} \times J(J+1) + \ln\left(\frac{2C}{Qr}\right) \tag{3.1}$$

Where B is the rotational constant, c is the velocity of light, C is the constant depending on the change of dipole moment, S_J is the line strength which was calculated using the relations given in [63], Qr is the sum of the rotational states and is equal to k_BT/Bhc. This relation is for large T or small B. C and Qr are not needed to calculate the slop of the line. The rotational temperature was calculated to be 264 ± 5 by the slope of the line (Figure 3.8) taking the data from Table 3.2 and using the Eq. 3.1. The straight line in the Figure 3.8 was determined by the least squares method. Errors

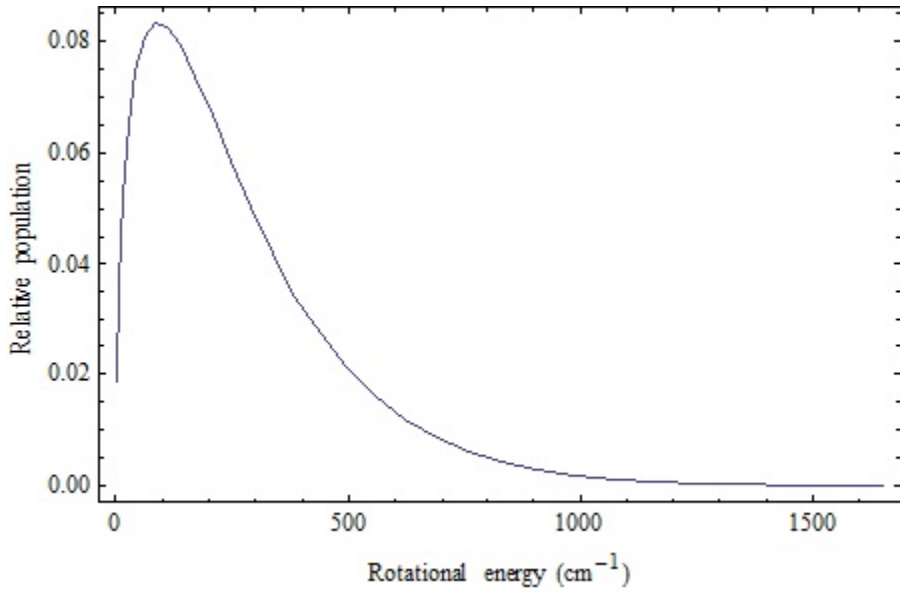

Figure 3.9: Relative rotational population versus rotational energy graphed at 264 K.

of the observed rotational temperature were calculated from the standard deviation of the least squares fit. At large T and small B, the fractional molecular population at the temperature T is given by

$$\frac{N_J}{N} = \frac{Bhc}{k_B T}(2J+1)[e^{-\frac{hcBJ(J+1)}{k_B T}}] \tag{3.2}$$

Where N is the number density at the pressure and temperature of the experiment. The relative rotational population versus rotational energy for this state is shown in Figure 3.9.

Chapter 4

Velocity filtering and guiding of cold molecular NO

4.1 Introduction and motivation

Velocity filtering is a simple idea that we extract only slow molecules from the entire velocity distribution. We need thermal sources of molecules to filter the slow molecules. Molecules are neutral in general, but in some molecules they can have an asymmetric charge distribution with one end more positively charged and other end more negatively charged. These molecules are called polar molecules. NO is a polar molecule so it has a permanent electric dipole moment. The Stark effect is the shifting and splitting of spectral lines of atoms/molecules due to the interaction of the dipole moment with an external static inhomogeneous electric field. The hexapole straight guide consisted of six high voltage cylindrical copper rods in a symmetric arrangement with alternating polarity. The cross section is shown in Figure 4.1(left). The magnitude of the electric field inside the hexapole grows with distance from the axis in the two transverse directions, as shown in the contour plot in Figure 4.1(right). By applying a high enough voltage with a suitable geometry of the hexapole, a two dimensional trap can be formed for low field seeking molecular states, as shown in Figure 4.2.

A very large number of cold molecules exist even at room temperature. By providing the electric field in the hexapole guide that increases in all transverse directions, the molecules in the low field seeking states and with a small enough transverse velocity can be guided. If the guided molecules are sufficiently slow, they can be contained in

traps. As I will describe in the next chapter, our permanent magnet trap has the trap depth of around 0.25 K. For a polar molecule like NO with a mass of $4.98 * 10^{-26} kg$ (30 atomic units), this trap depth corresponds to a velocity of 14.5 m/s. At 300 K and for a cutoff velocity of 14.5 m/s, the fraction of the molecules can be calculated from the Boltzmann distribution, which is $\int_0^{14.5} \frac{4}{\alpha^3\sqrt{\pi}} v^2 e[-\frac{v^2}{\alpha^2}]\, dv \approx 3.3{*}10^{-5}$. The most probable velocity at 300 K is $\alpha = \sqrt{\frac{2k_BT}{m}} = 407.78 m/s$. This result corresponds to the large number of guided molecules when starting with a high density of gas at normal temperature and pressure.

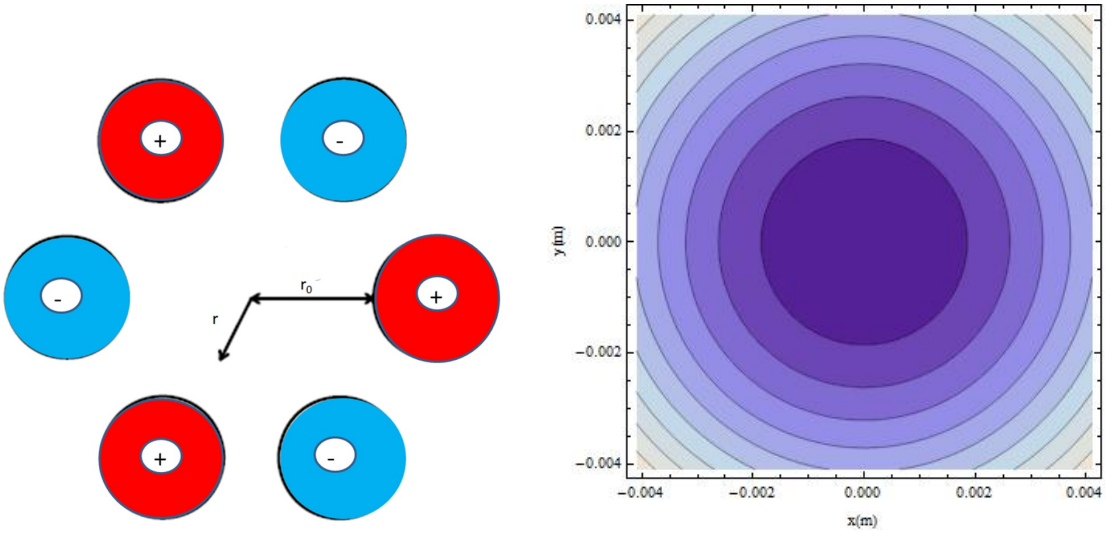

Figure 4.1: Hexapole guide cross section (left). The circles indicate the position of the electrodes at which the alternate voltage is applied. + corresponds to the positive voltage and - indicates the negative voltage. Electric field distribution in the hexapole guide for $\pm 5kV$ electrode voltage (right).

A straight hexapole field guide can guide low-field seeking molecules with low transverse velocities along the path of the hexapole axis. However, the total energy may not be low if the component of the velocity along the guide is large. In fact,

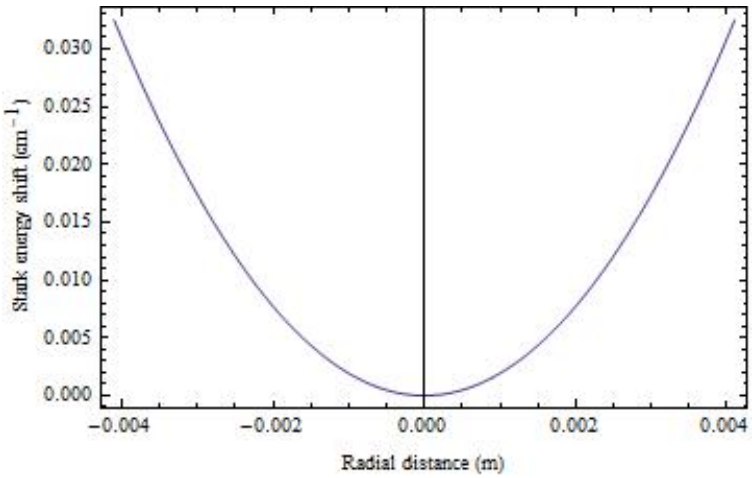

Figure 4.2: A cross section of the two dimensional traps formed inside the hexapole guide through which the low field seeking molecules are guided.

high-field seeking states may make it to the output of the guide if they travel the line of sight between the input and the output. In the rest of this section, I discuss the effusive source, the computer simulation of trajectory of the particles in the hexapole guide, the flux of guided molecules, the loading rate of the magnetic trap of the particular internal state ($\Omega = 1/2$, J = 1/2, $M_J = 1/2$), and the experimental production of cold low field seeking molecular NO.

4.1.1 Effusive source

Filtering slow molecules from the reservoir at a low temperature effusive source is the motivation behind velocity filtering and guiding for further manipulation of the cold gas. The effusive molecular beam source is the container with a hole through which high pressure gas passes into a low pressure chamber where collisions with the fast molecules are less likely to occur. The pressure in the chamber in which the gas flows should be low enough so that the mean free path of the gas should be larger

than the size of the chamber. It can be calculated that the angular distribution of the molecules coming out from the effusive source follow the Cosine law. NO molecules are introduced into the hexapole guide using the stainless steel effusive source. The pressure inside the chamber is kept low so that the molecular beam would be effusive. The total number of molecules per second from an effusive source is given by(4.1)[71].

$$N = \pi a^2 \sqrt{\frac{8RT}{\pi M}} \frac{\Delta P}{4k_B T} \tag{4.1}$$

Where R is the gas constant, M is a molecular weight in kg/mol, ΔP is the pressure difference between high pressure and low pressure side and a is the radius of the cylindrical tube.

With our experimental parameters, the above equation yields a molecular flux of about $10^{16}/sec$. The population of the rotational states at the effusive source is given by

$$P = (2J + 1)exp[-\frac{E_{rot}}{k_B T}] \tag{4.2}$$

where E_{rot} is the rotational energy and 2J+ 1 is the degeneracy taken in the absence of the external field. The rotational population of the molecules with a rotational quantum number less than 41/2 occupies more than 99% of the population at 77 K as shown in Figure 4.3.

4.2 Calculation of the particle trajectory

The trajectory of the particles is evaluated by integrating Newton's classical equations of motion at specified time intervals for the duration of the total simulation time. First, the particles' initial positions and initial velocities at time t=0 are chosen

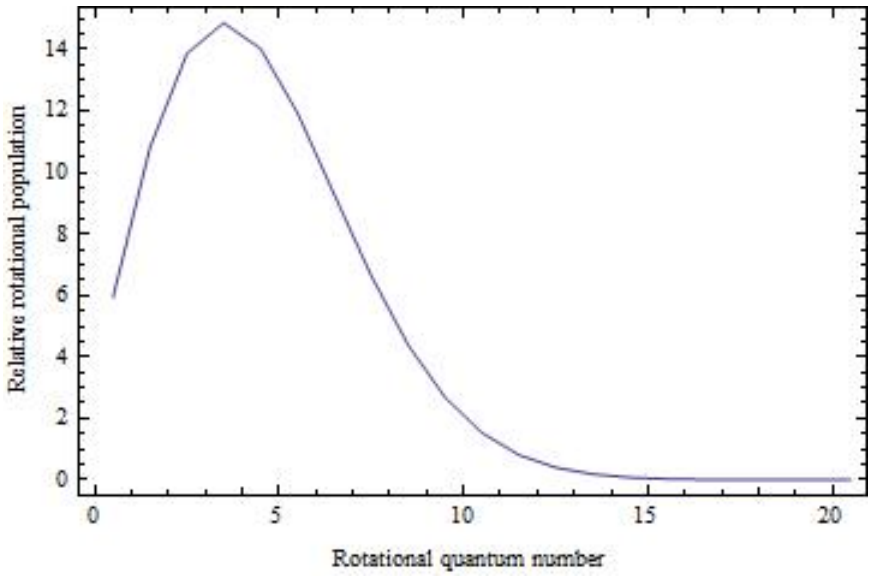

Figure 4.3: Thermal distribution of the rotational levels at T = 77 K. The curve represents the rotational population as a function of J.

randomly. Then numerical integration is done to determine the particle's positions and velocities at time $t(=0)+\Delta t$ from the initial known acceleration so that particles' current velocities are adjusted by the acceleration term to find the new velocities such as $v(t+\Delta t)$ and this new position is adjusted such as $r(t+\Delta t)$ from the standard kinematic trajectory equations. The Mathematica program can be written so that this process is repeated until the whole trajectory for time period t is calculated. When Δt is too large, the calculated path of the particles can be extremely rough so that it will not show the minute oscillations or components of the particles' motion that may occur between very small periods of time. Since the total energy of the system should be a constant in time, we adjusted the energy at each step. We also calculate the new value of potential energy and kinetic energy at a new position r and at a new velocity v and make sure that kinetic energy at this position is positive. If the kinetic energy

at the new position is not positive, the total energy is not physical. Energy adjusting integration algorithm is given in Appendix F.

4.3 A stark hexapole velocity filter

The electric field is axially symmetric in the ideal hexapole given by

$$E(r) = 3\frac{V_0}{2}\frac{r^2}{r_0^3} \tag{4.3}$$

Where, r is cylindrical coordinates, the z-axis coincides with the axis of the hexapole, V_0 is the half of the voltage between two hexapole rods, and r_0 is the inner radius of the hexapole. We define x and y as the two directions perpendicular to the guide. In the hexapole arrangement, the electric field increases from zero field in the center (r=0) to the maximum value that is equal to $3\frac{V_0}{2}\frac{1}{r_0}$ at the edge of the physical rods(r=r0) as shown in Figure 4.1(left). The average alignment of the molecules within the electric field is defined by the classical expectation value of the cosine of the dipole precession angle $< \cos\theta >$. In the quantum mechanical description, the classical dipole is replaced by the expectation value for the projection of the dipole moment on the inter-nuclear axis so that $< \cos\theta >= \frac{M_J\Omega}{J(J+1)}$. The first order linear Stark effect in the strong electric field E is given by

$$E_{stark} = -\frac{M_J\Omega}{J(J+1)}\mu_{el}E(r) \tag{4.4}$$

where μ_{el} is the electric dipole moment of the polar molecules and θ is the angle between $\vec{\mu}_{el}$ and $\vec{E}$. For NO molecules, $\mu_{el}E \ll B_J$, so only the first order Stark effect is considered as given in Eq.(4.5) and higher order terms are neglected. Here, B_J is

the rotational constant. The Stark shift of a Λ doublet level ΔW_{stark} relative to the zero field center of the Λ doublet components is given by Eq.(4.5).

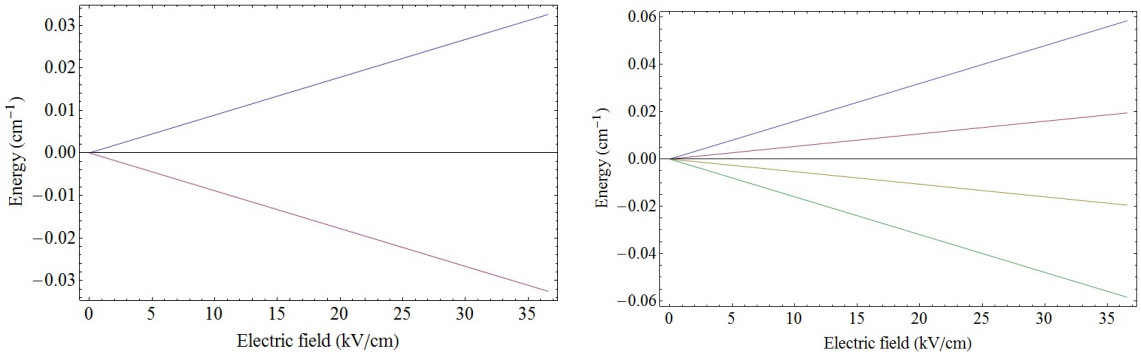

Figure 4.4: Stark shift of the Ω = 3/2, J = 3/2 level (right) and Ω = 1/2, J = 1/2 level (left) of NO. Molecular states in which their potential energy increases (decrease) with the electric field is called the low-field seeking (high field-seeking) states.

$$\Delta W_{stark} = \sqrt{(\frac{\Lambda}{2})^2 + (E_{stark})^2} \tag{4.5}$$

The first order Stark shift was calculated and is shown in Figure 4.4. When an external electric field of several kV/cm is applied to a NO molecule in a low J state, the nearby Λ mix and repel each other due to the Stark effect. The upper level of the Λ-doublet will raise its energy (positive Stark effect, low field seeking states) while the lower levels will decrease in energy (negative Stark effect, high field seeking states). Thus, the inhomogeneous electric field inside the hexapole exerts a force on the low field seeking molecules so that they are deflected towards the axis, whereas the high field seeking states are deflected away from the hexapole axis, and they are lost. In this way, the low field seeking or upper Λ-doublet states are selected and are guided by the hexapole field. Since the Stark effect is inversely proportional to J(J+1), the Stark

effect is weaker for NO in higher J(Figure 4.5). Because of this reason, the hexapole only focused low J states.

Using Eq 4.5, we calculated the Stark shifts of low field seeking particles of $\Pi_{1/2}$ states for J $\leq 15/2$ as a function of rotational quantum number at the field strength of 33kV/cm, as shown in Figure 4.5 where the guided high stark molecules are shown. The vertical sequences in this figure occur because the different states M_J of J have the same rotational energy, but different Stark shifts. Also, the Stark shift decreases with increasing in rotational quantum number in NO because the spacing between Λ-doublet states increases with increasing J. As our slow beam originated from a 77 K temperature source, many stark shifted states are populated and the higher Stark shifted molecules can be observed ($\Omega = 1/2, J = 1/2, M_J = 1/2$) which is about 2% of total population. So, the population of higher stark shifted molecules coming out from the effusive source is about $10^{14}/sec$. These large stark shifted molecules are guided in the hexapole guide. Since the population of the states with lower stark shift is larger as shown in Figure 4.5, most of the molecules escape from the guide.

4.3.1 Computer simulation and its results

In our experiment, the molecules originate from the effusive source at a temperature typically between 70-80 K. with a small nozzle through which the gas flows from a high pressure 0.01 torr to a low pressure 10^{-7} torr directly inside the hexapole guide. Though the temperature of the gas is low, the speeds are high enough so that the movement of the molecules is regarded as classical. The Newton's laws can be used and quantum mechanical description is unnecessary. The magnitude of the force

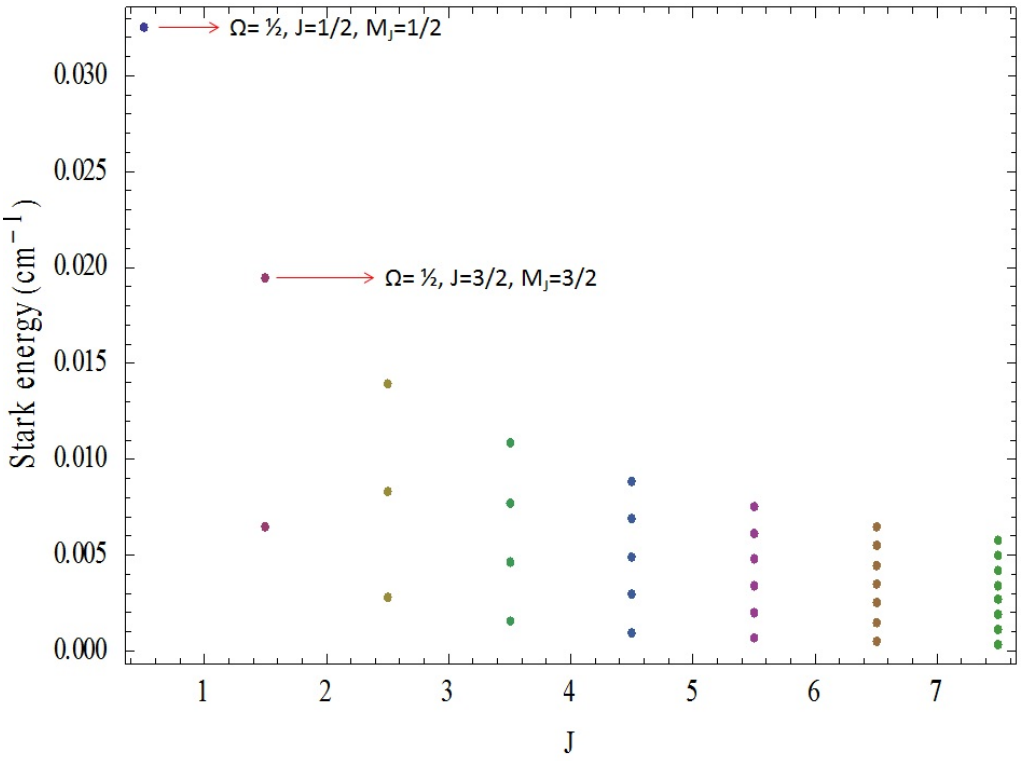

Figure 4.5: The Stark shift of NO as a function of the zero-field rotational energy of low field seeking rotational states for 35kV/cm. The two most Stark-shifted states are shown in the figure.

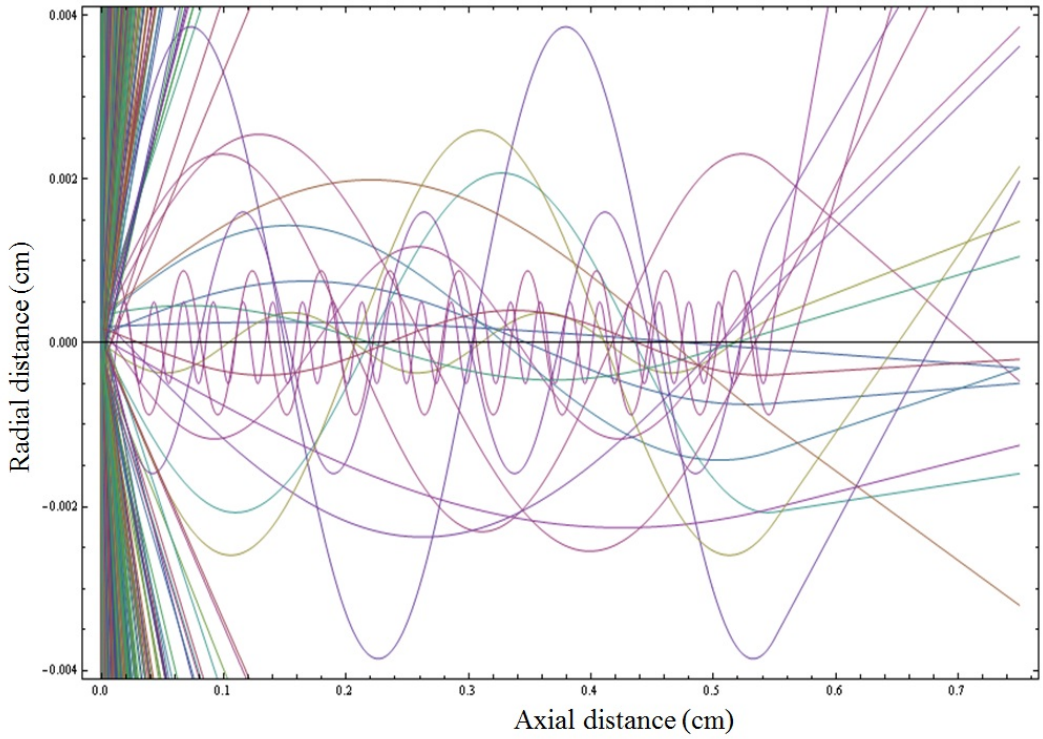

Figure 4.6: Molecules from the effusive source. Trajectory simulation of 1000 NO particles showing he velocity filtering process through the hexapole guide at ± 5 kV electrode voltage. The molecules with transverse velocities below the cutoff velocity are transmitted through the guide. Those molecules which are not guided are lost, also shown in the figure.

experienced by the low field seeking molecules within the hexapole field is given by

$$F = \frac{dE_{stark}}{dr} = -6\mu_{el}V_0\frac{M_J\Omega}{r_0^3 J(J+1)}r = -kr \tag{4.6}$$

Where k is the force constant that depends on the quantum state. The solution of Eq.(4.6) provides simple harmonic motion in the radial direction. For a given electric field gradient, a Monte Carlo code was written in Mathematica for trajectory simulations along the hexapole axis. Results are shown in Figure 4.6 and Figure 4.7. We assume an ideal hexapole potential in calculating the trajectory in the hexapole field regions.

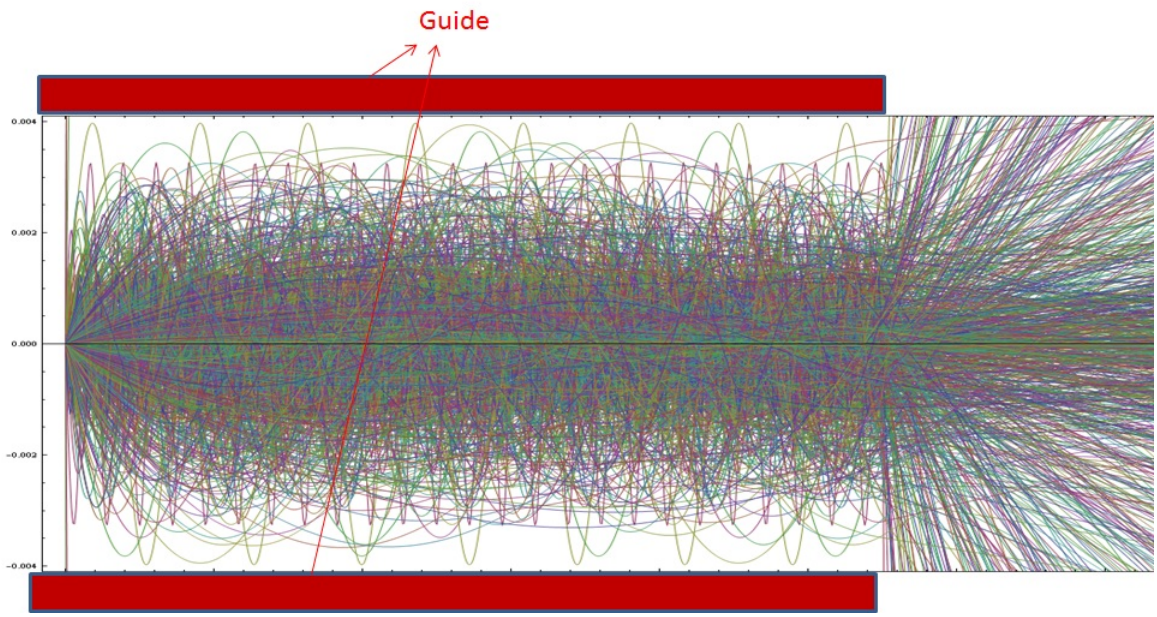

Figure 4.7: Trajectory simulation of 1000 particles in the hexapole guide at guide voltage of $\pm 5kV$.

The radial position of the molecules at time t was calculated with a time step of $\Delta t = 10^{-5}$sec. Transverse velocities were chosen randomly from Boltzmann velocity distribution at 77 K. The initial position was chosen randomly. Straight line trajectories were assumed in all field-free regions as shown in Figure 4.6 without the guide. Those molecules whose velocity was less than the maximum cutoff velocity were guided and transmitted through the hexapole, and are counted as a successful trajectory, whereas other molecules escaped, which is also shown in Figure 4.6. Taking the initial transverse velocity of all the particles (1000) below the cut off velocity randomly, the trajectories was simulated as shown in Figure 4.7. The molecules again execute straight-line trajectories upon the exit from the hexapole. Because the slow molecules have large angular divergence, all the molecules do not make it to the detection region. For the rotatinal state with largest stark shift ($\Omega = 1/2, M_J = 1/2, J = 1/2$), we

find approximately 2% of molecules are guided as shown in Figure 4.6. This can be improved by increasing the guide voltage.

The transverse velocity distribution of the guided molecules was also calculated. Figure 4.8 shows the transverse velocity distribution before and after the guide. To measure the temperature of molecules, the velocity distribution of the guided molecules was measured. The appropriate value of temperature was calculated in the Eq.(4.8) matching the measured distribution. From the guided velocity distribution, we obtained the transverse temperature of guided molecules, T_p=2.5 mK.

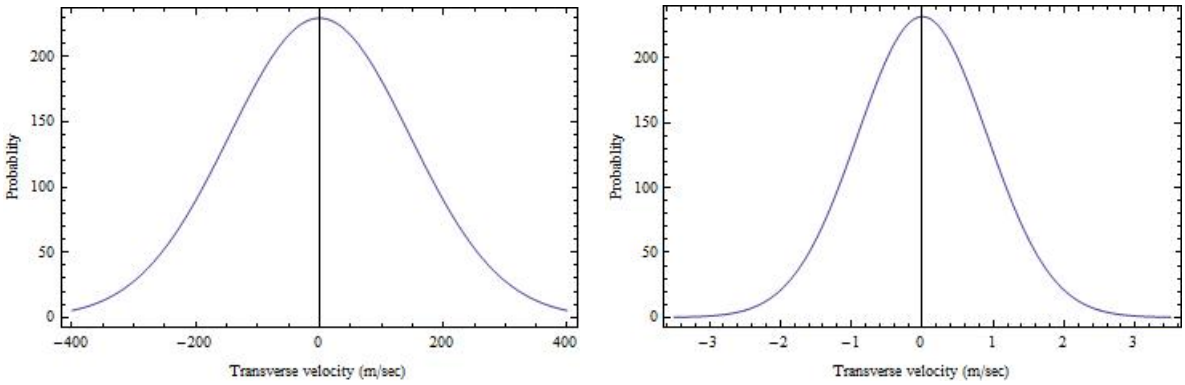

Figure 4.8: Transverse velocity distribution of the molecules before guide (left) and after guide (right) at ± 5kV rod voltage.

4.3.2 Guided molecules

Here we will calculate analytically the guided flux. Initially, both transverse and longitudinal initial temperature of the molecules from the effusive source is the same. To calculate the flux of guided molecules, we assumed that the initial longitudinal (or transverse) velocity distribution of the incident molecular beam at a temperature of 77K satisfies the Maxwell- Boltzmann (or Gaussian) velocity distribution. At

the effusive source condition, the normalized velocity distribution of the emerging molecules and the molecules inside the container are the same, which is given by the following Boltzmann velocity distribution

$$f(v)dv = \frac{2}{\alpha^4}v^3 e[-\frac{v^2}{\alpha^2}]dv \tag{4.7}$$

Where α is the most probable velocity. Integrating over the total velocity gives the fraction of molecules at any temperature range.

The thermal velocity distribution of NO molecules at 77K, and the fraction of the molecules guided below cutoff velocity in the transverse direction, are shown in Figure 4.9. The cut off velocity will be discussed below.

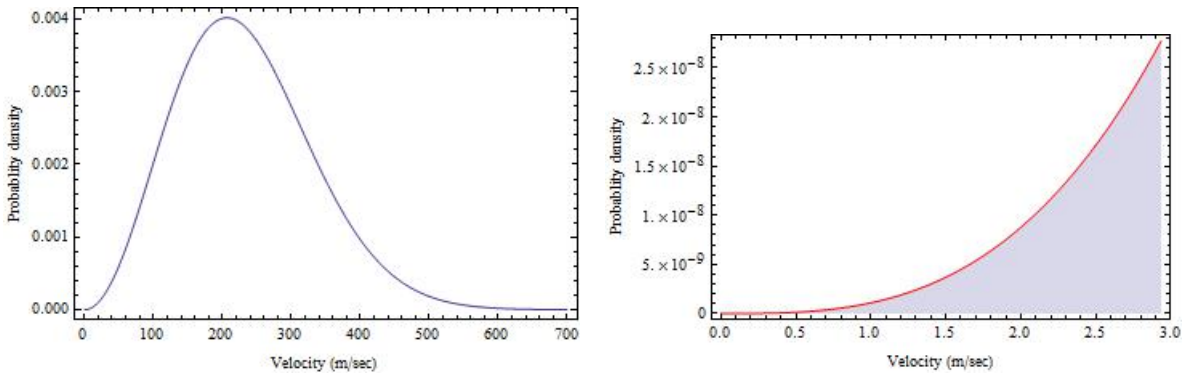

Figure 4.9: Idea of velocity filtering is shown. Velocity distribution at effusive source (left). A considerable guided fraction of the molecules below cut off velocity at 77 K source temperature (right).

The fraction of the molecules in the guide in transverse direction is given by

$$fr = \int_{-v_{max}}^{v_{max}} \frac{m}{\sqrt{2\pi k_B T}} e[-\frac{m{v_r}^2}{2k_B T}]\ dv_r \tag{4.8}$$

A Stark hexapole guide filters by energy, not by angle. If the transverse velocity ($v_r = \sqrt{v_x^2 + v_y^2}$) of the molecules exceeds the cut off velocity v_{max}, the molecules are lost

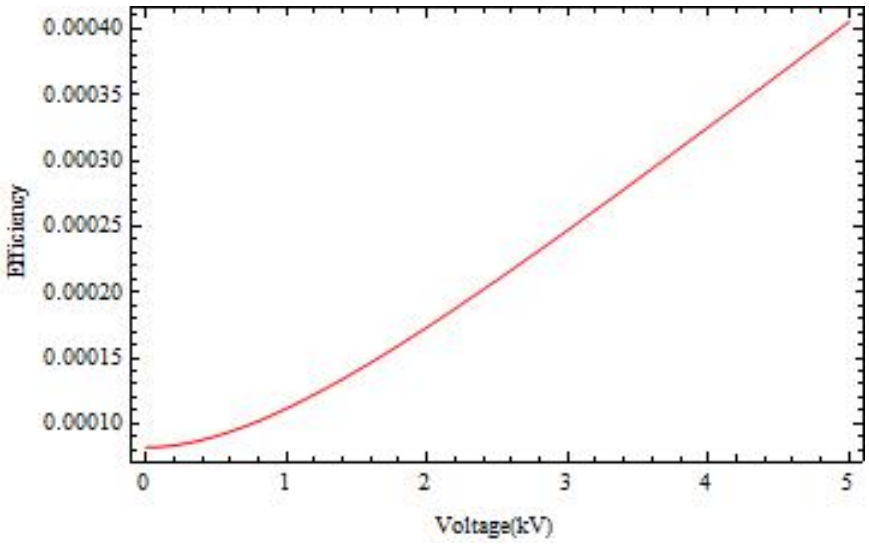

Figure 4.10: Guiding efficiency as a function of rod voltage

from the guide. The maximal transverse cutoff velocity v_{max} at maximum stark shift is given by

$$E_{Maxstark} = \frac{1}{2} m v_{max}^2 \tag{4.9}$$

For particular J, M_J, Ω, V_0, and r0 the maximum Stark shift occurs at r=r0. This cutoff velocity depends on the Stark shift of the molecules, their mass, and on the geometry of the hexapole guide. Since our hexapole surrounds the effusive source nozzle, all molecules that have a transverse kinetic energy below the Stark energy will be guided, whereas the fast ones will be lost over the electrodes barrier.

The output number of particles from the hexapole guide can be calculated as follows: the total flux of the guided molecules or the guiding efficiency can be obtained from the ratio of the integrated area under the transverse velocity profiles of the output molecular beam to the input molecular beam. The total guided low field seeking molecular flux for a given hexapole configuration and for a particular internal state

($\Omega = 1/2$, J = 1/2, $M_J = 1/2$), is given by input number per second multiplied by efficiency. The calculated guiding efficiency at $\pm 5kV$ rod voltage is 10^{-4}/sec so that the guided number of molecules is 10^{12}/sec which agree with the simulation results. The guiding efficiency as a function of guide voltage is shown in Figure 4.10. We also calculated the number density in the hexapole trap as a function of guide voltage (Eq.(4.10)).

$$\Phi 1 = \frac{1}{4} n v_{ave} A \tag{4.10}$$

Where $\Phi 1$ is the loading rate, n is the number density in the trap, A is the cross section area of the guide through which the guided molecules came out, and v_{ave} is the average speed. The number density inside the hexapole trap is calculated in the order of $10^7/cm^3$.

4.4 Experimental procedure

The experimental apparatus is shown in Figure 4.11. It is similar to that described in more detail in the previous chapter. I will discuss only the modifications for this particular experiment. The experimental set-up consists of a cooled source tube assembly and the electrostatic hexapole. The length of our hexapole guide is about 0.55 m. Gas can be let in from a reservoir at room temperature. The reservoir is connected to the stainless tube using Teflon. The tube is connected to the copper can which is held at the specific temperature. The hexapole guide connects the copper can to a separate detection chamber. Molecules are injected into the guide through a stainless still tube (15 cm length and 0.0036 cm radius) that is connected to a nitric

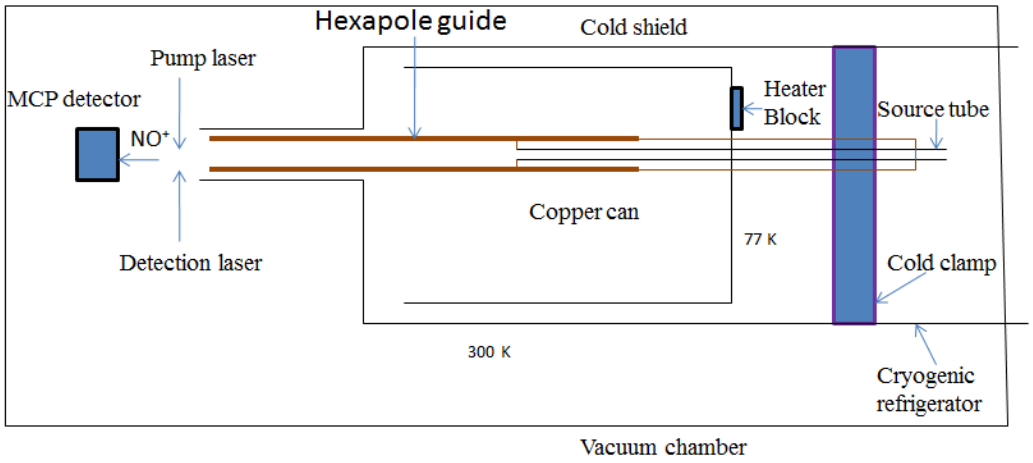

Figure 4.11: Experimental set up showing vacuum chamber and the hexapole guide.

oxide reservoir and equipped with a heater element such that its temperature can be controlled and adjusted. By cooling the tube, the Maxwell-Boltzmann velocity distribution gets compressed and shifts to lower velocities so that the fraction of slow molecules increases. This increases the guided flux. Also, the number of thermally occupied states is reduced, which leads to an improved purity of the guided beam. The gas flow rate through the nozzle can be determined from this pressure rise and the known pumping speed. Most of the injected molecules are not guided and escape into the vacuum chamber as explained earlier. When the gas is flowing, the pressure in the chamber rises to the typical value of a few 10^{-6} torr.

4.4.1 Experimental results

In preparation of eventually magnetically trapping of NO, the NO molecules were directed into the two dimensional straight electric guide. As described above, there is an increase in the number of low-field seeking molecules with a low rotational quantum number because of the guide. The high field seeking molecules are not

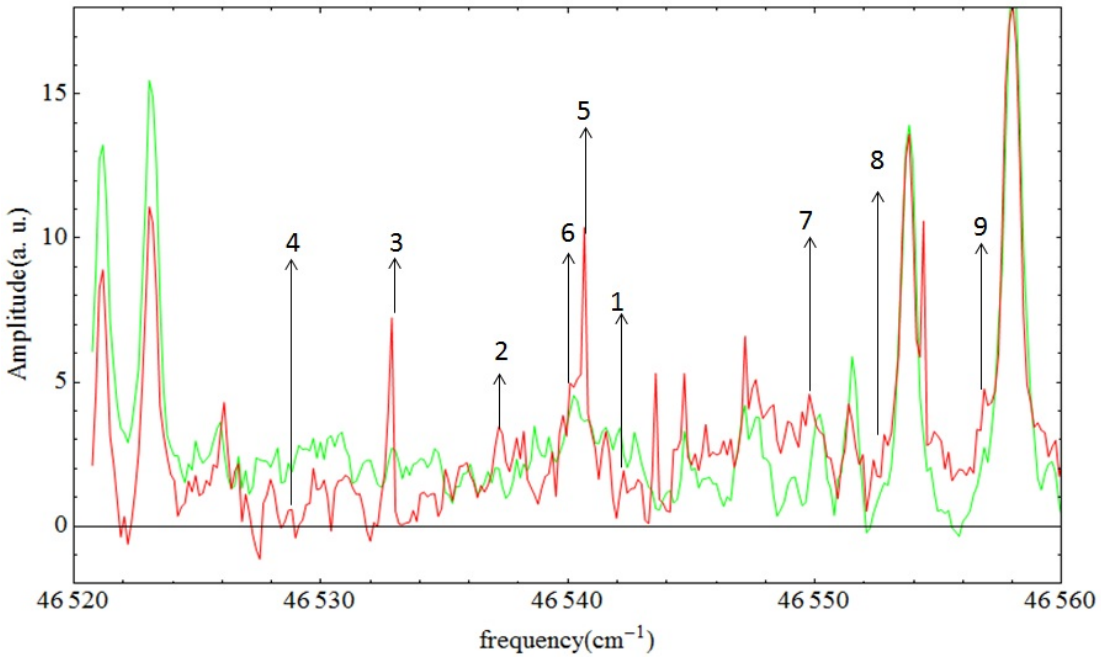

Figure 4.12: Red lines show the signals at ± 5.5 kV guide voltage and green lines show the signals without guide voltage. It can be seen that low rotational low field seeking lines are enhanced. The same lasers were used to take these two spectra.

Table 4.1: Tabulation of the transitions given in Figure 4.12.

Peak	**J**	**Branch**
1	1/2	P21ff
2	3/2	P21ff
3	5/2	P21ff
4	7/2	P21ff
5	3/2	Q21fe
6	5/2	Q21fe
7	3/2	R21ff
8	5/2	R21ff
9	7/2	R21ff

guided by the hexapole. So there is a decrease in the number of high-field seeking molecules that reach the detector. This result is shown in Figure 4.12. We can see in the figure that some transitions are stronger with the guide voltage on, while some transitions are suppressed. The dye laser was scanned in the range to excite $X^2\Pi(\nu'' = 0) \longrightarrow A^2\Sigma(\nu' = 1)$ transitions. The second laser was tuned to 355 nm to ionize the NO molecules from the A state. Some of the enhanced lines are assigned using the theoretical values of allowed transitions as calculated in chapter 2. Those low field seeking molecules in $\Pi_{\frac{1}{2}}$ state are shown in Table 4.1.

Chapter 5

Magnetic trapping of NO

5.1 Introduction

The magnetic moment of an electron spin is one Bohr magneton where 1 $\mu_B = 0.6717$ Kelvin/Tesla= 1.4MHz/Gauss. Most of the atoms on the periodic table, and a great number of molecules have net magnetic moments on the order of 1 Bohr magneton or greater. Molecular radicals with one or two unpaired electrons such as NO, NS, and OH are paramagnetic and magnetic forces are comparatively strong for these molecules. Because of this reason, paramagnetic particles are suitable candidates for magnetic trapping. Cold molecules in a magnetic trap can be used to explore, measure, and control quantum processes.

According to Maxwell's equations, a static electromagnetic field maximum cannot exist in free space in three dimensions. So, the atoms and molecules must be in low-field seeking states to be trapped in free space. The interaction energy of a neutral particle in a magnetic field is generally much weaker than the atoms/molecules thermal energy at room temperature, even at several Tesla. So, atoms/molecules must be cooled before they can be trapped.

5.1.1 Magnetic trapping

The first successful neutral atom trap was the quadrupole magnetic trap [18]. The most common magnetic trap configurations are the quadrupole trap and the Ioffe trap [72, 60]. Comparing the two types of trap, the quadrupole trap's linearly varying

magnetic field is more strongly confining than the quadratically varying field of the Ioffe trap. However, the quadrupole trap has a zero-field point at its center. A magnetic trap using a field in the loffe configuration provides a nonzero field minimum at the bottom of a harmonic potential because of the bias field. Traps having such field configurations have been produced using permanent magnet traps, Ioffe configuration traps[73], and superconducting coils [74].

If the paramagnetic atom or molecule is placed in a magnetic field, the energy of the atoms or molecules varies with the magnetic field strength depending on whether the magnetic dipoles are on average antiparallel or parallel to the magnetic field strength. Those states whose energy increases (dipoles antiparallel) are called low-field seeking states and those of which energy decreases (dipoles parallel) are called high field seeking states. The interaction potential energy of a molecules of a magnetic dipole moment $\vec{\mu}$ with an external magnetic field is given by

$$V_{int} = -\vec{\mu}.\vec{B} = -\mu B cos\theta \tag{5.1}$$

where θ is the angle between the magnetic moment and the magnetic field direction. This energy is minimized when the magnetic moment aligns parallel to the magnetic field. For the conservative potential, the magnetic dipole force on the atom or molecule in the field B is given by

$$\vec{F} = \nabla(\vec{\mu}.\vec{B}) \tag{5.2}$$

The force given in Eq.(5.2) can be used to trap atoms or molecules only in the minimum

of the static magnetic field if the following condition is satisfied.

$$\mu B_{trap} > 0.5mv^2 \tag{5.3}$$

Quantum-mechanically, the magnetic moment of an atom with total electron angular momentum $\vec{J}$ is given by

$$\vec{\mu} = g_J \mu_B \vec{J} \tag{5.4}$$

μ_B is given by Eqs.(2.6). Combining Eqs.(5.1) and (5.4), the magnetic interaction potential energy of molecules in the higher external magnetic fields ceate the linear Zeeman shift given by

$$V_{int} = g_J \mu_B M_J B \tag{5.5}$$

Where, M_J is the projection of J along the direction of $\vec{B}$ as shown in Figure 2.3. M_J is the magnetic quantum number which takes 2J + 1 possible values. M_J is given by

$$M_J = J, J-1, J-2... - J \tag{5.6}$$

The factor g_J is given by [75]

$$g_J = \frac{1}{J(J+1)}[\frac{3}{2} \pm \frac{2(J-1/2)(J+3/2) - 3/2\lambda + 3}{[4(J+1/2)^2 + \lambda(\lambda-4)]^{1/2}}] \tag{5.7}$$

Where λ is the ratio of the spin orbit coupling constant to the rotational constant. The + or - sign correspond to the $^2\Pi_{1/2}$ and $^2\Pi_{3/2}$ states.

The magnetic energies versus magnetic field for the lowest state of the NO within the first excited state $A^2\Sigma^+_{1/2}$, $\nu = 0$ for N=0, J=1/2 and N=1, J=3/2 is calculated using the relations given in [76] and shown in Figure 5.2. I also calculated the Zeeman shift for NO of $X^2\Pi_{3/2}$(Ω = 3/2, J = 3/2) using Eqs.(5.5),(5.6), and (5.7). $X^2\Pi_{1/2}$(

$\Omega = 1/2$, J = 1/2) state does not have first order Zeeman shift. Magnetic energies and their magnetic field dependence for the lowest states of NO within these electronic ground states are shown in Figure 5.1.

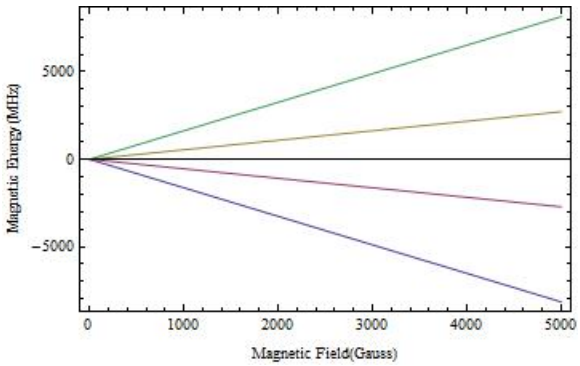

Figure 5.1: Calculated Zeeman shift for NO of $X^2\Pi_{3/2}$($\Omega = 3/2$, J = 3/2).

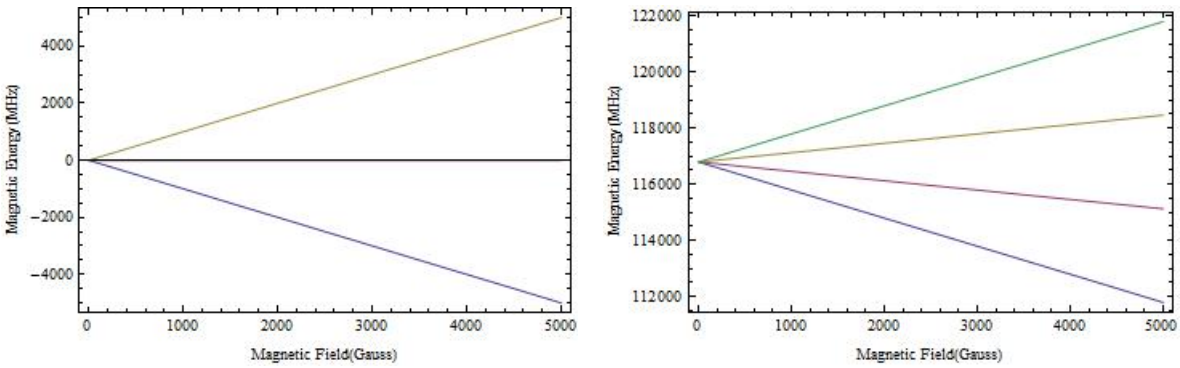

Figure 5.2: Calculated Zeeman shift for NO of $A^2\Sigma^+$ ($\nu = 0$, N=0, J=1/2) (left) and $A^2\Sigma^+$ ($\nu = 0$, N=1, J=3/2)(right)

Because of dissimilar dependence of g_J on J, $^2\Pi_{1/2}$ and $^2\Pi_{3/2}$ states behave differently in the presence of a magnetic field in any rotational state and the trap depth is different for different states. The energy does not vary with the direction of the magnetic field $\vec{B}$, because the dipole moves adiabatically around the changing magnetic

field direction.

There are also other trap loss processes. The trapped gas collides with the background gas and is lost. This loss can be minimized by maintaining good vacuum in the trapping region. The weak-field-seeking Zeeman state may decay to high field-seeking states by emitting a photon. However, these transitions are dipole forbidden and are of low energy making the transition rate astronomically long. When two trapped particles elastically collide, one of them can give sufficient energy to the other so that it escapes from the trap.

Our research group is trying to investigate NO with an aim of trapping low-field seekers NO molecules in the $\Pi_{3/2}$ ground state. The magnetic trap used in our lab is a simple construction producing a spherical quadrupole field using two ring permanent magnets. To construct such a trap, two coaxial permanent ring cylindrical magnets are used which are axially magnetized. The field magnitude produced by the two cylindrical ring magnets is zero at the midpoint between them, creating a local field minimum in free space. This field minimum acts as a potential minimum where the particle remains in the low field-seeking Zeeman level.

5.1.2 Why NO in a permanent magnet trap ?

The $^2\Pi_{1/2}$ ground state has no first order Zeeman shift and the spin orbit excited state $^2\Pi_{3/2}$ has Zeeman shift of 1.6 μ_B. Also, as the rotational level of the $^2\Pi_{1/2}$ ground state increases, the $^2\Pi_{1/2}$ and $^2\Pi_{3/2}$ ground states mix with each other so that effective Zeeman shift for the $^2\Pi_{1/2}$ ground state increases.

Permanent magnets trap can be a good choice to trap atoms/molecules, rather

than the water-cooled coils and electromagnetic traps. It is possible to get much larger field gradient for low cost. The reduced size of the magnets allows us to match the volume of the vacuum chamber and significant optical access. One disadvantage of permanent magnets trap is the inability to turn the field on and off during the loading of slow molecules. Each magnet has the surface magnetization of more than 5 kG. When comparing to the coil electromagnetic trap, a large current and large number of turns is required; such a current is impossible in practice at room temperature. Superconducting coils can produce this large field, but it is complex and expensive. NdFeB magnets can have remnant magnetization of up to 12kG and intrinsic coercivity of 18 kOe. Because of those reasons, this magnets are highly resistant to demagnetization[73]. I also calculated the trap depth for a pair of anti-Helmholtz coils. The analytical expressions were taken from [59]. The trap depth is small as compared to the trap depth due to two ring magnets. The Mathematica codes to calculate the trap depth is shown in Appendix D.

The method to trapping molecules will be feasible for any molecules with $^2\Pi$ ground state. Molecules could be OH and NS. The effective magnetic dipole moment of OH in its J = M_J = 3/2 state is 1.2 μ_B. OH ground state molecule is best described by Hund's case (a). In this molecule, the spin Σ=1/2 and orbital Λ= 1 angular momenta are strongly coupled to the molecular axis giving total angular momentum projection of Ω = 3/2 and 1/2. The Ω = 1/2 state lies 126 cm^{-1} above Ω = 3/2 state[77]. The ground state splitting of NS is 221.5 cm^{-1}. NS is an unstable open-shell molecule. Its electronic structure is similar to nitric oxide. The experimental value of dipole

moment of NS is 1.8 ± 0.02 D for the $^2\Pi_{1/2}$ and $^2\Pi_{3/2}$ states [78].

5.2 Permanent magnet trap

Our permanent magnet trap consists of two axially-magnetized permanent magnets symmetrically positioned and aligned along the z axis. These magnets produce the quadrupole field increasing along all directions and the field minimum at the center. NO molecules can be trapped in the minimum of this trap through the interaction of the total magnetic moment of NO with trap's inhomogeneous magnetic field. Our permanent magnet trap is not the first use of permanent magnet trapping. In 1995, Ramdall G. Hullet group at Rice University used the six axially magnetized, cylindrical, high-flux NdFeB permanent magnets, positioned and aligned along three mutually orthogonal axes in an Ioffe configuration [73]. Near the center of the trap, the potential experienced by the atoms is harmonic with an oscillation frequency of 10^2 Hz. Laser cooled and Zeeman slowed atomic beam were loaded into the trap. They trapped approximately 4×10^8 ground state lithium atoms initially at 1.1 mK kinetic temperatures and $8 \times 10^{11} cm^{-3}$ peak densities. The life time of trapped atoms was 240 seconds. The two magnets along z axis were used to produce the bias field to stop Majorna transitions and other 4 magnets in the x-y plane were used to produce the quadrupole field.

I wrote the computer programming code to design the permanent magnets Zeeman slower. I also simulate the motion of Rb atoms in the slower as shown in Appendix A. We derived and calculated the trap depth along x, y, z, x=y,y=z and x=z directions

of two, four, and six axially magnetized, high-flux NdFeB rectangular permanent bar magnets, positioned and aligned along three mutually orthogonal axes. The trap depth calculation Mathematica code due to bar magnets is given in Appendix C. The analytical expressions were taken from [79]. We also derived the trap depth and we calculated the trap depth along x, y, z, x=y, y=z and x=z directions of two, four, and six axially magnetized, high-flux NdFeB ring cylindrical and cylindrical permanent magnets. The Magnets are positioned and aligned along mutually orthogonal axes. The derivation will be discussed below. Finally, our use of two permanent ring magnets in building NO traps is motivated by the large trap depth and the desire to have good optical access to the trapped NO along with overall experimental simplicity. The schematic of two ring permanent magnets trap is shown in Figure 5.3 and the machine drawing is shown in Appendix G.

We derive the trap depth between the two ring permanent magnets as follows.

$$B(r) = -\mu_o \nabla \Phi(r) \tag{5.8}$$

Where B(r) is the magnetic field at r, $\Phi(r)$ is the scalar potential and μ_o is the permeability of free space. For cylindrical permanent magnets, $\Phi(r)$ is given by

$$\Phi(r) = \sum_{i=1}^{N} \frac{1}{4\pi} \int \frac{\hat{n_i} \cdot \vec{M_i}}{|r - r'|} da' \tag{5.9}$$

Where sum accounts for contribution from the faces of ring magnets, M is the magnetization, $\hat{n_i} \cdot \vec{M_i}$ is the surface charge density of the face. In the case of the trap, only the inner face of the magnets contribute to the trap depth as the outer faces are sufficiently far from the trap centers, but I take into account the contribution of both

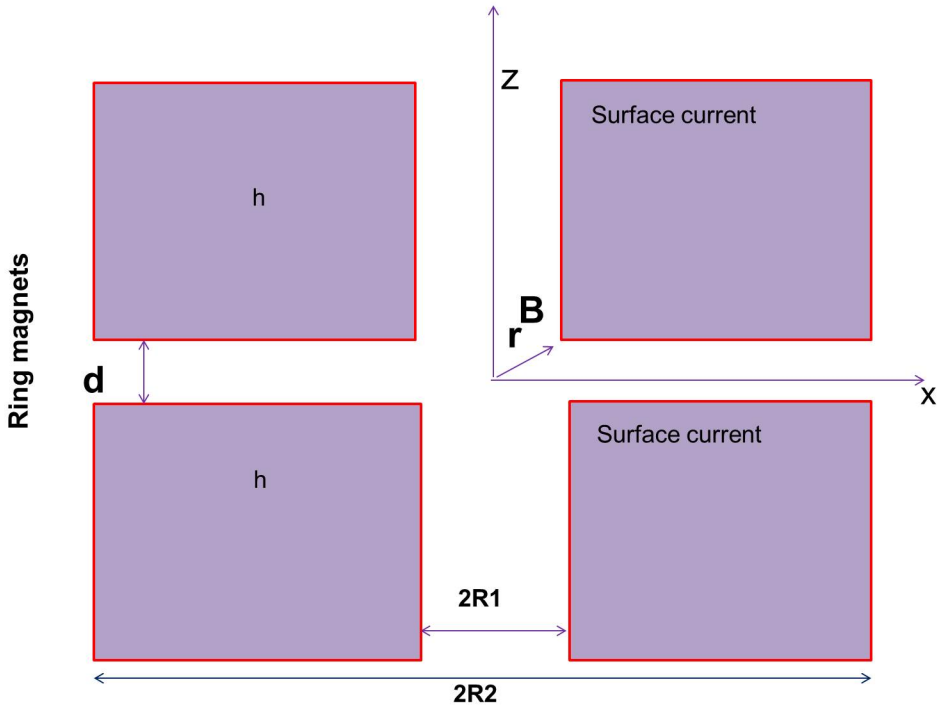

Figure 5.3: Syhematic of two ring magnets trap.

inner and outer surface in my calculation. For two cylindrical magnets, N = 4, for two ring cylindrical magnets, N = 8 and etc. The scalar potential from above expression is given by

$$\Phi(r,z) = \frac{M}{4\pi}\int_0^{2\pi}\int_0^{a}\frac{r'dr'd\phi'}{|r-r'|} \tag{5.10}$$

We derived scalar potential for the inner surface performing the integrals, and then

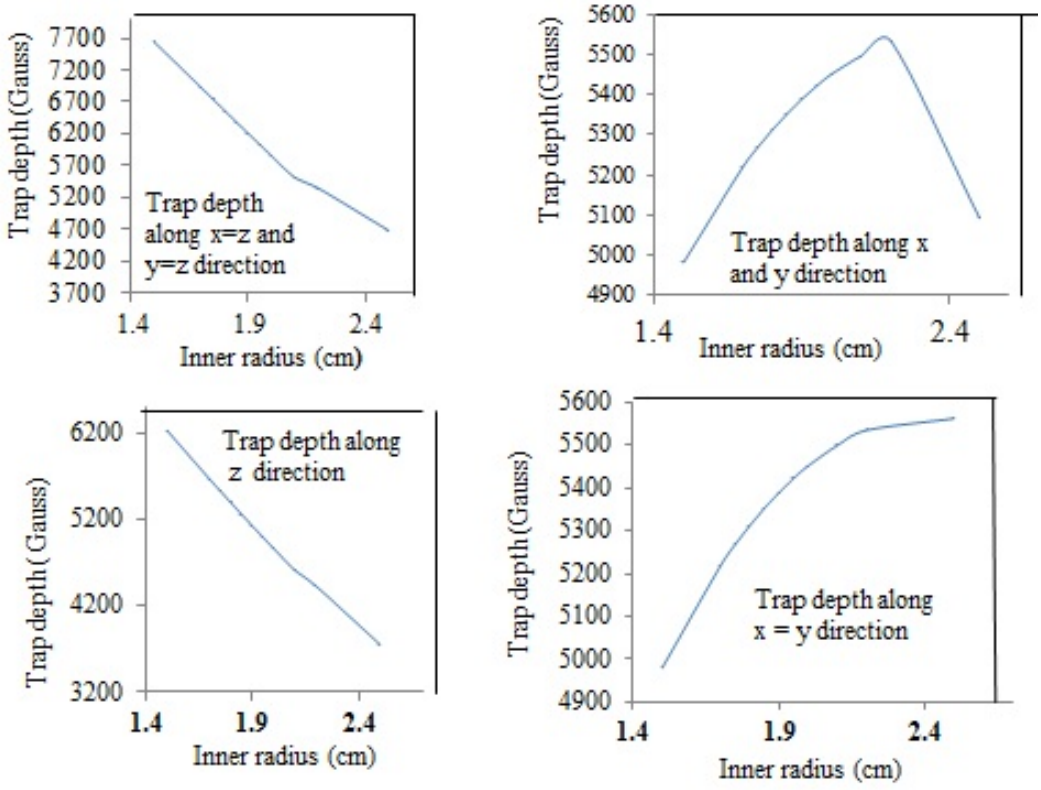

Figure 5.4: Trap depth as a function of inner radius of two permanent ring mangnets.

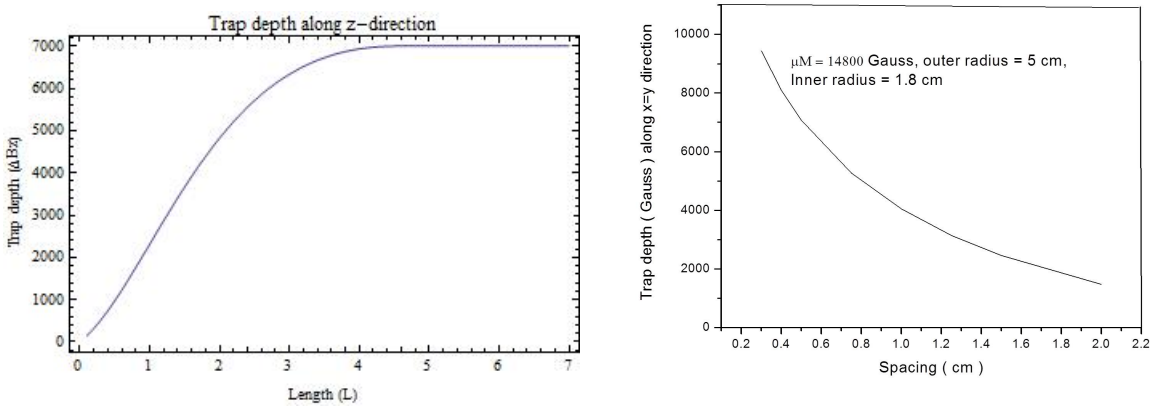

Figure 5.5: (a)The trap depth as a function of thickness of each of the ring magnets (left). (b) The trap depth as a function of spacing between two magnets (right).

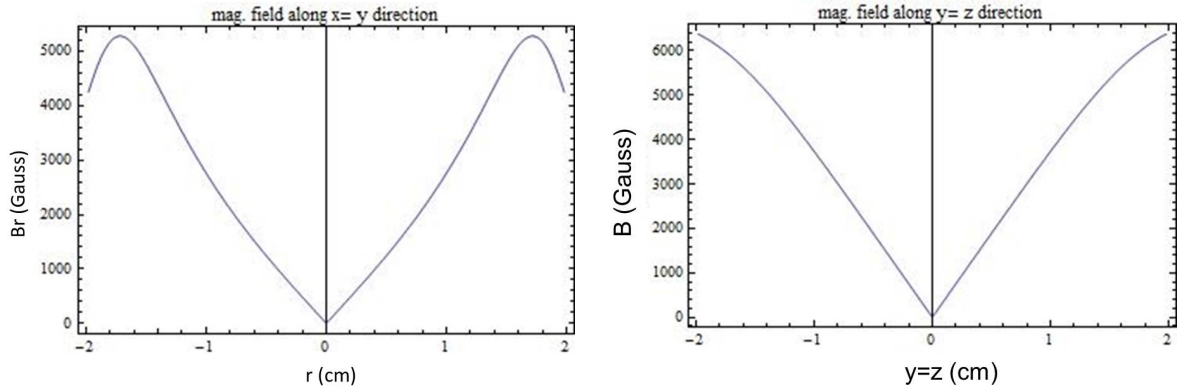

Figure 5.6: Plot of the calculated Br(r, z=0) for the two ring magnets of the given geometry (left) and plot for B(y=z) (right)

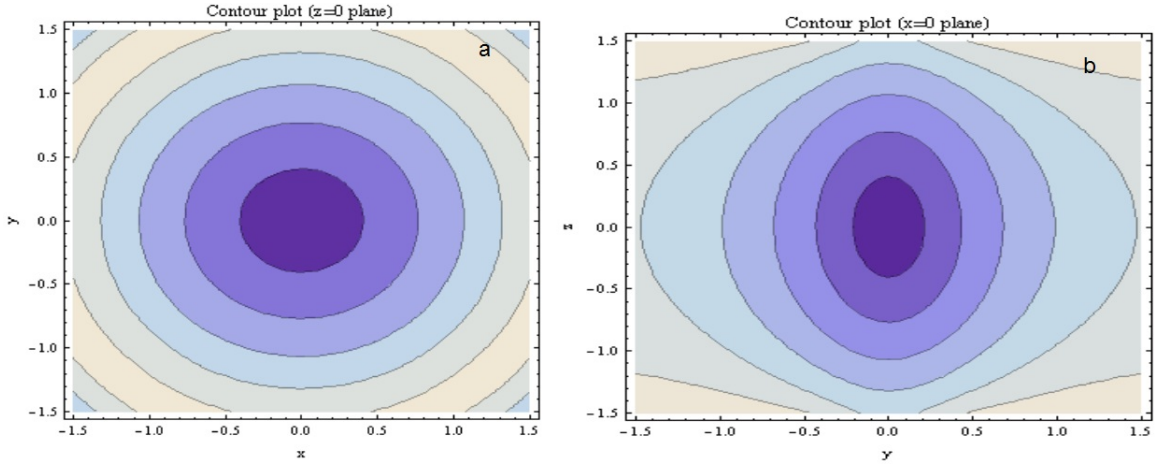

Figure 5.7: A contour plot of field magnitude of the quadrupole trap in the central quadrupole trap region in two ring permanent magnets configuration, (a) x-y plane(left) and (b) in y-z plane(right)

the scalar potential is given by

$$\begin{aligned}\Phi(r,z) &= -\frac{\mu_o M}{4\pi}\sqrt{r^2+z^2} \\ &\quad +\frac{\mu_o M}{4\pi}(\sqrt{R1^2+r^2+z^2-2rR1Cos\phi'} \\ &\quad +rCos\phi'(Log(2\sqrt{R1^2-2rR1Cos\phi'+r^2+z^2}+2R1 \\ &\quad -2rCos\phi')-Log(2\sqrt{r^2+z^2}-2rCos\phi'))\end{aligned}$$

Where R1 is the radius of the cylindrical magnet. The axially magnetized magnet produces the magnetic field which is given by Eq.(5.8). We solve the Eq. 5.8 using the potential in Eq. 5.11 for two ring magnets numerically by Mathematica. The trap depths of the two ring magnets were calculated as a function of inner radius as shown in Figure 5.4. Finally, we chose the inner radius to be 1.8 cm and outer radius to be 5 cm because at these values, we have enough trap depth with over all simplicity to load NO gas into the trap. We also calculate the trap depth as a function of spacing between two ring magnets as shown in Figure 5.5 (right) and finally we choose this number to be is 0.75 cm so that we will have enough space for optical access to the center of the trap. As shown in Figure 5.5(left), the thickness of the each of the ring magnets was chosen to be 2.5 cm because at this point, the trap depth reaches the maximum and after that it saturates.

I calculated the trap depth for a variety of diameters, the spacing between magnets, the magnetization, and the inner radius, which is shown in Appendix E. The calculated trap depth for our specification is shown in Figure 5.6. Figure 5.7 shows the magnetic

Table 5.1: Specification of NdFeB magnet N52.

Specification	Values
Diameter	10 cm.(OD) and 3.6 cm.(ID)
Thickness	2.5 cm.
Tolerances	$\pm 0.004" \times \pm 0.004" \times \pm 0.004"$
Material	NdFeB, Grade N52
Plating/Coating	Ni-Cu-Ni (Nickel)
Magnetization direction	Axial (Poles on Flat Ends)
Max Operating Temp	80 °C
Brmax	14,800 Gauss
BHmax	52 MGOe
Quantity	2 pieces
Company and URL(China)	Permanent Magnetic Co.,Limited, www.magnets-china.net

field symmetry of the x-y plane at z = 0 and y-z plane at x=0 in contour plots. The linearity of the field gradients near the center of the trap center is indicated by the even spacing of the potential lines. Figure 5.7 plot also shows the difference in axial and radial gradients for the quadrupole trap that is along the symmetry axis of the two ring magnets (z-axis). To make the magnets compatible with the high vacuum chamber, ring magnets are coated with nickel because nickel plating prevents corrosion. The specification of NdFeB magnets we have ordered is shown in Table 5.1. I also calculated the trap depth between two ring permanent magnets using analytical expressions. The analytical expressions for a ring magnet are discussed in [80, 81, 82]. The Mathematica code and the expressions to calculate the trap depths are given in Appendix B. The analytical and the calculated trap depths exactly match.

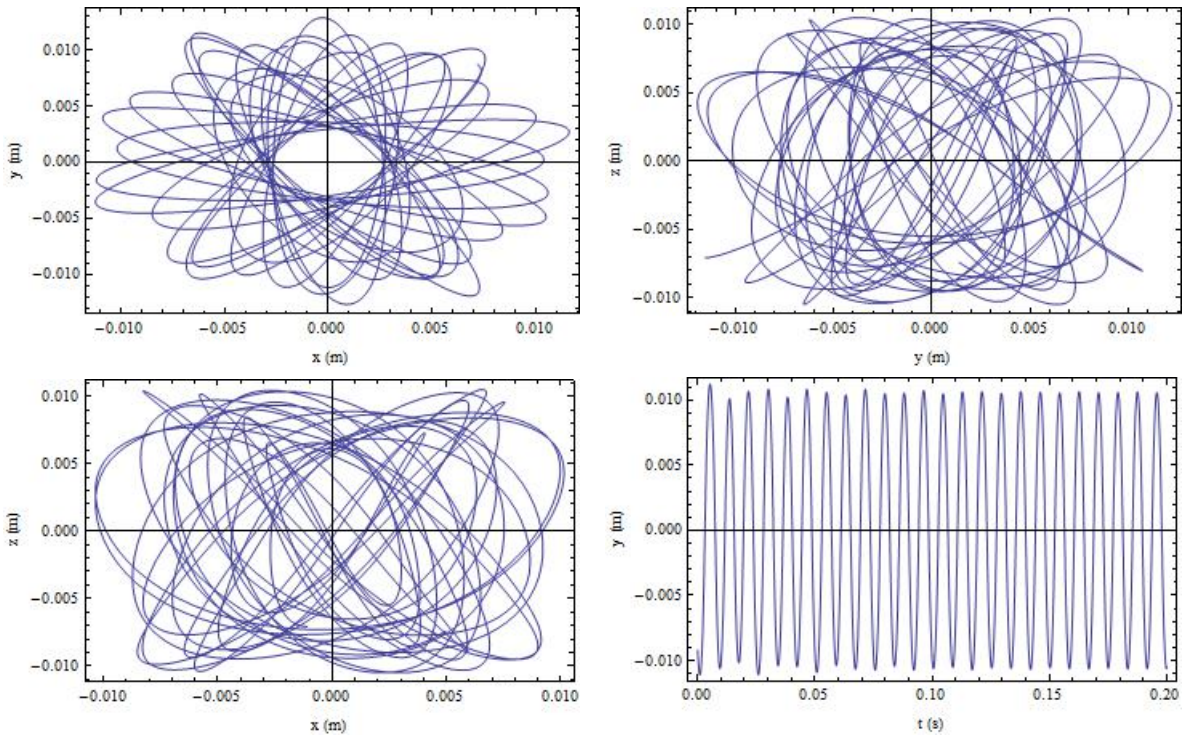

Figure 5.8: Trajectory simulation of the NO particle in the permanent magnet trap. (1) Position of particle in the x, y plane (top left). (2) Position of particle in the y, z plane (top right). (3) Position of particle in the x, z plane (bottom left). The velocity of the particle is a random number below the trap depth. As the trap potential is conservative, the particles total energy is conserved and the particle remains in the trap forever (bottom right).

5.3 Monte Carlo methods

5.3.1 Trajectory of neutral NO in trap

In this section, we report some results of the computational trajectory simulation of the trapped NO. We solved the classical equations of motion to get the trajectories of the NO within the trap. We calculated the trajectory of the particles under various experimental conditions such as trap depth, NO gas temperature, time etc. In these simulations, low tail Boltzmann distribution of velocity of NO less than the cut off velocity was chosen and guided from the hexapole guide and loaded into the trap with some reasonable set of initial conditions. The magnetic field force on the particle inside the trap is given by the Eq.(5.2).

The numerical integration of the trajectories simulation was done using the same process as described in the chapter 4. The interactions between trapped particles and the hyperfine structure are neglected in all of the simulations described in this thesis. For trajectory simulations, a particle's initial velocity is chosen randomly from a Maxwell-Boltzmann distribution at some specified temperature and the particles x, y, and z coordinates are generated randomly. Some of the results of these trajectory simulations are shown in Figure 5.8. The particles follow simple classical orbits in the magnetic trap since the trapping potential is conservative. If the atom's initial energy is below the trap depth, it will remain in the trap until lost from collisions.

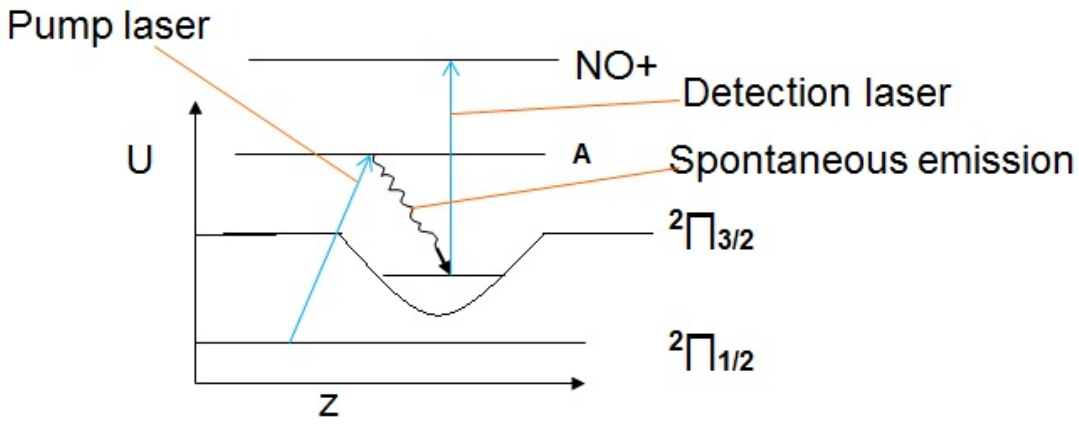

Figure 5.9: Optical pumping

5.3.2 Loading magnetic trap and optical pumping

We also calculated the loading rate of the magnetic trap. The distance between the exit channel of the guide and the other end of ring cylindrical magnet is about 29 mm. The geometric fraction is given as $\frac{\int_0^{2\pi} d\phi \int_0^{36} cos\theta sin\theta d\theta}{\int_0^{2\pi} d\phi \int_0^{90} cos\theta sin\theta d\theta}$ and the number of low field seeking particles loaded into the trap per second is given by the output number of particles per second from the guide multiplied by that fraction. So, because of the large divergence of the molecules coming out from the guide, only about 2% ($10^{10}/s$) molecules are loaded into the magnetic trap.

In summary, the total number of molecules coming out from the effusive source is $10^{16}/s$. Out of these, the highest stark shifted molecules ($\Omega = 1/2, J = 1/2, M_J = 1/2$) is 2% ($10^{14}/s$). Only 2% are guided in our hexapole guide ($10^{12}/s$). This result also agrees with the analytical result. Number of particles interacting with probe laser is 10^7/sec. In the optical pumping process as shown in Figure 5.9, the population of molecules in $\Pi_{1/2}$ states are excited to the excited state A by pump laser. The

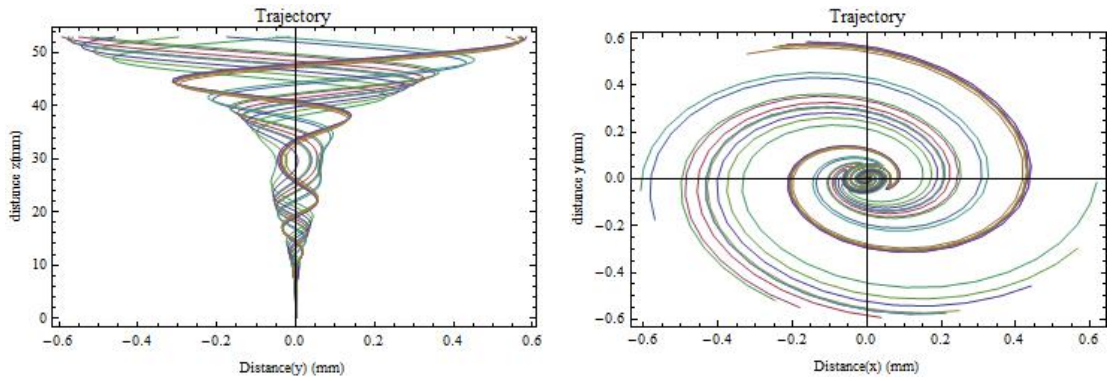

Figure 5.10: Ions trajectory in y-z plane (left) and in the x-y plane (right) in the electromagnetic field condition of our example

population undergoes spontaneous emission to the $\Pi_{1/2}$ and $\Pi_{3/2}$ states and populates different rovibrational states. Only 1% (10^5)/sec molecules are transferred to $\Pi_{3/2}$ by optical pumping. Since $\Pi_{3/2}$ state has a large magnetic moment, these molecules can be trapped.

5.3.3 Trajectory of ions and time of flight

In this section, we will see the motion of the charged particle, their velocity and the kinetic energy in the electromagnetic field condition. The laser 355 nm is used to ionize the molecules. Those ionized molecules move under the electromagnetic condition towards the detector. A charged particle moving in a magnetic field will feel a force that is proportional to both the strength of the magnetic field and the velocity. Also, this force is perpendicular with both the magnetic field and the velocity of the charged particle. The stationary particle and the particle moving in the direction of the magnetic field lines will not experience a force. Because of this, charged particles move in a circle (or more generally, a helix) around magnetic field lines; this

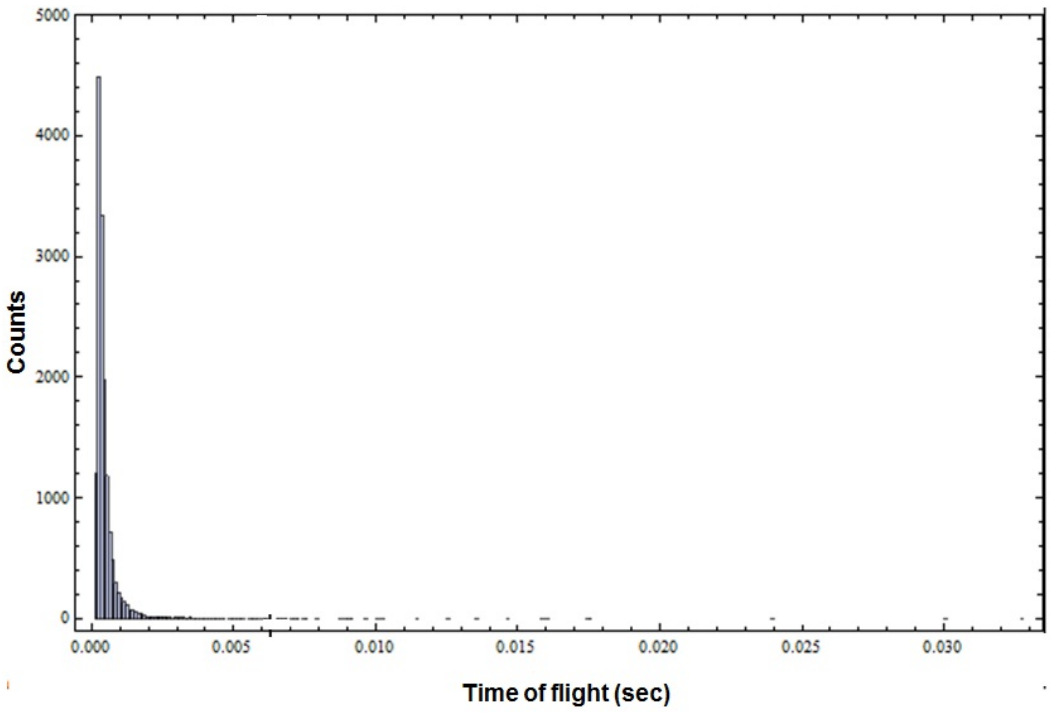

Figure 5.11: Time of flight

is called cyclotron motion. The magnetic fields can't do work on a charged particle and a magnetic field alone cannot speed up or slow down a charged particle because the magnetic field is always perpendicular to the motion. It changes the particle's direction.

The equation of motion of the charged particle of mass m and charge q and velocity $\vec{v}$ in electric field $\vec{E}$ and magnetic field $\vec{B}$ is given by

$$\vec{F} = m\frac{d\vec{v}}{dt} = q(\vec{E} + \vec{v} \times \vec{B}) \tag{5.11}$$

It was assumed that the charged particles do not collide and their motion is determined by the fields only. For $\vec{E}$=0, this equation can be written as

$$\frac{m}{2}\frac{d\vec{v}}{dt}.\vec{v} = \frac{q}{2}(\vec{v} \times \vec{B}).\vec{v} = 0 \tag{5.12}$$

The right side is equal to zero because $\vec{v} \times \vec{B}$ is perpendicular to both $\vec{v}$ and $\vec{B}$. Then,

$$\frac{d}{dt}(\frac{mv^2}{2}) = 0 \tag{5.13}$$

This means the kinetic energy of the charged particle in the absence of an electric field is constant. Taking the second derivative of the Eq. 5.11 with $\vec{E} = E_z\hat{z}$ gives

$$\begin{bmatrix} \frac{d^2v_x}{dt^2} \\ \frac{d^2v_y}{dt^2} \\ \frac{d^2v_z}{dt^2} \end{bmatrix} = (\frac{q}{m})^2 \cdot \begin{bmatrix} -(B_y^2 + B_z^2) & B_xB_y & B_xB_z \\ B_xB_y & -(B_x^2 + B_z^2) & B_yB_z \\ B_xB_z & B_yB_z & -(B_x^2 + B_y^2) \end{bmatrix} \cdot \begin{bmatrix} v_x \\ v_y \\ v_z \end{bmatrix} + (\frac{q}{m})^2 \cdot \begin{bmatrix} 0 & B_z & -B_y \\ -B_z & 0 & B_x \\ B_y & -B_x & 0 \end{bmatrix} \cdot \begin{bmatrix} E_x \\ E_y \\ E_z \end{bmatrix}$$

This matrix equation was solved numerically for the ion trajectories. A Mathematica simulation code was written to simulate the ion motion. Figure 5.10 shows the trajectory of the charged particles in an electromagnetic condition. We also simulate the trajectory of 5000 ions to calculate the time of the flight of the ions towards the detector. It is shown in Figure 5.11.

5.4 Experimental

The magnetic trap as described in this chapter was kept inside the detection chamber. MCP plate was redesigned (Appendix G) and was kept with magnetic trap so that it can detect the charged particles coming from the magnetic trap. One of the ring magnets was grounded and the 300 V was applied to the other ring magnet. -2000 V was applied to the ion collector (MCP). The ions formed inside the magnetic trap are accelerated towards the detector.

We checked the compatibility of the REMPI detection in the magnetic trap. We took the spectra of background NO in the experimental set up described in the previous

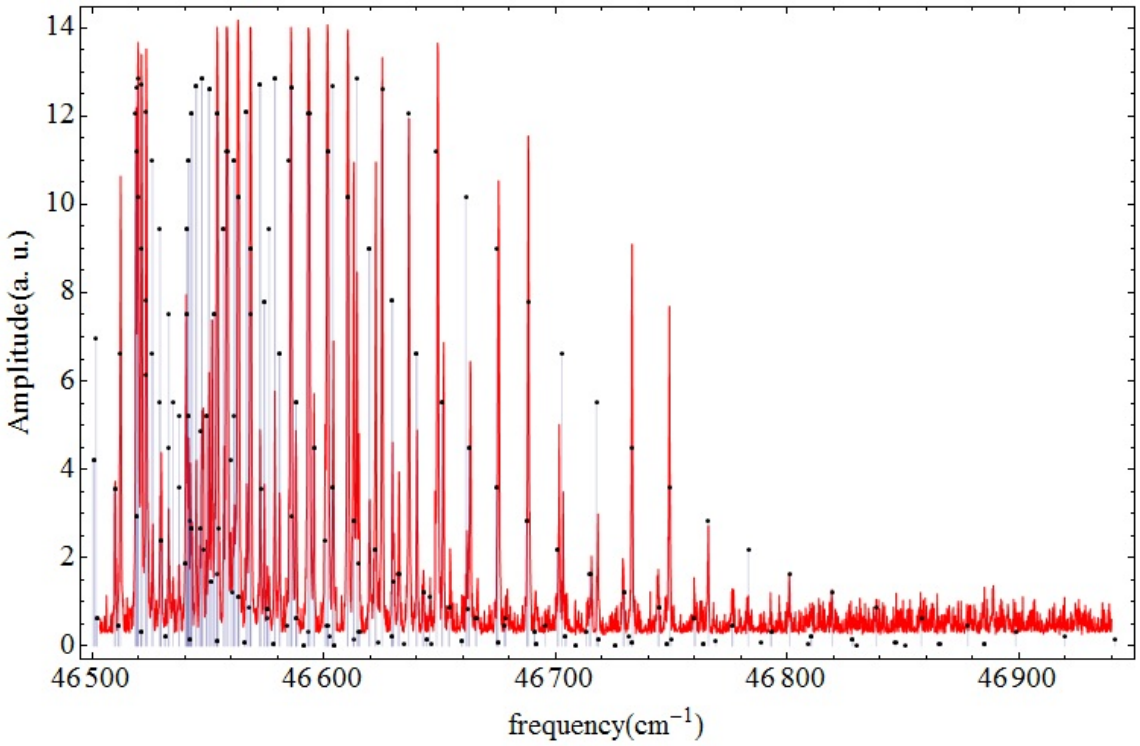

Figure 5.12: NO spectra in the magnetic trap. Red lines are the experimental spectra and blue lines are the theoretical spectra.

sections. The NO REMPI spectra was taken in the long range of wavelength from 213 nm (46948.4 cm^{-1}) to 215 nm (46511.6 cm^{-1}) in the magnetic trap as shown in Figure 5.12. We find that REMPI worked well and should be usable to detect trapped NO for further experiments.

Chapter 6

Summary and conclusion

Results of a new source for cold molecular production using activated carbon was presented, which may eliminate the need for ablation loading in buffer gas cooling experiments. It would be placed between the two strong ring permanent magnets that create the quadrupole magnetic trap of around 300 mK trap depth. Molecular NO was produced by the charged activated carbon after sending the pulse of current. It could be also produced in a cell that thermalized with the He buffer by elastic collision with the buffer gas. The buffer gas dissipates the translational energy of the NO molecules by allowing them to sink into the conservative quadrupole magnetic trapping field. As this dissipation scheme does not depend on any particular energy levels of NO, many molecules can be trapped there in low-field seeking states whose kinetic energies are below the trap depth. We also presented the experimental results of production of low field seeking NO in the lowest rovibrational state. We also checked experimentally the compatibility of the REMPI detection in the magnetic trap and we find that REMPI worked well and should be usable to detect trapped NO for further experiments.

We also presented a computer simulation method for filtering, guiding and magnetic trapping of cold molecular NO. In the filtering process, the low field electric seeking molecules interact with an inhomogeneous electrostatic field of a hexapole guide which is exploited to select the slow molecules from a cold molecular source. The resulting cold fraction in the non-magnetic $^2\Pi_{1/2}$ ground state can be directed into a magnetic

trap where it may be optically pumped into the $^2\Pi_{3/2}$ fine structure state which can be magnetically trapped. Also, we present the computer simulation of the trajectory of the charged particles in the electromagnetic field. We present the simulation of the time of flight of 1000 charged particles in the electromagnetic field.

References

[1] J. Danielak, U. Domin, M. Kepa, and Z. Rytel, J. Mol. Spectrosc. **181**, 394402 (1997).

[2] C. G. Townsend, N. H. Edwards, C. J. cooper, K. P. Zetie, and C. J. Foot, Phy. rev. A **52**, 1423 (1995).

[3] M. Anderson, J. Ensher, M. Matthews, C. Wieman, and E. Cornell, Science 269 **198**, (1995).

[4] B. D. Marco and D. Jin, Science 285 **1703**, (1999).

[5] R. Onofrio, C. Raman, J. M. Vogels, J. R. Abo-Shaeer, and A. P. Chikkatur, Phys. Rev. Let. **85**, 2228 (2000).

[6] M. O. Mewes, M. R. Andrews, D. M. Kurn, D. S. Durfee, and anTownsend C. G., Phys. Rev. Let. **78**, 582 (1997).

[7] H. L. Bethlem, G. Berden, F. M. H. Crompvoets, R. T. Jongma, A. J. A. VanRoij, and G. Meijer, Nature **406**, 491 (2000).

[8] E. R. I. Abraham, N. W. M. Ritchie, W. I. McAlexander, and R. G. Hulet, J. Chem. Phys. **103**, 7773 (1995).

[9] S. Jochim, M. Bartenstein, A. Altmeyer, G. Hendl, C. Chin, J. H. Denschlag, and R. Grimm, Phys. Rev. Lett. **91**, 240402 (2003).

[10] R. deCarvalho, J. M. Doyle, B. Friedrich, T. Guillet, J. Kim, D. Patterson, and J. D. Weinstein, Eur. Phys. J. D **7**, 289 (1999).

[11] J. D. Weinstein, R. deCarvalho, J. Kim, D. Patterson, B. Friedrich, and J. M. Doyle, Phys. Rev. A **57**, R3173 (1998).

[12] H. F. Hess, Phys. Rev. B **34**, 3476 (1986).

[13] N. Masuhara, J. M. Doyle, J. C. Sandberg, D. Kleppner, T. J. Greytak, H. F. Hess, and G. P. Kochanski, Phys. Rev. Lett. **61**, 935 (1988).

[14] J. R. Bochinski, E. R. Hudson, H. J. Lewandowski, G. Meijer, and J. Ye, Phys. Rev. Lett. **91(24)**, 243001 (2003).

[15] H. L. Bethlem, G. Berden, and G. Meijer, Phys. Rev. Lett. **83(8)**, (1999).

[16] T. Junglen, T. Rieger, S. A. Rangwala, P. W. H. Pinkse, and G. Rempe, Phys. Rev. Lett. **92**, 22300 (2004).

[17] S. A. Rangwala, T. Junglen, T. Rieger, P. W. H. Pinkse, and G. Rempe, Phys. Rev. A. **67**, 043406 (2003).

[18] A. L. Migdall, J. V. Prodan, W. D. Phillips, B. T. H., and H. J. Metcalf, Phy. rev.Lett. **54 (24)**, 2596 (1985).

[19] W. D. Phillips, J. V. Prodan, and H. J. Metcalf, J. Opt. Soc. Am. B2 **11**, (1985).

[20] W. Petrich, M. H. Anderson, J. R. Ensher, and E. A. Cornell, Phys. Rev. Lett. **74**, 3352 (1995).

[21] M. Gupta and D. Herschbach, J. Phys. Chem. A **103**, 10670 (1999).

[22] E. Narevicius *et al*, Phys. Rev. Lett. **103201**, (2007).

[23] L. B. Hendrick *et al*, Phys. Rev. Lett. **88**, 133003 (2002).

[24] N. Edvardas *et al*, Phys. Rev. Lett. **100**, 093003 (2008).

[25] J. D. Weinstein, R. deCarvalho, T. Guillet, B. Friedrich, and J. M. Doyle, Nature **395**, 148 (1998).

[26] J. Kim, B. Friedrich, D. P. Katz, D. Patterson, J. D. Weinstein, R. deCarvalho, and J. M. Doyle, Phys. Rev. Lett. **78**, 3665 (1997).

[27] C. I. Hancox, S. C. Doret, M. T. Hummon, L. J. Luo, and J. M. Doyle, Nature **431**, 281 (2004).

[28] C. C. Bradley, C. A. Sackett, J. J. Tollett, , and R. G. Hulet, Phys. Rev. Lett. **75**, 1687 (1995).

[29] K. B. Davis, M. O. Mewes, M. R. Andrews, N. J. Druten, D. S. Durfee, D. M. Kurn, and K. W., Phys. Rev. Lett. **75**, 3969 (1995).

[30] P. D. Lett, K. Helmerson, W. D. Philips, L. P. Ratliff, S. L. Rolston, and M. E. Wagshul, Phys. Rev. Lett. **71**, 2200 (1993).

[31] J. D. Miller, R. A. Cline, and D. J. Heinzen, Phys. Rev. Lett. **71**, 2204 (1993).

[32] E. R. I. Abraham, N. W. M. Ritchie, W. I. McAlexander, and R. G. Hulet, J. Chem. Phys. **103**, 7773 (1995).

[33] H. Wang, P. L. Gould, and W. C. Stwalley, Phys. Rev. A **53**, R1216 (1996).

[34] A. Fioretti, D. Comparat, A. Crubellier, O. Dulieu, F. Masnou-Seeuws, and P. Pillet, Phys. Rev. Lett. **80**, 4402 (1998).

[35] H. R. Thorsheim, J. Weiner, and P. S. Julienne, Phys. Rev. Lett. **58**, 2420 (1987).

[36] J. D. Miller, R. A. Cline, and D. J. Heinzen, Phys. Rev. Lett. **71**, 2204 (1993).

[37] C. Haimberger, J. Kleinert, M. Bhattacharya, and N. P. Bigelow, Phys. Rev. A **70**, 021402(R) (2004).

[38] A. J. Kerman, J. M. Sage, S. Sainis, T. Bergeman, and D. DeMille, Phys. Rev. Lett. **92**, 153001 (2004).

[39] A. J. Kerman, J. M. Sage, S. Sainis, T. Bergeman, and D. DeMille, Phys. Rev. Lett. **92**, 033004 (2004).

[40] M. W. Mancini, G. D. Telles, A. R. L. Caires, V. S. Bagnato, and L. G. Marcassa, Phys. Rev. Lett. **92**, 133203 (2004).

[41] D. Wang, J. Qi, M. F. Stone, O. Nikolayeva, H. Wang, B. Hattaway, S. D. Gensemer, P. L. Gould, E. E. Eyler, and W. Stwalley, Phys. Rev. Lett. **93**, 243005 (2004).

[42] S. D. Kraft, P. Staanum, J. Lange, L. Vogel, R. Wester, and M. Weidem, J. Phys. B **39**, S993 (2006).

[43] J. M. Sage, S. Sainis, T. Bergeman, and D. DeMille, . Phys. Rev. Lett. **94**, 203001 (2005).

[44] D. Jin and J. Ye, Physics Today **64**, 27 (2011).

[45] S. Y. T. Meerakker, H. L. Bethlem, and G. Meijer, Nature Phys. **4**, 595 (2008).

[46] H. L. Bethlem, F. M. H. Crompvoets, R. T. Jongma, S. Y. T. van de, Meerakker, and G. Meijer, Phys. Rev. A **65**, (2002).

[47] H. L. Bethlem, J. van Veldhoven, M. Schnell, and G. Meijer, Phys. Rev. A **74**, (2006).

[48] F. M. H. Crompvoets, H. L. Bethlem, R. T. Jongma, and G. Meijer, Nature **411**, (2001).

[49] C. E. Heiner, H. L. Bethlem, and G. Meijer, Phys. Chem. Chem. Phys. **8**, (2006).

[50] C. E. Heiner, D. Carty, G. Meijer, and H. L. Bethlem, Nature Phys. **3**, (2007).

[51] N. F. Ramsay, *Molecular Beams* (Oxford University Press) (1990).

[52] J. R. Zacharias, Phys. Rev. **94**, 751 (1954).

[53] B. Ghalfari, Phys. Rev. A. **60**, 3878 (1999).

[54] T. Rieger, P. Windpassinger, S. A. Rangwala, G. Rempe, and P. W. H. Pinkse, Phys. Rev. Lett. **99**, 063001 (2007).

[55] T. Rieger, T. Junglen, S. A. Rangwala, G. Rempe, P. W. H. Pinkse, and J. Bulthuis, Phys. Rev. Lett. **73**, 061402(R) (2006).

[56] M. Motsch, L. D. van Buuren, M. Sommer, C. Zeppenfeld, G. Rempe, and P. W. H. Pinkse, arxiv:physics 0809.1728v1 (2008).

[57] B. Benjamin and O. Andreas, Phys. Rev. A **82**, 033418 (2010).

[58] J. van Veldhoven, H. L. Bethlem, and G. Meijer, Phy. rev.Lett. **94**, 083001 (2005).

[59] T. Bergeman, G. Erez, and H. J. Metcalf, Phys. Rev. A **35 (4)**, 1535 (1987).

[60] V. S. Bagnato, G. P. Lafyatis, A. G. Martin, E. L. Raab, R. N. Ahmad-Bitar, and D. E. Pritchard, Phys. Rev. Lett. **58 (21)**, 2194 (1987).

[61] J. M. Brown, J. T. Hougen, K. P. Huber, J. W. C. Johns, I. Kopp, H. Lefebvre-Brion, A. J. Merer, D. A. Ramsay, J. Rostas, and R. N. Zare, J. Mol. Spectrosc. **55**, 500 (1975).

[62] F. H. Geuzebroek, M. G. Tenner, A. W. Kleyn, and S. Stolte, Chem. Phys. Lett. **187**, 520 (1991).

[63] G. Herzberg, 2nd ed. (van Nostrand Reinhold, New York) (1950).

[64] C. Amiot, J. P. Maillard, and J. Chauville, **87**, 196 (1981).

[65] B. J. Bischel, Ph.d thesis, The University of Oklahoma, 2005.

[66] J. S. Alexander, Master thesis, The University of Oklahoma, 2006.

[67] G. Reiser, W. Habenicht, K. M. Dethlefs, and E. W. Schlag, Chem. Phys. Lett. **152**, 119 (1988).

[68] J. H. VanVleck, Phys. Rev. **33**, 467 (1929).

[69] A. M. Wodtke, L. Huewel, H. Schlueter, H. Voges, G. Meijer, and P. Andresen, J. Chem. Phys. **89**, 1929 (1988).

[70] W. C. Campbell and J. M. Doyle, Cooling, trap loading, and beam production using a cryogenic helium buffer gas .

[71] R. D. Present, *Kinetic theory of gases* McGraw-Hills Block Company, lnc., New York, Toronto London (1958).

[72] H. F. Hess, G. P. Kochanski, J. M. Doyle, N. Masuhara, D. Kleppner, and T. J. Greytak, Phys. Rev. Lett. **59**, 672 (1987).

[73] J. J. Tollett, C. C. Bradley, C. A. Sackett, , and R. G. Hulet, Phys. Rev. A **51**, R22 (1995).

[74] J. M. Doyle *et al*, REVIEW OF SCIENTIFIC INSTRUMENTS **75**, 17 (2004).

[75] Proceedings of the Royal Society of London. Series A, Mathematical and Physical Sciences **408**, 233 (1986).

[76] F. Friedrich, R. deCarvalho, J. Kim, D. Patterson, J. D. Weinstein, and J. M. Doyle, J. Chem. Soc. Faraday Trans. **94**, 17831791 (1998).

[77] M. Zwierlein, C. Stan, C. Schunck, R. S. F., S. Gupta, Z. Hadzibabic, and W. Ketterle, Department of Physics, MITHarvard Center for Ultracold Atoms, and Research Laboratory of Electronics, MIT, Cambridge, Massachusetts 02139, USA .

[78] P. A. G. O'Hare, J. Chem. Phys. **52**, 2992 (1970).

[79] P. F. Edward, Permanent Magnet And Electromechanical Devices: Materials, Analysis, And Applications .

[80] R. Ravaud, G. Lemarquand, and C. Depollier, IEEE TRANSACTIONS ON MAGNETICS **44**, 1982 (2008).

[81] R. Ravaud, G. Lemarquand, and V. Lemarquand, Progress In Electromagnetics Research B **11**, 281297 (2009).

[82] S. I. Babic and C. Akyel, Progress In Electromagnetics Research C **5**, 71 (2008).

[83] C. Dedman, J. Nes, T. Hanna, and K. Dall, Review of Scientific Instruments **72**, 5136 (2004).

Appendix A

Permanent magnet Zeeman slower

There are many techniques to slow and cool atomic beams. Zeeman slowing is the best known and a very efficient and advantageous method of cooling. In this appendix, I will summarize the physics of the Zeeman slower, especially the permanent magnet Zeeman slower that I have designed. The magnetic field in a Zeeman slower is produced by series of ring permanent magnets. A magnetic field is applied to shift the energy levels of the atoms moving along the axis of the desired Zeeman slower tube. If there is an appropriate field along the axis, the atoms moving through the tube can be decelerated efficiently by a counter propagating laser beam of constant frequency. To calculate this desired field of the Zeeman slower for Rb atoms as shown in in Figure A.1(red), we used the relation given in [83] for Zeeman slower for 42 cm long. I wrote the Mathematica code to calculate the Zeeman slower profile for the series of ring permanent magnets as shown in in Figure A.1(blue). The advantage of this design is the absence of wires and currents. Also, the design uses flexible permanent magnets and the magnets can be attached and removed as necessary. I derived the expression for the magnetic field along the axis of an ideal permanent magnet of length h and radius R given by Eq. A.1.

$$B(z) = \frac{\mu M}{2}\left(\frac{z+\frac{h}{2}}{\sqrt{R^2+(z+\frac{h}{2})^2}} - \frac{z-\frac{h}{2}}{\sqrt{R^2+(z-\frac{h}{2})^2}}\right) \tag{A.1}$$

where M is magnetization and μ is the permeability of free space. For a ring magnet having outer radius R and inner radius r, the field produced along the z axis is given

by

$$B(z) = \frac{\mu M}{2}\left(\frac{z+\frac{h}{2}}{\sqrt{R^2+(z+\frac{h}{2})^2}} - \frac{z-\frac{h}{2}}{\sqrt{R^2+(z-\frac{h}{2})^2}}\right) - \frac{\mu M}{2}\left(\frac{z+\frac{h}{2}}{\sqrt{r^2+(z+\frac{h}{2})^2}} - \frac{z-\frac{h}{2}}{\sqrt{r^2+(z-\frac{h}{2})^2}}\right) \tag{A.2}$$

Our model placed 21 permanent ring magnets on the z-axis, from z = 0 to z = 42 cm. The outer radius was fixed to be 5 cm, the μM was fixed to be 2000 Gauss, and spacing between the magnets was fixed to be 2.1 cm. I calculated the internal radii of 21 ring magnets using the desired field equations. The internal radii are given in Table A.1. As the graph in Figure A.1 shows, this configuration produces magnetic fields in agreement with the magnetic field of the desired ideal slower.

The expected velocity curve if our desired field matches the expected field is $v0\sqrt{1-\frac{z}{z0}}$, where v0 is the initial velocity, z is the distance along the Zeeman slower, and z0 is the length of the Zeeman slower. For the initial acceleration of Rb atoms given in [83], the variety of initial velocities and the trajectory curves are shown in Fig-A.3 and Fig-A.2. It can be seen that those atoms with velocities greater than 30000 cm/sec are not slowed down by the Zeeman slower. The atoms with initial velocities less than 30000 cm/sec are slowed down to nearly 2300 cm/sec. The trajectories of the atomic particles are calculated using classical equations of motion. The initial radial position is set to zero. Fig-A.2 shows the trajectories of the particles in the axial direction as a function of time. The faster atoms are not slowed down by the Zeeman slower because the faster atoms are not captured by the slower. These molecules follow the unmodified trajectories through Zeeman slower without any reduction in velocity. Other atoms with velocities below the capture velocities are slowed down by the slower

Table A.1: Tabulation of the calculated inner radius of the ring magnets.

Inner radius (cm)	
r1	2.821
r2	3.185
r3	2.925
r4	2.851
r5	2.785
r6	2.771
r7	2.795
r8	2.857
r9	2.952
r10	3.076
r11	3.226
r12	3.398
r13	3.588
r14	3.790
r15	4.012
r16	4.212
r17	4.508
r18	4.542
r19	4.712
r20	4.570
r21	3.8223

within its length. Fig-A.3 shows the evolution of the radial position of the atoms through the Zeeman slower as a function of axial position of atoms. The zero point in the axial position is the entrance of the slower. The undeviating of the atom having initial velocity greater than the capture velocity is a result of the non-resonance of the laser with the atomic energy shift. For the atoms below the capture velocity of the slower, there are straight trajectories until the point where they are in resonance with the slowing laser beam. The atoms remain in resonance with the laser beam and are continually slowed down until their velocity become minimum. Velocities are slowed down and the large spreads in velocities below captured velocity are compressedd in

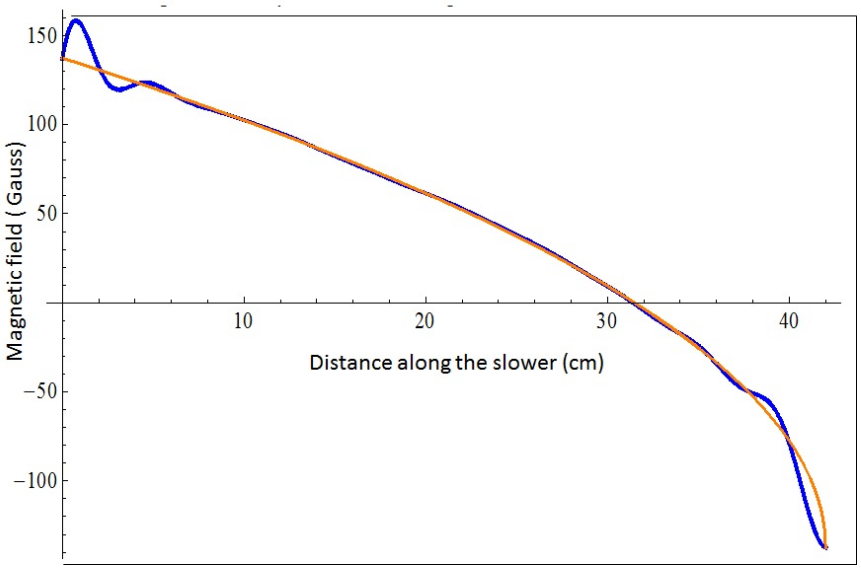

Figure A.1: Plot of desired magnetic field (red) and simulated magnetic field (blue) for 42 cm long Zeeman slower

velocity space. We can see in the plot of Fig-A.3 that the different axial velocities are compressed to the same point.

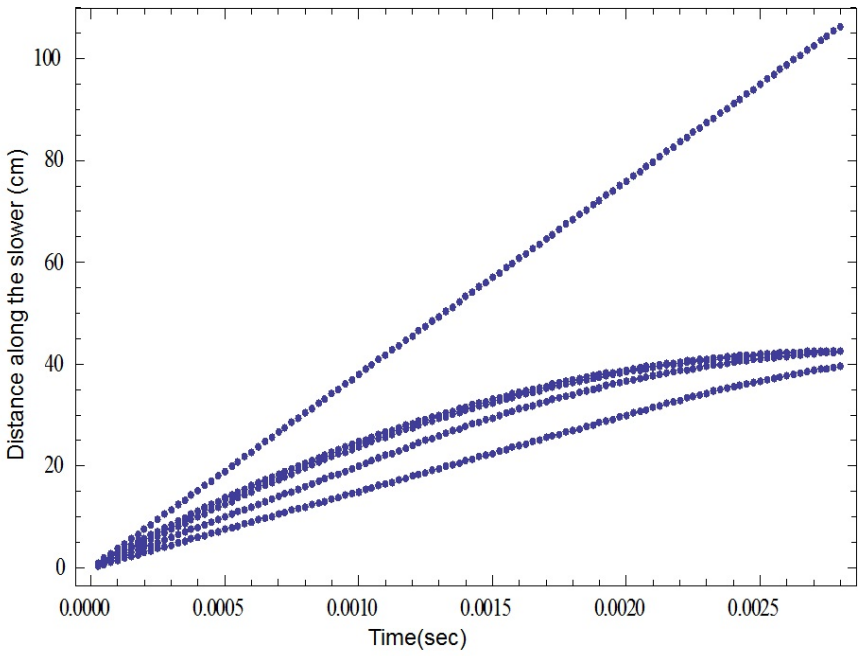

Figure A.2: simulated trajectory of the Rb atoms through the Zeeman slower as a function of time

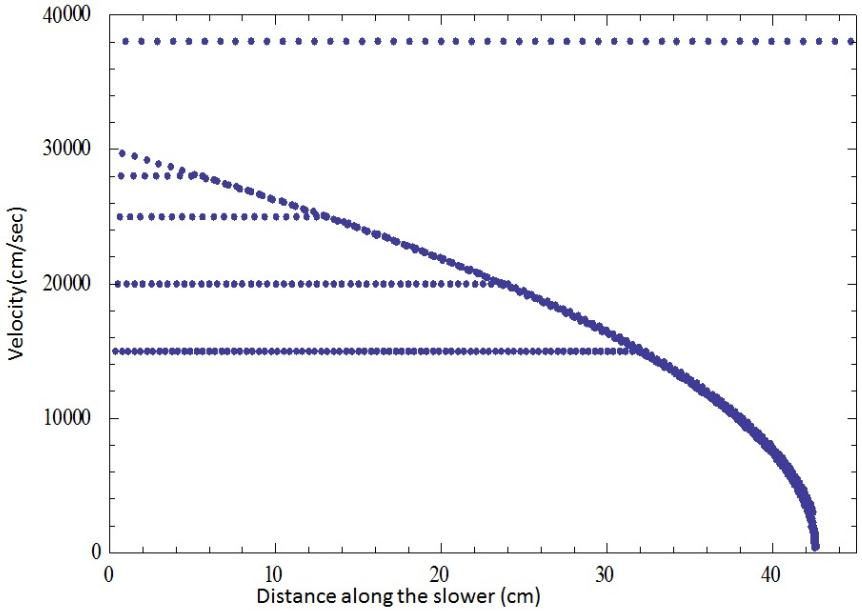

Figure A.3: Simulated trajectories for Rb atoms travelling through the Zeeman slower for a variety of velocities is shown. Trajectories show the slowing of the axial velocities.

Appendix B

Mathematica code to calculate trap depth between two rings permanent magnets using analytical expressions

```
R = 0.05; (* Outer radius of ring magnet in m *)
a = 0.018; (* Inner radius of ring magnet in m *)
M = 1.48; (* Magnetization *)
μ0 = 4 * Pi * 10^-7; (* permeability of free space *)

r[x_, y_] := Sqrt[x^2 + y^2];

k1p[x_, y_, z_, h_] := 2 * Sqrt[a * r[x, y]] / Sqrt[(a + r[x, y])^2 + (z - h)^2];

k2p[x_, y_, z_, h_] := 2 * Sqrt[R * r[x, y]] / Sqrt[(R + r[x, y])^2 + (z - h)^2];

h1p[x_, y_, z_, h_] := 2 * r[x, y] / (r[x, y] + Sqrt[r[x, y]^2 + (z - h)^2]);

h2p[x_, y_, z_, h_] := 2 * r[x, y] / (r[x, y] - Sqrt[r[x, y]^2 + (z - h)^2]);

θ11p[x_, y_, z_, h_] := ArcSin[Sqrt[(1 - h1p[x, y, z, h]) / (1 - k1p[x, y, z, h]^2)]];

θ12p[x_, y_, z_, h_] := ArcSin[Sqrt[(1 - h1p[x, y, z, h]) / (1 - k2p[x, y, z, h]^2)]];

θ21p[x_, y_, z_, h_] := ArcSin[Abs[z - h] / (Sqrt[r[x, y]^2 + (z - h)^2] + r[x, y])];

θ22p[x_, y_, z_, h_] := ArcSin[Abs[z - h] / (Sqrt[r[x, y]^2 + (z - h)^2] + r[x, y])];
```

```
Brp[x_, y_, z_, h_] :=
  M/(Pi*μ0) * 1/k1p[x, y, z, h] * Sqrt[a/r[x, y]] * (EllipticE[k1p[x, y, z, h]^2] -
    (1 - k1p[x, y, z, h]^2/2) * EllipticK[k1p[x, y, z, h]^2]) -
  M/(Pi*μ0) * 1/k2p[x, y, z, h] * Sqrt[R/r[x, y]] * (EllipticE[k2p[x, y, z, h]^2] -
    (1 - k2p[x, y, z, h]^2/2) * EllipticK[k2p[x, y, z, h]^2]);
Bzp[x_, y_, z_, h_] := M/(2*3.14*μ0) *
  (k1p[x, y, z, h] * (z - h) * Sqrt[r[x, y]^2 + (z - h)^2]/
     (Sqrt[r[x, y]*a] * (Sqrt[r[x, y]^2 + (z - h)^2] + r[x, y])) * EllipticK[k1p[x, y, z, h]] +
   Pi/2 * Sign[z - h] * Sign[Sqrt[r[x, y]^2 + (z - h)^2] - a] *
    (1 - (EllipticF[θ11p[x, y, z, h], 1 - k1p[x, y, z, h]]/
        EllipticK[1 - k1p[x, y, z, h]] + 2/Pi * EllipticK[
         k1p[x, y, z, h]] * JacobiZeta[θ11p[x, y, z, h], 1 - k1p[x, y, z, h]])) +
   Pi/2 * Sign[z - h] * (1 - (EllipticF[θ21p[x, y, z, h], 1 - k1p[x, y, z, h]]/
        EllipticK[1 - k1p[x, y, z, h]] +
       2/Pi * EllipticK[k1p[x, y, z, h]] *
```

```
JacobiZeta[θ21p[x, y, z, h], 1 - k1p[x, y, z, h]]))) - M/(2 * 3.14 * μ0) *
(k2p[x, y, z, h] * (z - h) * Sqrt[r[x, y]^2 + (z - h)^2] /
 (Sqrt[r[x, y] * R] * (Sqrt[r[x, y]^2 + (z - h)^2] + r[x, y])) * EllipticK[k2p[x, y, z, h]] +
 Pi/2 * Sign[z - h] * Sign[Sqrt[r[x, y]^2 + (z - h)^2] - R] *
  (1 - (EllipticF[θ12p[x, y, z, h], 1 - k2p[x, y, z, h]] /
      EllipticK[1 - k2p[x, y, z, h]] + 2/Pi * EllipticK[
       k2p[x, y, z, h]] * JacobiZeta[θ12p[x, y, z, h], 1 - k2p[x, y, z, h]])) +
 Pi/2 * Sign[z - h] * (1 - (EllipticF[θ22p[x, y, z, h], 1 - k2p[x, y, z, h]] /
      EllipticK[1 - k2p[x, y, z, h]] +
     2/Pi * EllipticK[k2p[x, y, z, h]] *
      JacobiZeta[θ22p[x, y, z, h], 1 - k2p[x, y, z, h]])));
Bz[x_, y_, z_, h_] := Bzp[x, y, z, h] + Bzp[x, y, z, -h];
Bp[x_, y_, z_, h_] := Brp[x, y, z, h] + Brp[x, y, z, -h];
B[x_, y_, z_, h_] := Sqrt[Bz[x, y, z, h]^2 + Bp[x, y, z, h]^2];
a1 =
 ListPlot[Table[{x, 10000 * μ0 * B[x, 0, 0, 0.00375]}, {x, -0.015, 0.015, 0.000005}],
  Joined → True, PlotRange → {0, 5000}, Frame → True,
  PlotRange → All, FrameLabel → {"x (m)", "Magnetic Field(Gauss)"},
  PlotLabel → "Magnetic Field along x direction"]
```

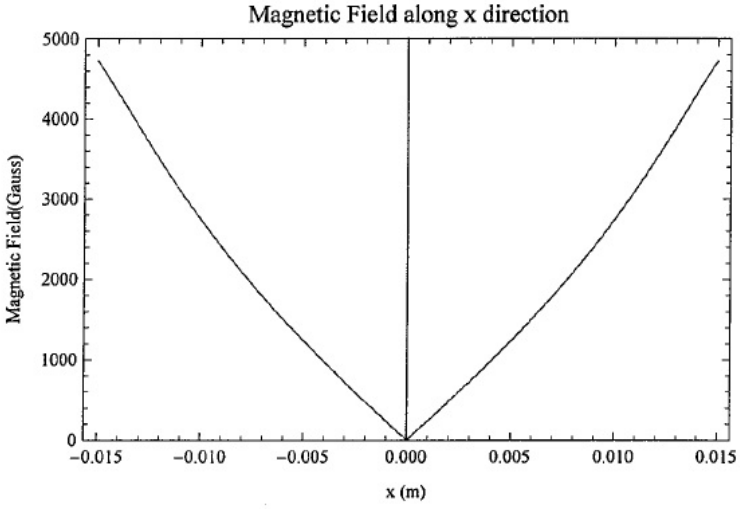


```
b1 =
 ListPlot[Table[{y, 10 000 * μ0 * B[0, y, 0, 0.00375]}, {y, -0.015, 0.015, 0.000005}],
  Joined → True, PlotRange → {0, 5000}, Frame → True,
  PlotRange → All, FrameLabel → {"y (m)", "Magnetic Field(Gauss)"},
  PlotLabel → "Magnetic Field along y direction"]
```

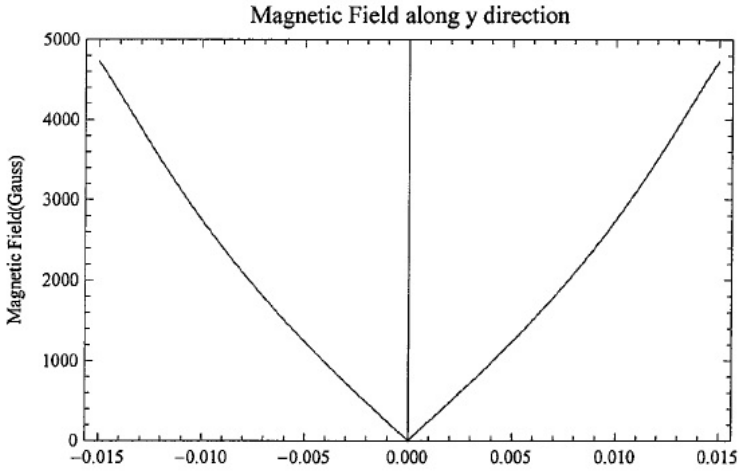


```
c1 = ListPlot[Table[{z, 10 000 * μ0 * B[0.000001, 0.000001, z, 0.00375]},
    {z, -0.015, 0.015, 0.000005}], Joined → True, PlotRange → All, Frame → True,
  PlotRange → All, FrameLabel → {"z (m)", "Magnetic Field(Gauss)"},
  PlotLabel → "Magnetic Field along z direction"]
```

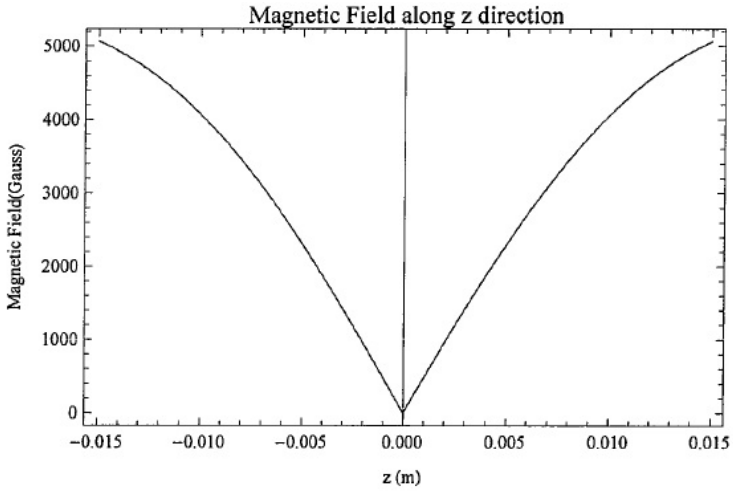


```
d1 = ListPlot[Table[{√2 * x, 10 000 * μ0 * B[x, x, 0, 0.00375]},
    {x, -0.015, 0.015, 0.000005}], Joined → True, PlotRange → {0, 5000}, Frame → True,
  PlotRange → All, FrameLabel → {"x=y (m)", "Magnetic Field(Gauss)"},
  PlotLabel → "Magnetic Field along x=y direction"]
```

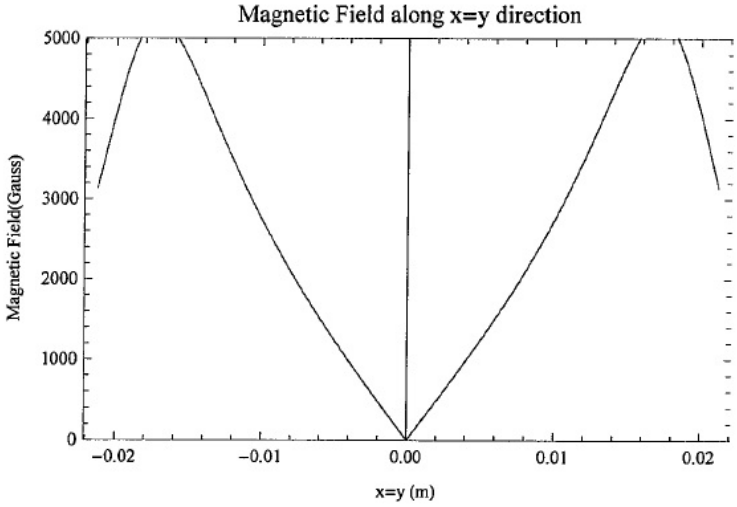


```
e1 = ListPlot[Table[{√2 * x, 10 000 * μ0 * B[x, 0, x, 0.00375]},
    {x, -0.015, 0.015, 0.000005}], Joined → True, PlotRange → {0, 5000}, Frame → True,
  PlotRange → All, FrameLabel → {"x=z (m)", "Magnetic Field(Gauss)"},
  PlotLabel → "Magnetic Field along x=z direction"]
```

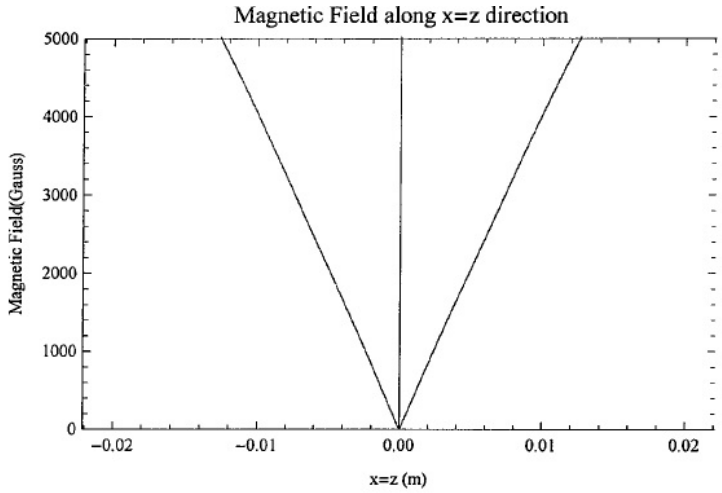


```
f1 = ListPlot[Table[{√2 * y, 10 000 * μ0 * B[0, y, y, 0.00375]},
    {y, -0.015, 0.015, 0.000005}], Joined → True, PlotRange → {0, 5000}, Frame → True,
  PlotRange → All, FrameLabel → {"y=z (m)", "Magnetic Field(Gauss)"},
  PlotLabel → "Magnetic Field along y=z direction"]
```

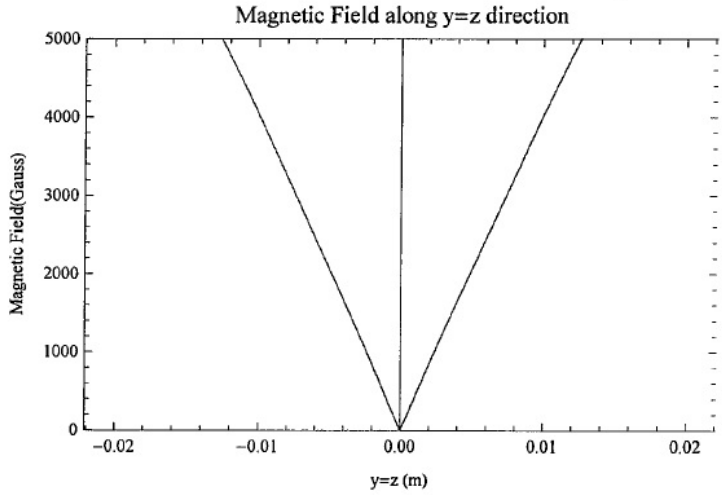


```
Show[a1, b1, c1, d1, e1, f1]
```

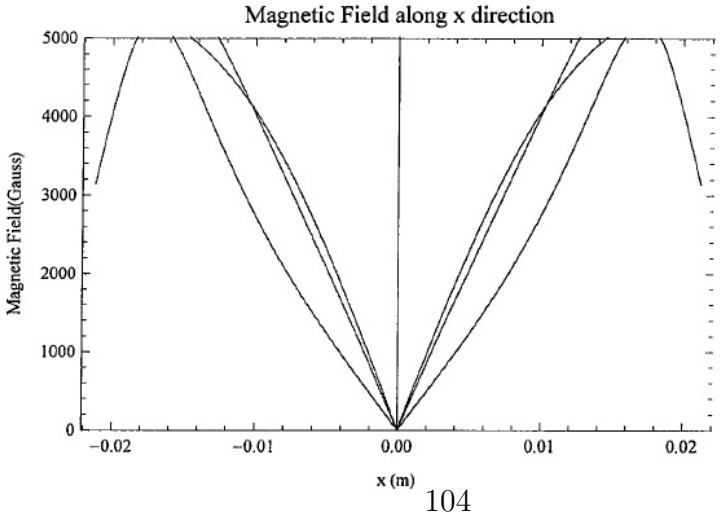

Appendix C

Magnetic trap depth calculation mathematica code due to bar magnets

```
a = 0.0222; (* dimension of the magnetic surface = a*a , perfect square*)
```

Integration of following 3 functions produces a magnetic field due to a magnetic surface perpendicular to z-axis and the center is also on the z-axis.

$$\texttt{FxZ[x\_, y\_, z\_, xp\_, yp\_, zk\_, M\_]} := M\,\frac{x - xp}{12.571\left((x-xp)^2 + (y-yp)^2 + (z-zk)^2\right)^{3/2}};$$

$$\texttt{FyZ[x\_, y\_, z\_, xp\_, yp\_, zk\_, M\_]} := M\,\frac{y - yp}{12.571\left((x-xp)^2 + (y-yp)^2 + (z-zk)^2\right)^{3/2}};$$

$$\texttt{FzZ[x\_, y\_, z\_, xp\_, yp\_, zk\_, M\_]} := M\,\frac{z - zk}{12.571\left((x-xp)^2 + (y-yp)^2 + (z-zk)^2\right)^{3/2}};$$

```
(* M is the magnetization*)
```

Integration of following 3 functions produces a magnetic field due to a magnetic surface perpendicular to x-axis and the center is also on the x-axis.

$$\texttt{FxX[x\_, y\_, z\_, xk\_, yp\_, zp\_, M\_]} := M\,\frac{z - zp}{12.571\left((z-zp)^2 + (y-yp)^2 + (x-xk)^2\right)^{3/2}};$$

$$\texttt{FyX[x\_, y\_, z\_, xk\_, yp\_, zp\_, M\_]} := M\,\frac{y - yp}{12.571\left((z-zp)^2 + (y-yp)^2 + (x-xk)^2\right)^{3/2}};$$

$$\texttt{FzX[x\_, y\_, z\_, xk\_, yp\_, zp\_, M\_]} := M\,\frac{x - xk}{12.571\left((z-zp)^2 + (y-yp)^2 + (x-xk)^2\right)^{3/2}};$$

Integration of following 3 functions produces a magnetic field due to a magnetic surface perpendicular to y-axis and the center is also on the y-axis.

$$\texttt{FxY[x\_, y\_, z\_, xp\_, yk\_, zp\_, M\_]} := M\,\frac{x - xp}{12.571\left((x-xp)^2 + (z-zp)^2 + (y-yk)^2\right)^{3/2}};$$

Integration of following 3 functions produces a magnetic field due to a magnetic surface perpendicular to y-axis and the center is also on the y-axis.

$$\texttt{FxY[x\_, y\_, z\_, xp\_, yk\_, zp\_, M\_]} := M\,\frac{x - xp}{12.571\left((x-xp)^2 + (z-zp)^2 + (y-yk)^2\right)^{3/2}};$$

$$\texttt{FyY[x\_, y\_, z\_, xp\_, yk\_, zp\_, M\_]} := M\,\frac{z - zp}{12.571\left((x-xp)^2 + (z-zp)^2 + (y-yk)^2\right)^{3/2}};$$

$$\texttt{FzY[x\_, y\_, z\_, xp\_, yk\_, zp\_, M\_]} := M\,\frac{y - yk}{12.571\left((x-xp)^2 + (z-zp)^2 + (y-yk)^2\right)^{3/2}};$$

Following function produces a magnetic field anywhere in space due to a magnetic surface located on (xk, yk, zk). The center of the magnetic surface must be located on x, y or z axis.
M=+1 or -1 defines whether this surface has a north or a south pole.

```
B[x_, y_, z_, xk_, yk_, zk_, M_] :=
  Module[{}, sumxZ = 0.; sumyZ = 0.; sumzZ = 0.; sumxX = 0.; sumyX = 0.;
   sumzX = 0.; sumxY = 0.; sumyY = 0.; sumzY = 0.; δ1 = .01 a; δ2 = .01 a;

   For[p1 = -a / 2., p1 ≤ a / 2., p1 += δ1,
    For[p2 = -a / 2., p2 ≤ a / 2., p2 += δ2,
     If[(xk == 0) && (yk == 0),
      sumxZ += FxZ[x, y, z, p1, p2, zk, M] δ1 δ2;
      sumyZ += FyZ[x, y, z, p1, p2, zk, M] δ1 δ2;
      sumzZ += FzZ[x, y, z, p1, p2, zk, M] δ1 δ2];
     If[(yk == 0) && (zk == 0),
      sumxX += FxX[x, y, z, xk, p1, p2, M] δ1 δ2;
      sumyX += FyX[x, y, z, xk, p1, p2, M] δ1 δ2;
      sumzX += FzX[x, y, z, xk, p1, p2, M] δ1 δ2];
     If[(xk == 0) && (zk == 0),
      sumxY += FxY[x, y, z, p1, yk, p2, M] δ1 δ2;
      sumyY += FyY[x, y, z, p1, yk, p2, M] δ1 δ2;
      sumzY += FzY[x, y, z, p1, yk, p2, M] δ1 δ2];
]];
Return[{sumxZ + sumxX + sumxY, sumyZ + sumyX + sumyY, sumzZ + sumzX + sumzY}]];
```

Following function produces the total magnetic field due to many magnetic surfaces described above.

```
Btot[x_, y_, z_] := B[x, y, z, 0.02225, 0, 0, 1] + B[x, y, z, -0.02225, 0, 0, 1] +
   B[x, y, z, 0, 0.02225, 0, 1] + B[x, y, z, 0, -0.02225, 0, 1] +
   B[x, y, z, 0, 0, 0.02225, 1] + B[x, y, z, 0, 0, -0.02225, 1];

Mag2Btot[x_, y_, z_] := Module[{}, Bval = Btot[x, y, z];
   B2 = Bval[[1]]^2 + Bval[[2]]^2 + Bval[[3]]^2;
   Return[Sqrt[B2]]];


xlst = {};
ylst = {};
zlst = {};
       For[i = -0.02, i ≤ 0.02, i += .01,
         AppendTo[xlst, {i, Mag2Btot[i, 0, 0]}];
         AppendTo[ylst, {i, Mag2Btot[0, i, 0]}];
         AppendTo[zlst, {i, Mag2Btot[0, 0, i]}];
        ];

       ListPlot[xlst, Joined → True, Frame → True,
        PlotLabel → "Mag. field along the x-axis",
        FrameLabel → {"x (m)", "Mag.field (T)"}]

       ListPlot[ylst, Joined → True, Frame → True,
        PlotLabel → "Mag. field along the y-axis",
        FrameLabel → {"y (m)", "Mag.field (T)"}]

       ListPlot[zlst, Joined → True, Frame → True,
        PlotLabel → "Mag. field along the z-axis",
        FrameLabel → {"z (m)", "Mag.field (T)"}]
```

Appendix D

Mathematica code to calculate magnetic trap depth for a pair of anti-Helmholtz coils

```
R = 0.1;(*Radius of each coil, in m *)
d = 0.062673;(* Distance between two coils,  in m *)
μ = 4 * π * 10^-7;(* Permeability of Free Space, in V.s/A.m *)
II = 100;(*Current through each coil,  in A *)
N0 = 20; (* Number of turns *)
I1 = N0 * II;

k1[R_, ρ_, z_, d_] := Sqrt[4 * R * ρ / ((R + ρ)^2 + (z - d)^2)];

k2[R_, ρ_, z_, d_] := Sqrt[4 * R * ρ / ((R + ρ)^2 + (z + d)^2)];

Bz1[R_, ρ_, z_, d_] := μ * I1 / (2 * π) * 1 / Sqrt[(R + ρ)^2 + (z - d)^2] * (EllipticK[k1[R, ρ, z, d]^2] +
    (R^2 - ρ^2 - (z - d)^2) / ((R - ρ)^2 + (z - d)^2) * EllipticE[k1[R, ρ, z, d]^2]);(* in V.s/m^2 = Tesla *)

Bz2[R_, ρ_, z_, d_] := μ * I1 / (2 * π) * 1 / Sqrt[(R + ρ)^2 + (z + d)^2] * (EllipticK[k2[R, ρ, z, d]^2] +
    (R^2 - ρ^2 - (z + d)^2) / ((R - ρ)^2 + (z + d)^2) * EllipticE[k2[R, ρ, z, d]^2]);(* in V.s/m^2 = Tesla *)

Bρ1[R_, ρ_, z_, d_] := μ * I1 / (2 * π * ρ) * (z - d) / Sqrt[(R + ρ)^2 + (z - d)^2] * (-EllipticK[k1[R, ρ, z, d]^2] +
    (R^2 + ρ^2 + (z - d)^2) / ((R - ρ)^2 + (z - d)^2) * EllipticE[k1[R, ρ, z, d]^2]);(* in V.s/m^2 = Tesla *)

Bρ2[R_, ρ_, z_, d_] := μ * I1 / (2 * π * ρ) * (z + d) / Sqrt[(R + ρ)^2 + (z + d)^2] * (-EllipticK[k2[R, ρ, z, d]^2] +
    (R^2 + ρ^2 + (z + d)^2) / ((R - ρ)^2 + (z + d)^2) * EllipticE[k2[R, ρ, z, d]^2]);(* in V.s/m^2 = Tesla *)

Bz[R_, ρ_, z_, d_] := Bz1[R, ρ, z, d] - Bz2[R, ρ, z, d];(* in V.s/m^2 = Tesla *)

Bρ[R_, ρ_, z_, d_] := Bρ2[R, ρ, z, +d] - Bρ1[R, ρ, z, d];(* in V.s/m^2 = Tesla *)
```

```
B[R_, ρ_, z_, d_] := √(Bz[R, ρ, z, d]^2 + Bρ[R, ρ, z, d]^2) ;(* in V.s/m^2 = Tesla *)

ListPlot[Table[{ρ, 10000 * B[R, ρ, 0, d]}, {ρ, -0.1, 0.1, 0.0001}], PlotRange → All,
 Frame → True, Joined → True, FrameLabel → {"ρ (m)", "Magnetic Field (Gauss)"}]
```

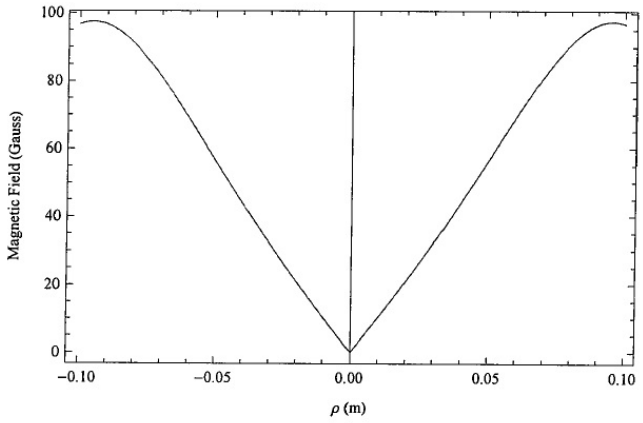


```
ListPlot[Table[{z, 10000 * B[R, 0.000001, z, d]}, {z, -0.08, 0.08, 0.0001}],
 PlotRange → All, Frame → True, Joined → True,
 FrameLabel → {"z (m)", "Magnetic Field (Gauss)"}]
```

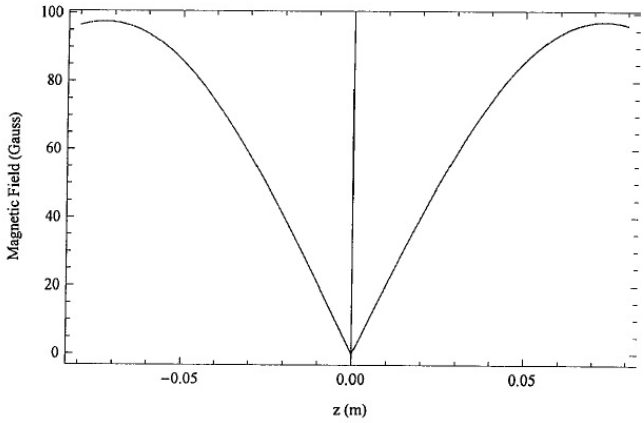

Appendix E

Calculated trap depths of two ring magnets

Along x Gauss	Along y Gauss	Along z Gauss	Along x=y Gauss	Along y=z Gauss	Along x=z Gauss	Inner Radius cm	Tip to tip spacing cm	Outer Radius cm	μM Gauss
2923.61	2923.61	2573.27	2923.8	3379.6	3379.6	1.75	0.75	3	13000
3012	3012	3261.49	3012.26	4252.59	4252.59	1.5	0.75	3	13000
2939.08	2939.08	4036.37	3087.93	5210.88	5210.88	1.25	0.75	3	13000
2682.71	2682.71	4919.34	3273.7	6269.99	6269.99	1	0.75	3	13000
2000.18	2000.18	5942.34	2000.12	7459.18	7459.18	0.75	0.75	3	13000
4009.74	4009.74	3887.87	4009.68	4930.65	4930.65	1.75	0.75	4	13000
3871.32	3871.32	4512.85	3871.52	5475.05	5475.05	1.5	0.75	4	13000
3608.11	3608.11	5267.71	3608.32	6486.04	6486.04	1.25	0.75	4	13000
3187.8	3187.8	6083.31	3188.07	7449.62	7449.62	1	0.75	4	13000
2558.21	2558.21	7014.87	2558.44	8441.83	8441.83	0.75	0.75	4	13000
1500.92	1500.92	8109.11	1500.92	9594.02	9594.02	0.5	0.75	4	13000
2655.84	2655.84	8461.14	3077.5	9855.88	9855.88	0.5	0.75	4.5	13000
2683.07	2683.07	7419.46	2683.05	8794.55	8794.55	0.75	0.75	4.5	13000
3359.35	3359.35	6528.14	3359.57	7875.79	7875.79	1	0.75	4.5	13000
3831.49	3831.49	5746.14	3831.41	7043.41	7043.41	1.25	0.75	4.5	13000
4152.54	4152.54	5049.21	4152.97	6275.41	6275.41	1.5	0.75	4.5	13000
4287.47	4287.47	4664.9	4287.38	5821.07	5821.07	1.65	0.75	4.5	13000
4323.93	4323.93	4541.81	4324.18	5667.29	5667.29	1.7	0.75	4.5	13000
4356.38	4356.38	4420.6	4356.34	5513.03	5513.03	1.75	0.75	4.5	13000
4373.98	4373.98	4348.48	4373.75	5420.39	5420.39	1.78	0.75	4.5	13000
4384.95	4384.95	4300.66	4385.18	5358.66	5358.66	1.8	0.75	4.5	13000
4395.31	4395.31	4253.06	4395.47	5296.97	5296.97	1.82	0.75	4.5	13000
4430.86	4430.86	4064.89	4431.12	5051.12	5051.12	1.9	0.75	4.5	13000
4448.39	4448.39	3949.19	4448.57	4898.61	4898.61	1.95	0.75	4.5	13000
4462.41	4462.41	4462.75	4462.75	4747.35	4747.35	2.	0.75	4.5	13000
4249.97	4249.97	3288.07	4482.73	4018.09	4018.09	2.25	0.75	4.5	13000
3430.31	3430.31	2782.48	4045.8	3347.67	3347.67	2.5	0.75	4.5	13000
4435.53	4435.53	3519.06	4690.12	4261.78	4261.78	2.25	0.75	4.75	13000

4653.12	4653.12	3953.38	4653.03	4839.7	4839.7	2.05	0.75	4.75	13000
4554.82	4554.82	3625.18	4685.87	4403.03	4403.03	2.2	0.75	4.75	13000
4635.98	4635.98	4066	4636.23	4988.96	4988.96	2	0.75	4.75	13000
4636.01	4636.01	3732.94	4677.74	4546.54	4546.54	2.15	0.75	4.75	13000
4665.84	4665.84	3842.35	4667.3	4692.15	4692.15	2.1	0.75	4.75	13000
4591.86	4591.86	4295.89	4592.15	5291.68	5291.68	1.9	0.75	4.75	13000
4546.75	4546.75	4484.06	4546.67	5536.6	5536.6	1.82	0.75	4.75	13000
4534.06	4534.06	4531.66	4534.43	5598.04	5598.04	1.80	0.75	4.75	13000
4520.79	4520.79	4579.48	4521.11	5659.52	5659.52	1.78	0.75	4.75	13000
4499.78	4499.78	4651.6	4500	5751.76	5751.76	1.75	0.75	4.75	13000
4269.96	4269.96	5273.52	4270.22	6510.45	6510.45	1.5	0.75	4.75	13000
3925.36	3925.36	5958.39	3925.63	7256.22	7256.22	1.25	0.75	4.75	13000
3432.09	3432.09	6725.4	3432.09	8060.6	8060.6	1	0.75	4.75	13000
2736.18	2736.18	7597.91	2736.41	8947.04	8947.04	0.75	0.75	4.75	13000
2470.28	2470.28	8615.44	2863.98	9969.18	9969.18	0.5	0.75	4.75	13000
4572.01	4572.01	4664.06	4627.96	5340.05	5340.05	1.75	0.75	5	13000
4374.84	4374.84	5360.09	4374.51	6284.68	6284.68	1.5	0.75	5	13000
4009.15	4009.15	6114.94	4009.63	7281.55	7281.55	1.25	0.75	5	13000
3497.16	3497.16	6908.12	3497.33	8222.4	8222.4	1	0.75	5	13000
2783.85	2783.85	7762.83	2784.42	9086.77	9086.77	0.75	0.75	5	13000
4572.01	4572.01	4664.06	4627.96	5340.05	5340.05	1.75	0.75	5	13000
4374.84	4374.84	5360.09	4374.51	6284.68	6284.68	1.5	0.75	5	13000
4009.15	4009.15	6114.94	4009.63	7281.55	7281.55	1.25	0.75	5	13000
3497.16	3497.16	6908.12	3497.33	8222.4	8222.4	1	0.75	5	13000
2783.85	2783.85	7762.83	2784.42	9086.77	9086.77	0.75	0.75	5	13000
4980.77	4980.77	6241.67	4980.4	7632.65	7632.65	1.5	0.75	5	14800
5220.01	5220.01	5676.04	5219.71	6918.06	6918.06	1.7	0.75	5	14800
5268.66	5268.66	5538.05	5268.94	6737.83	6737.83	1.75	0.75	5	14800
5313.17	5313.17	5401.5	5312.93	6557.95	6557.95	1.8	0.75	5	14800
5353.7	5353.7	5266.49	5354.05	6378.85	6378.85	1.85	0.75	5	14800
5390.37	5390.37	5133.09	5390.22	6200.94	6200.94	1.9	0.75	5	14800
5423.3	5423.3	5001.36	5423.75	6024.59	6024.59	1.95	0.75	5	14800
5452.59	5452.59	4871.37	5452.56	5850.14	5850.14	2	0.75	5	14800
5498.11	5498.11	4616.75	5500.76	5508.01	5508.01	2.1	0.75	5	14800
5535.84	5535.84	4432.11	5535.61	5340.89	5340.89	2.2	0.75	5	14800
5091.65	5091.65	3753.08	5563.42	4678.34	4678.34	2.5	0.75	5	14800

Appendix F

Energy adjusting integration algorithm

$Tiot = \frac{1}{2} m\, vo^2 + U(xo, yo, zo)$ is the initial total energy of the particle. It should be a constant in time at each point of the trajectory. After time Δt, the new position can be written as

$$xn = xo + vox\,\Delta t + \frac{1}{2} ax(xo, yo, zo)\,\Delta t^2$$

$$yn = yo + voy\,\Delta t + \frac{1}{2} ay(xo, yo, zo)\,\Delta t^2$$

$$zn = zo + voz\,\Delta t + \frac{1}{2} az(xo, yo, zo)\,\Delta t^2$$

Where $ax(xo, yo, zo)$ is the initial acceleration, xo, yo, zo are the initial positions of the particle, vox, voy, voz are the initial velocities. At each point of the trajectory, the kinetic energy should be positive and the potential energy at new position (xn, yn, zn) is calculated. Then the correct new position can be obtained as follows.

$If\,(Tiot - U(xn, yn, zn) < 0\,)$

$\{\, xn = xn - vox\,\Delta t$

$yn = yn - voy\,\Delta t$

$zn = zn - voz\,\Delta t\,\}$

Then new corrected velocities can be written as,

$$vnx = vox + ax(xo, yo, zo)\,\Delta t$$

$$vny = voy + ay(xo, yo, zo)\,\Delta t$$

$$vnz = voz + az(xo, yo, zo)\,\Delta t$$

The quantities $\sqrt{\frac{2(Tiot - U(xn, yn, zn))}{m}}$ and $\sqrt{vnx^2 + vny^2 + vnz^2}$ are not exactly the same at each point of the trajectory, we need to adjust the velocities.

$$vadj = \sqrt{\frac{2(Tiot - U(xn, yn, zn)}{m\,(vnx^2 + vny^2 + vnz)}}$$

$$vnv = vadj\ vnx$$

$$vny = vadj\ vny$$

$$vnz = vadj\ vnz$$

This algorithm can be used for nearly harmonic trajectories.

Appendix G

Machine drawing of the magnetic trap with detector

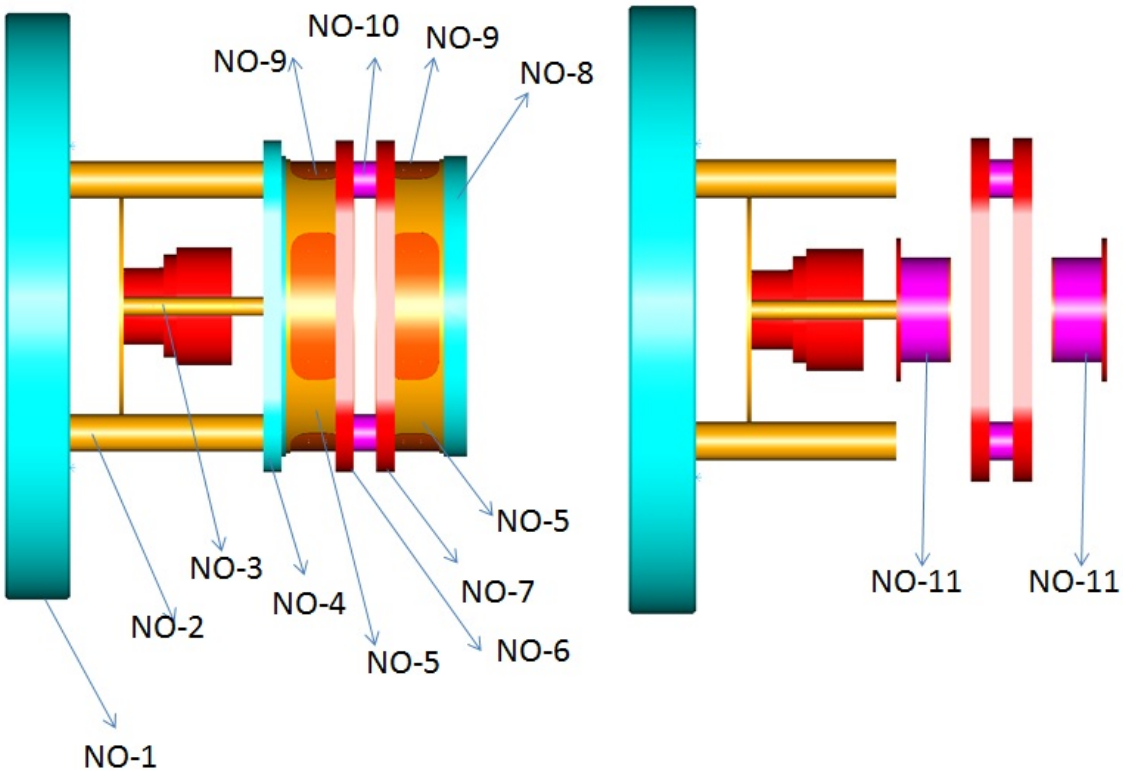

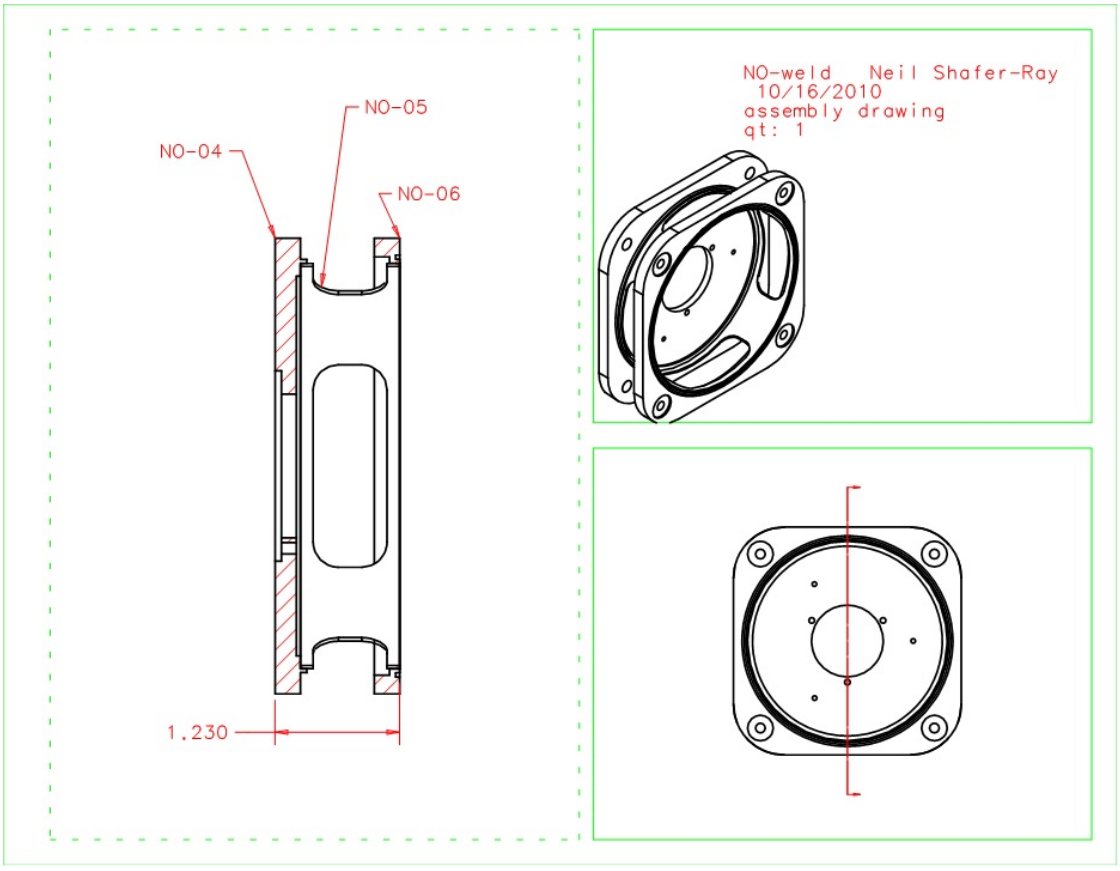
NO-05
NO-04
NO-06
1.230
NO-weld Neil Shafer-Ray
10/16/2010
assembly drawing
qt: 1

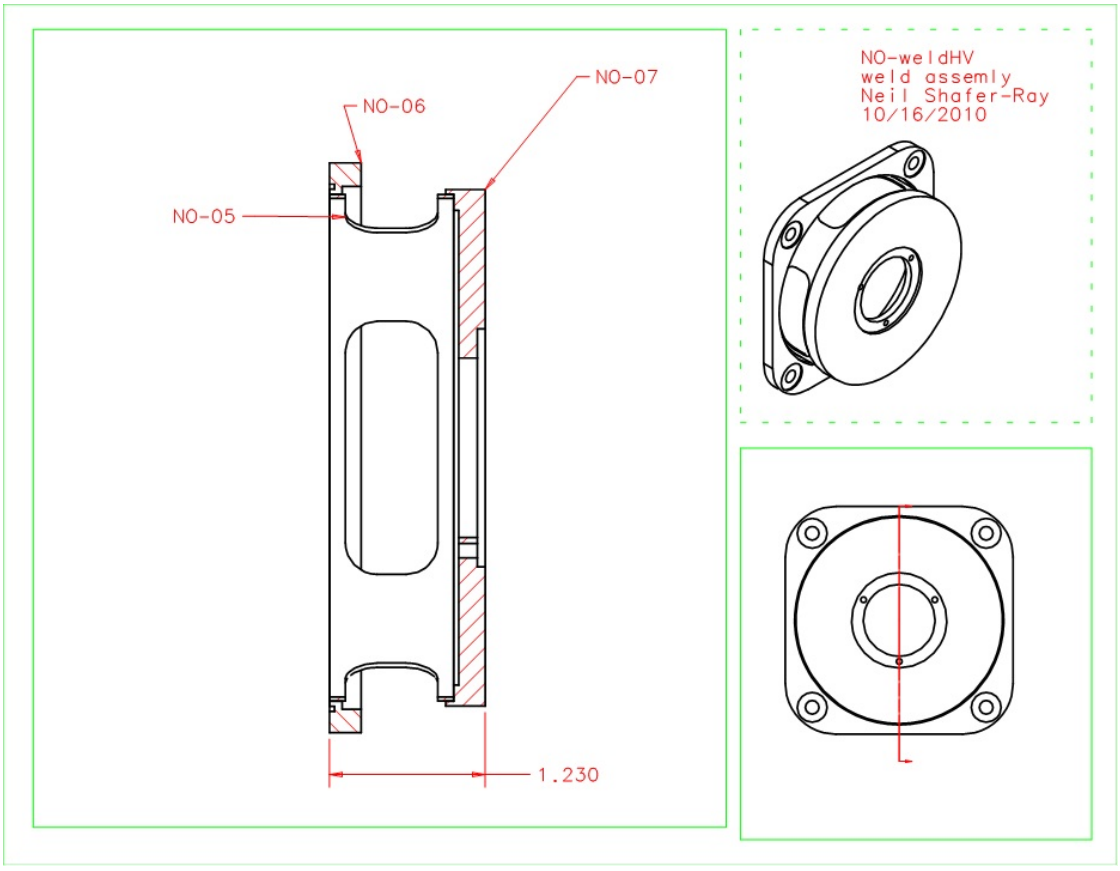
NO-06
NO-07
NO-05
1.230
NO-weldHV
weld assemly
Neil Shafer-Ray
10/16/2010

Neil Shafer-Ray
NO-01
modification to supplied
8 to 6
conflat flange
1 part required

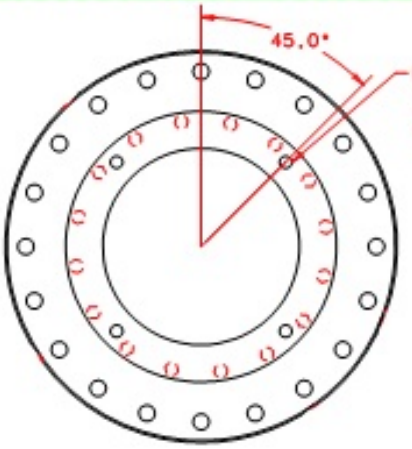

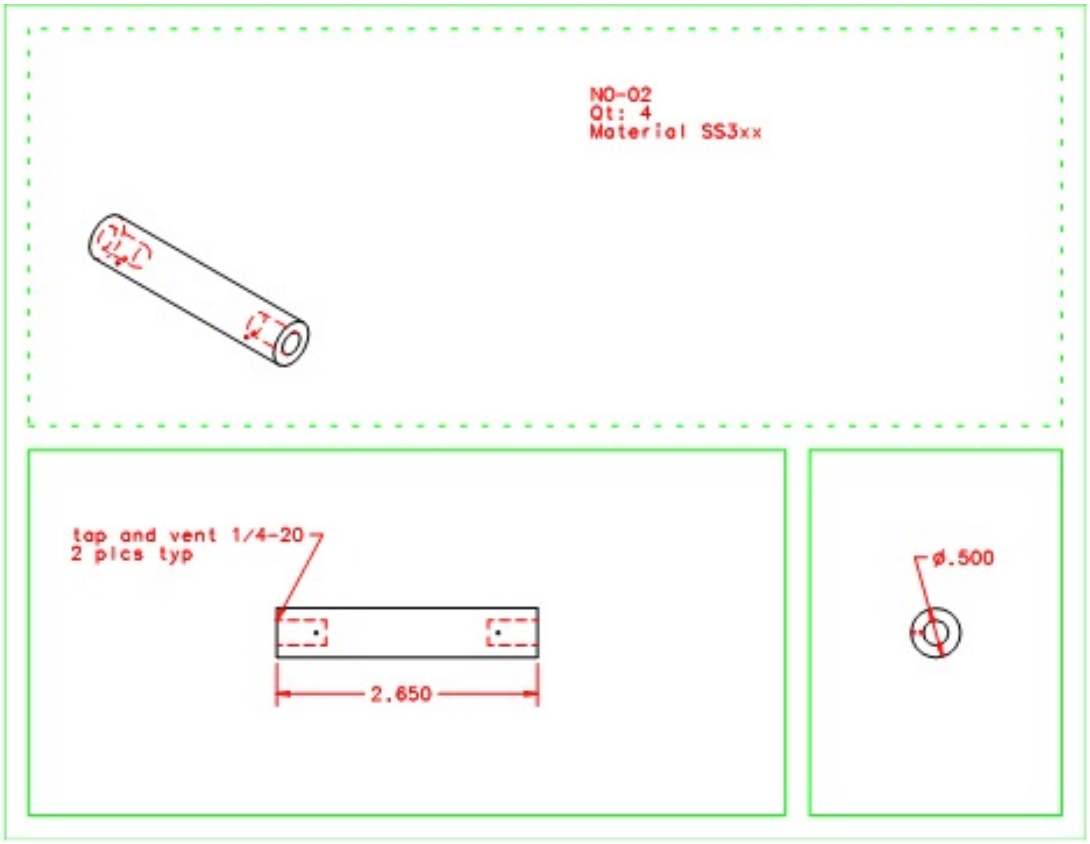
NO-02
Qt: 4
Material SS3xx
tap and vent 1/4-20
2 plcs typ
2.650
ø.500

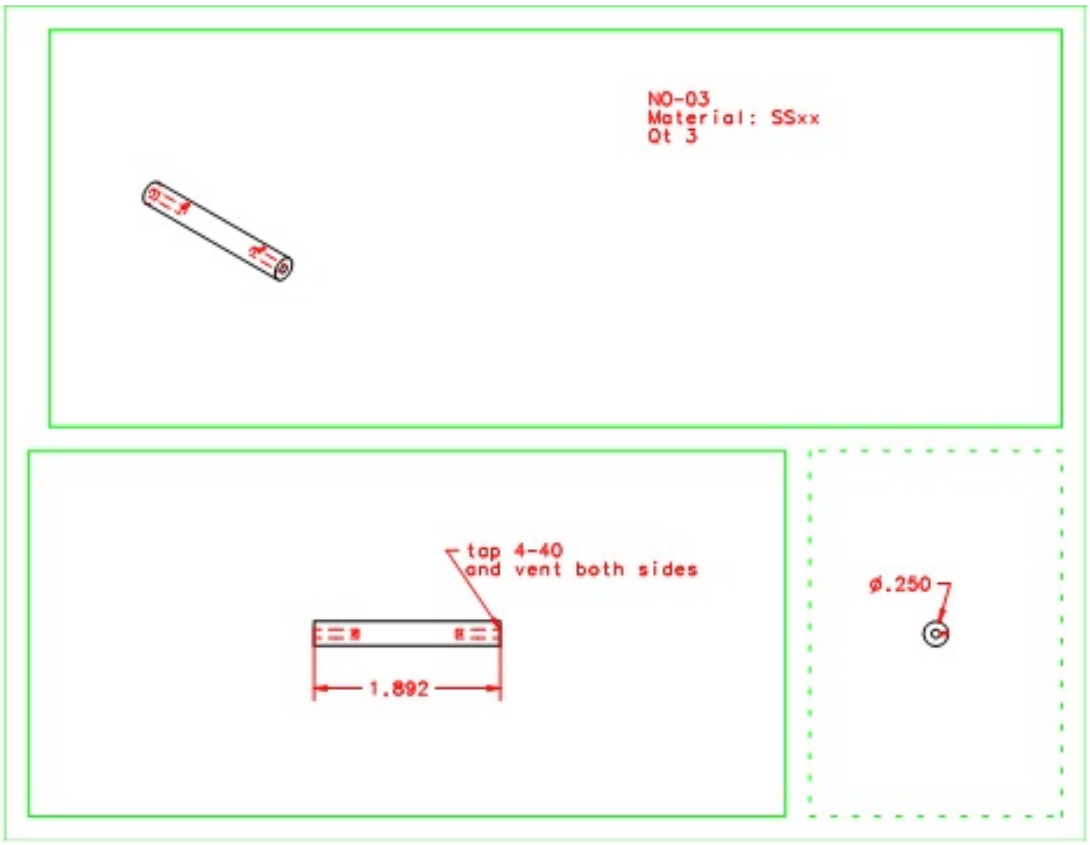
NO-03
Material: SSxx
Qt 3
tap 4-40
and vent both sides
1.892
ø.250

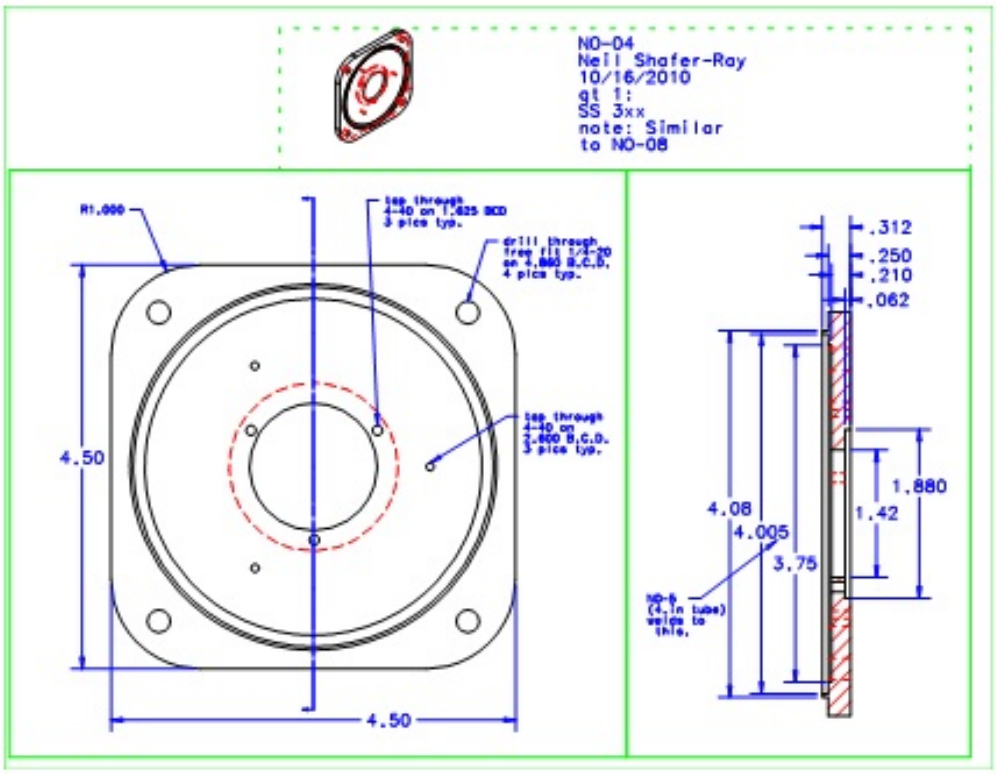
NO-04
Neil Shafer-Ray
10/16/2010
qt 1:
SS 3xx
note: Similar
to NO-08
R1.000
4.50
4.50
.312
.250
.210
.062
1.880
1.42
4.08
4.005
3.75

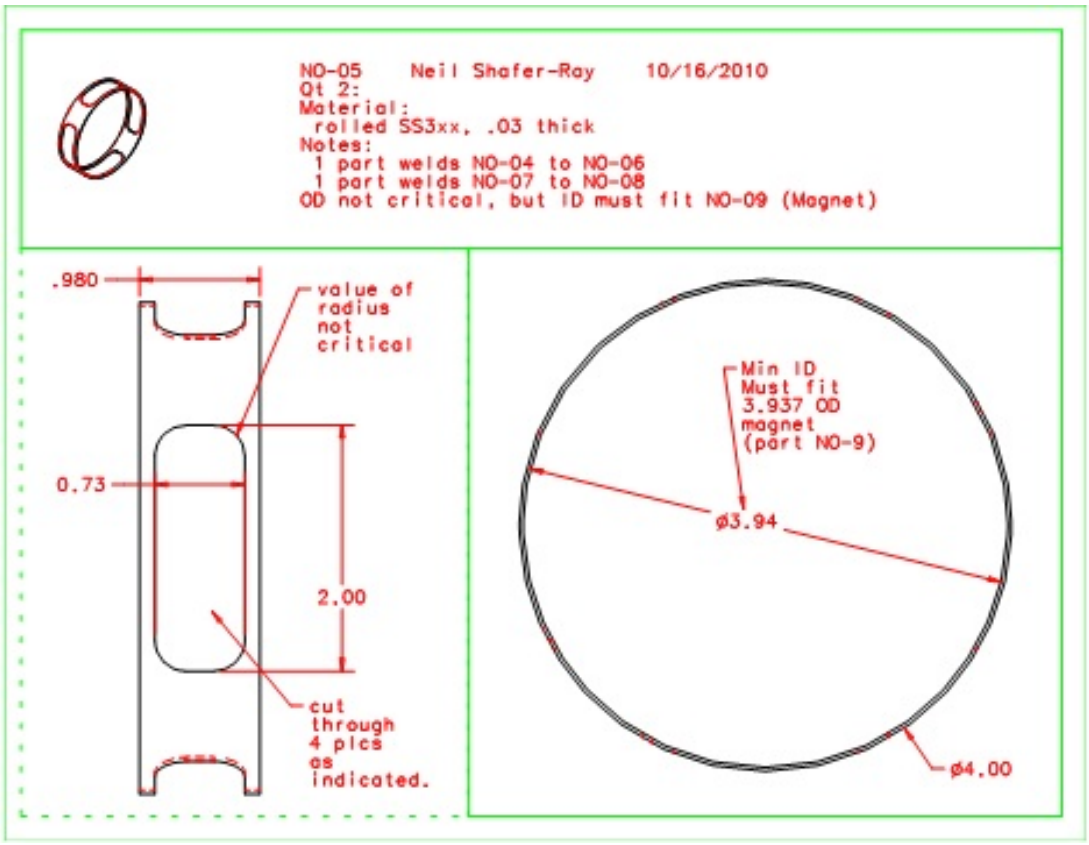
NO-05 Neil Shafer-Ray 10/16/2010
Qt 2:
Material:
rolled SS3xx, .03 thick
Notes:
1 part welds NO-04 to NO-06
1 part welds NO-07 to NO-08
OD not critical, but ID must fit NO-09 (Magnet)
.980
value of radius not critical
0.73
2.00
cut through 4 pics as indicated.
Min ID Must fit 3.937 OD magnet (part NO-9)
ø3.94
ø4.00

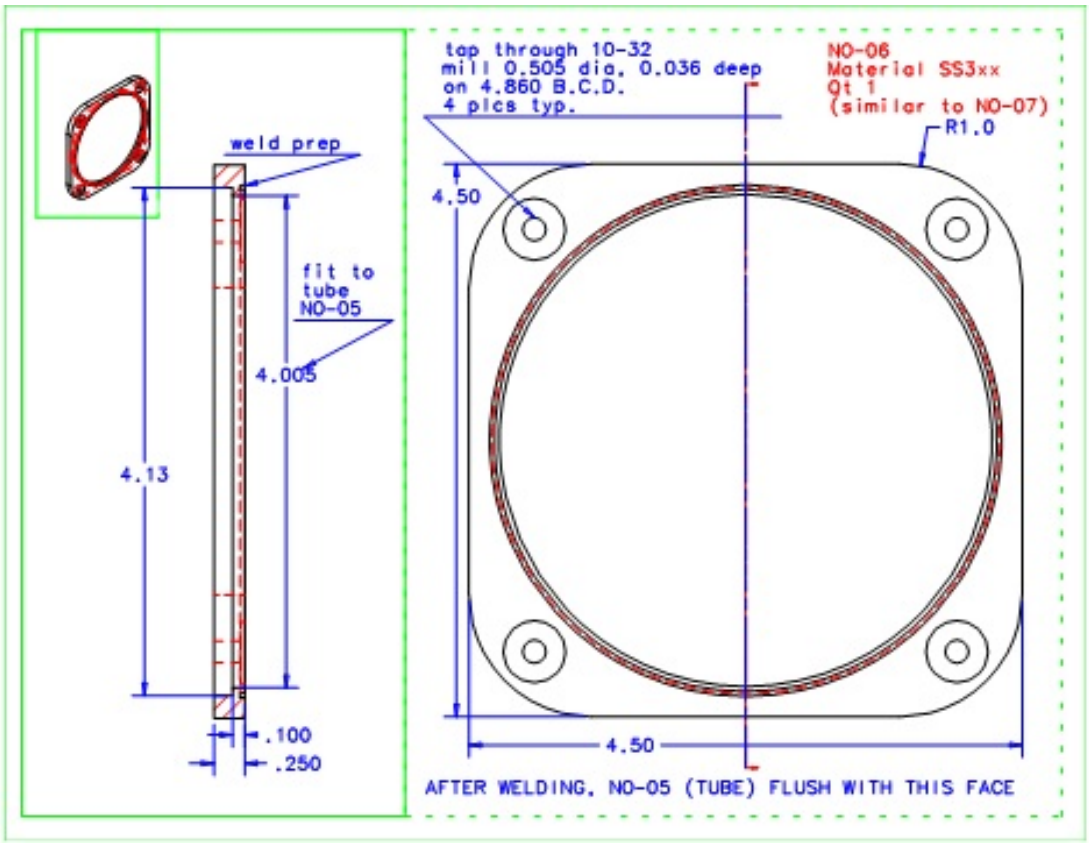
weld prep
fit to
tube
NO-05
4.005
4.13
.100
.250
tap through 10-32
mill 0.505 dia. 0.036 deep
on 4.860 B.C.D.
4 plcs typ.
NO-06
Material SS3xx
Qt 1
(similar to NO-07)
R1.0
4.50
4.50
AFTER WELDING, NO-05 (TUBE) FLUSH WITH THIS FACE

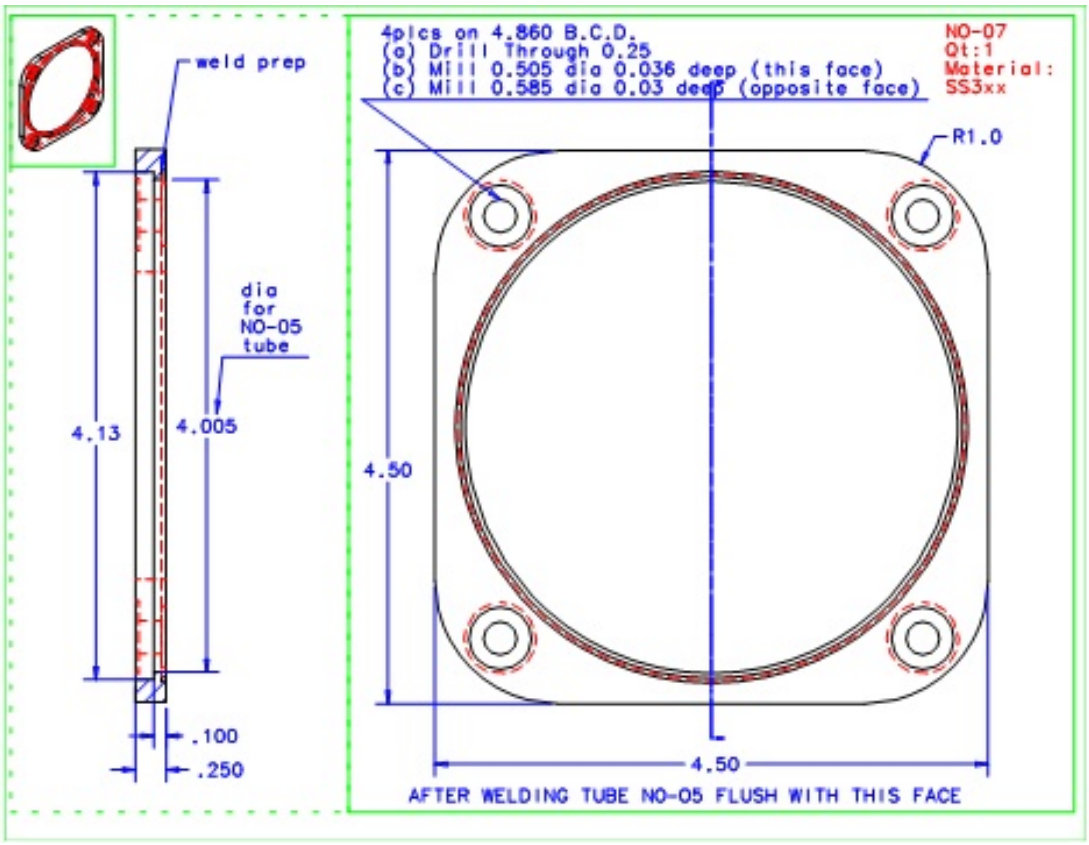
4plcs on 4.860 B.C.D.
(a) Drill Through 0.25
(b) Mill 0.505 dia 0.036 deep (this face)
(c) Mill 0.585 dia 0.03 deep (opposite face)
NO-07
Qt:1
Material:
SS3xx
weld prep
R1.0
dia
for
NO-05
tube
4.13
4.005
4.50
.100
.250
4.50
AFTER WELDING TUBE NO-05 FLUSH WITH THIS FACE

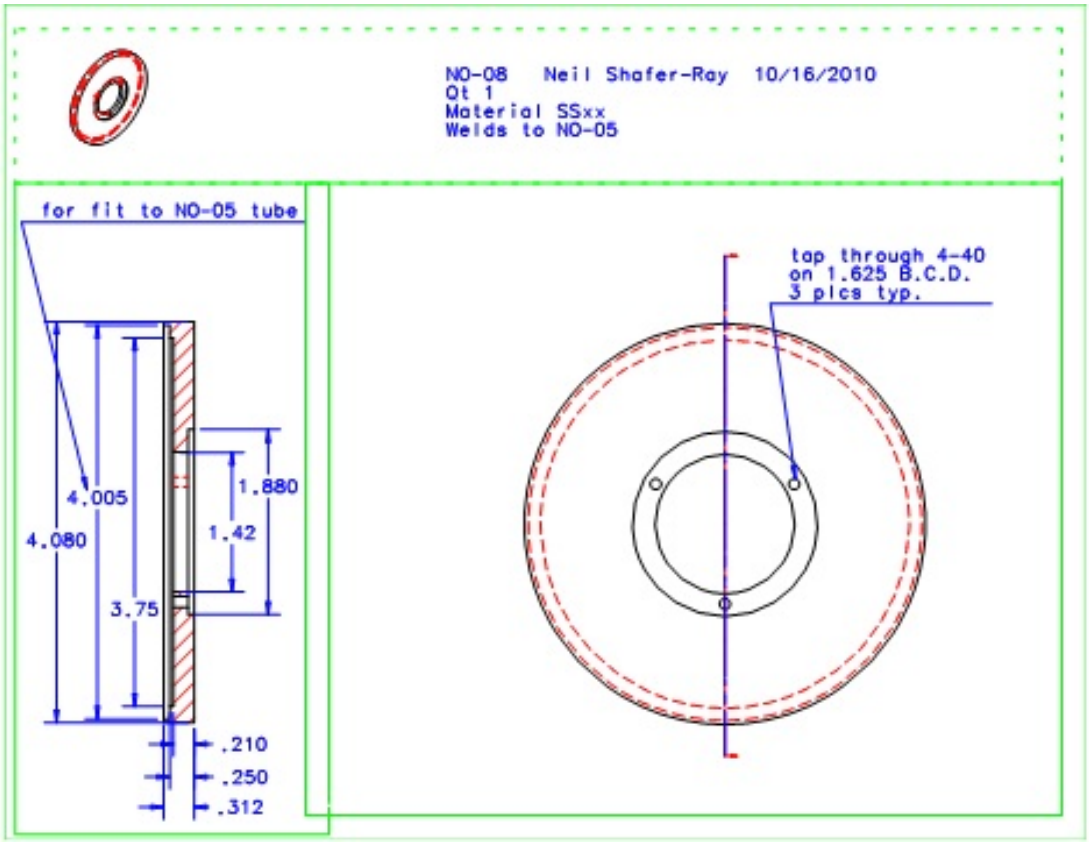
NO-08 Neil Shafer-Ray 10/16/2010
Qt 1
Material SSxx
Welds to NO-05
for fit to NO-05 tube
4.005
4.080
3.75
1.880
1.42
.210
.250
.312
tap through 4-40
on 1.625 B.C.D.
3 plcs typ.

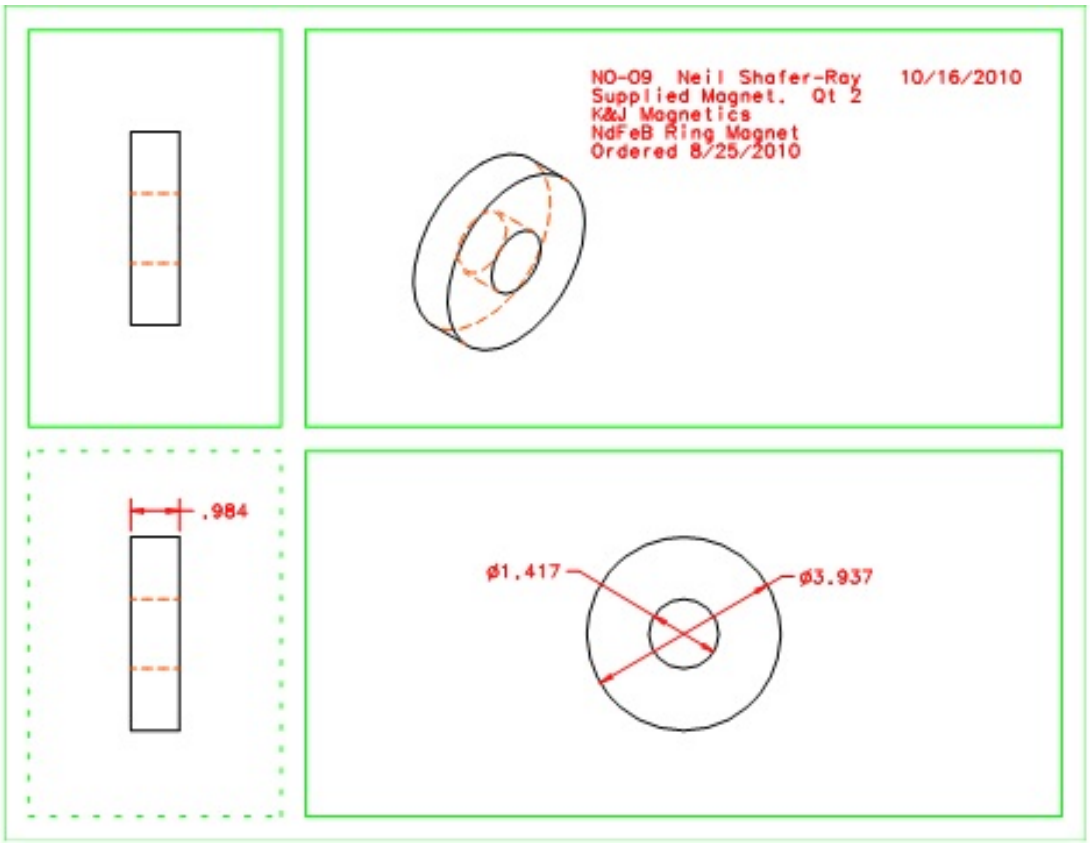
NO-09 Neil Shafer-Ray 10/16/2010
Supplied Magnet. Qt 2
K&J Magnetics
NdFeB Ring Magnet
Ordered 8/25/2010
.984
ø1.417
ø3.937

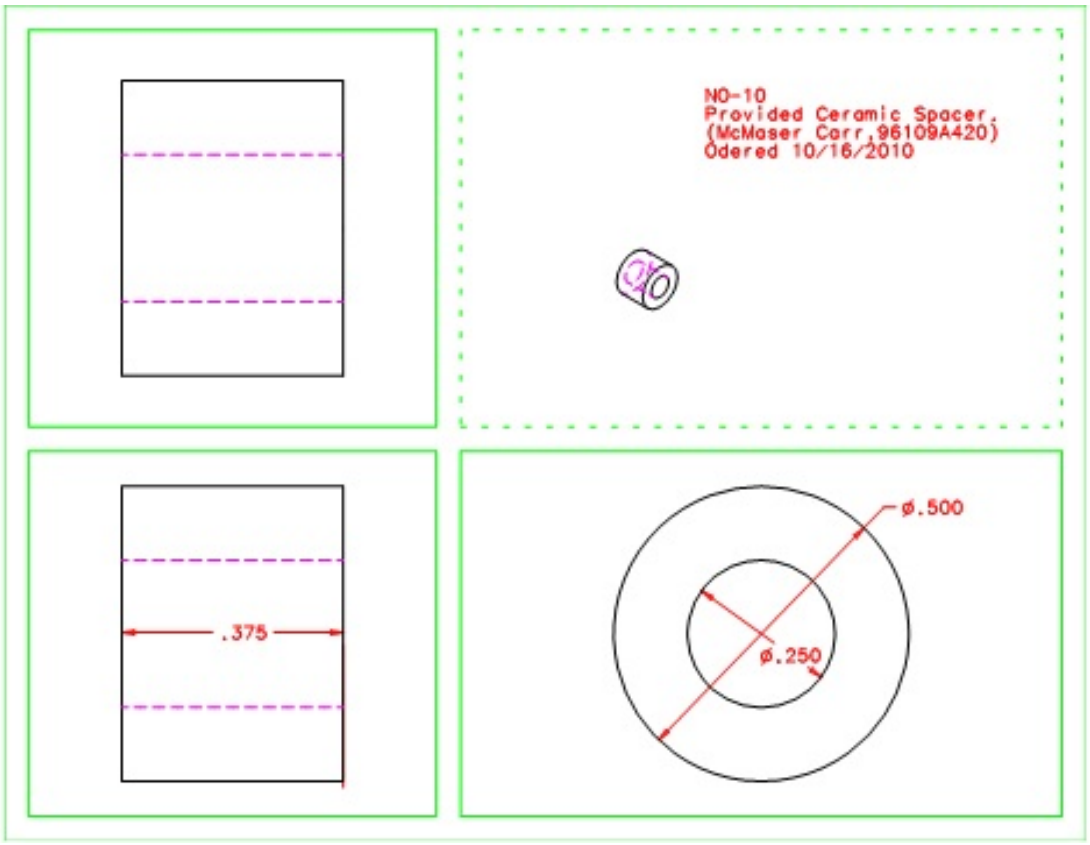
NO-10
Provided Ceramic Spacer,
(McMaser Carr,96109A420)
Odered 10/16/2010
.375
ø.500
ø.250

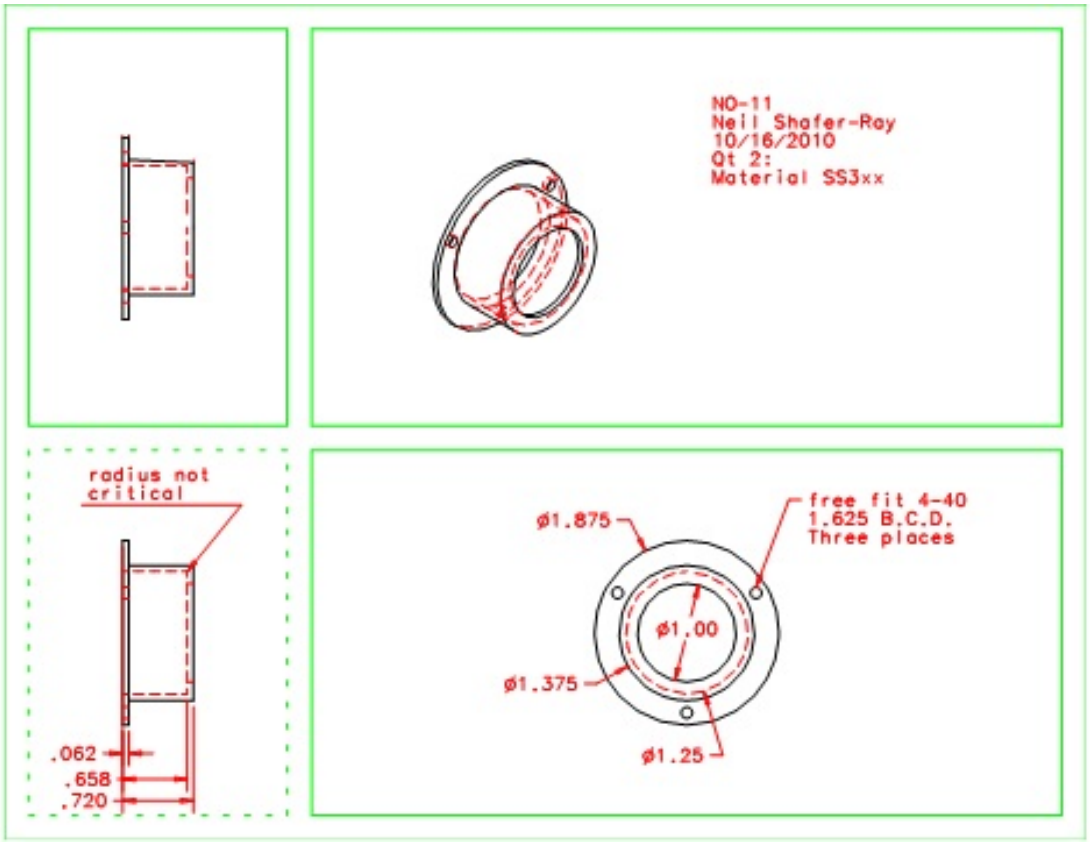
NO-11
Neil Shafer-Ray
10/16/2010
Qt 2:
Material SS3xx
radius not
critical
.062
.658
.720
ø1.875
free fit 4-40
1.625 B.C.D.
Three places
ø1.00
ø1.375
ø1.25

Appendix H

Machine drawing of the vacuum equipment

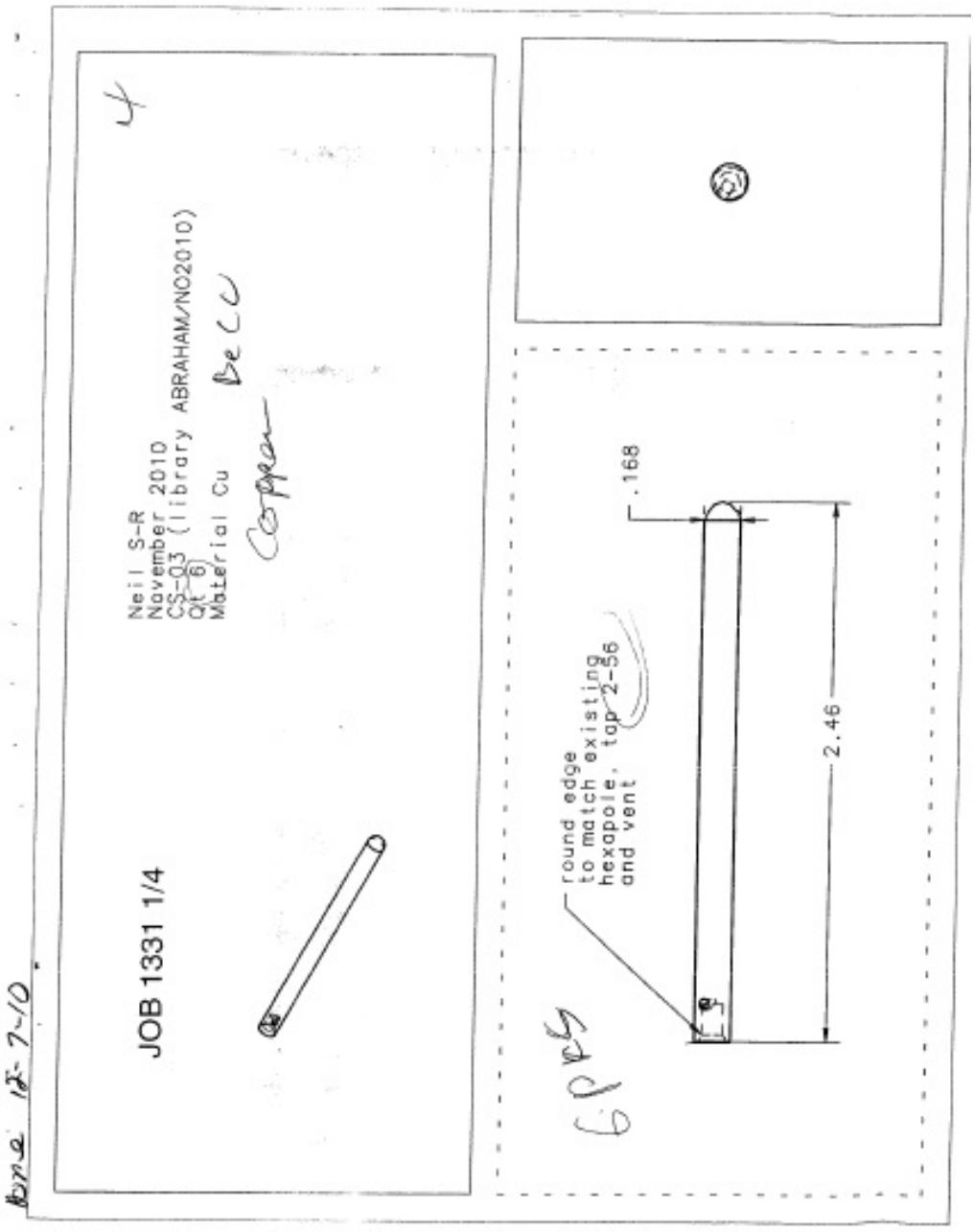

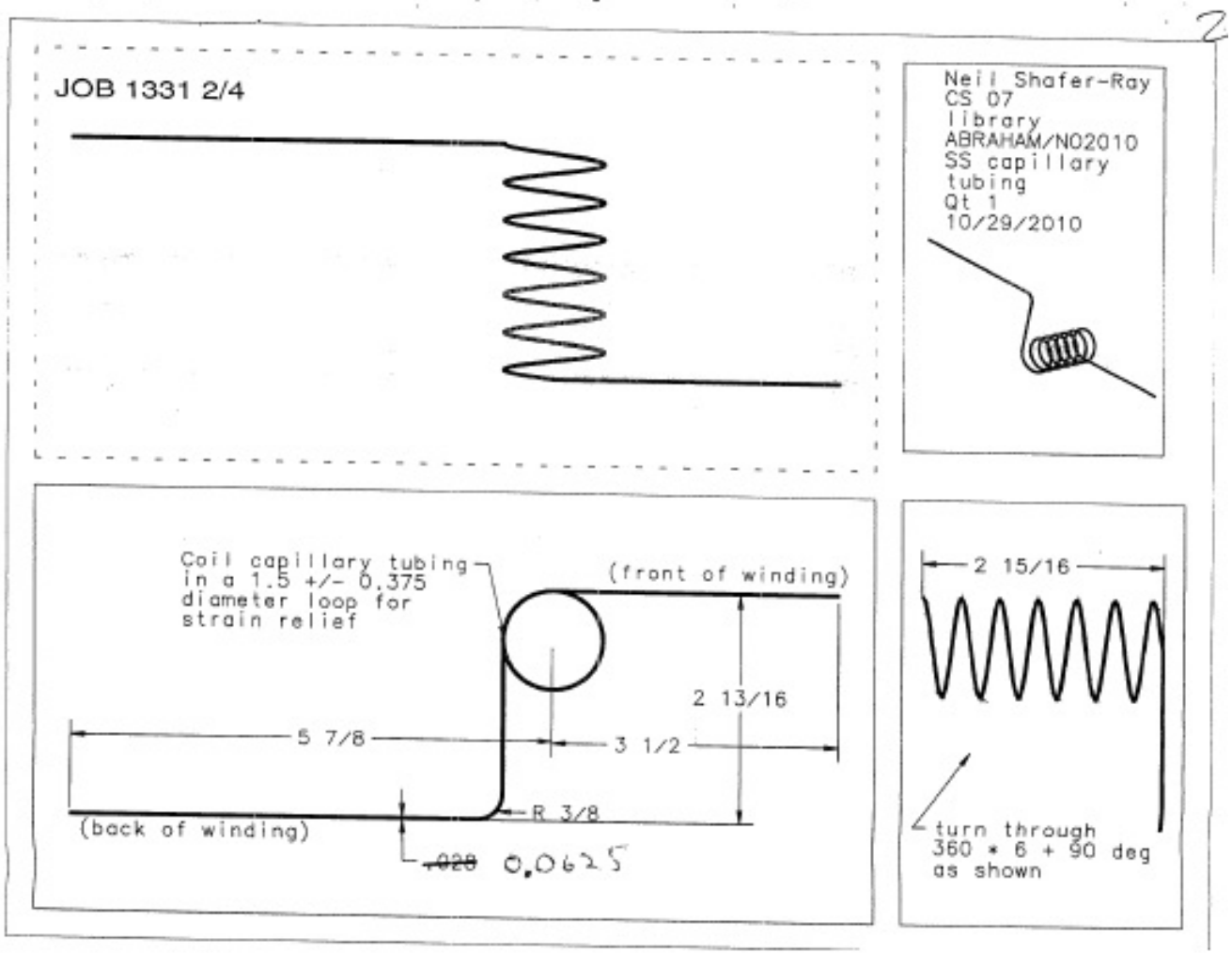
2
JOB 1331 2/4
Neil Shafer-Ray
CS 07
library
ABRAHAM/NO2010
SS capillary
tubing
Qt 1
10/29/2010
Coil capillary tubing
in a 1.5 +/- 0.375
diameter loop for
strain relief
(front of winding)
2 13/16
5 7/8
3 1/2
R 3/8
(back of winding)
+.020 0.0625
2 15/16
turn through
360 * 6 + 90 deg
as shown

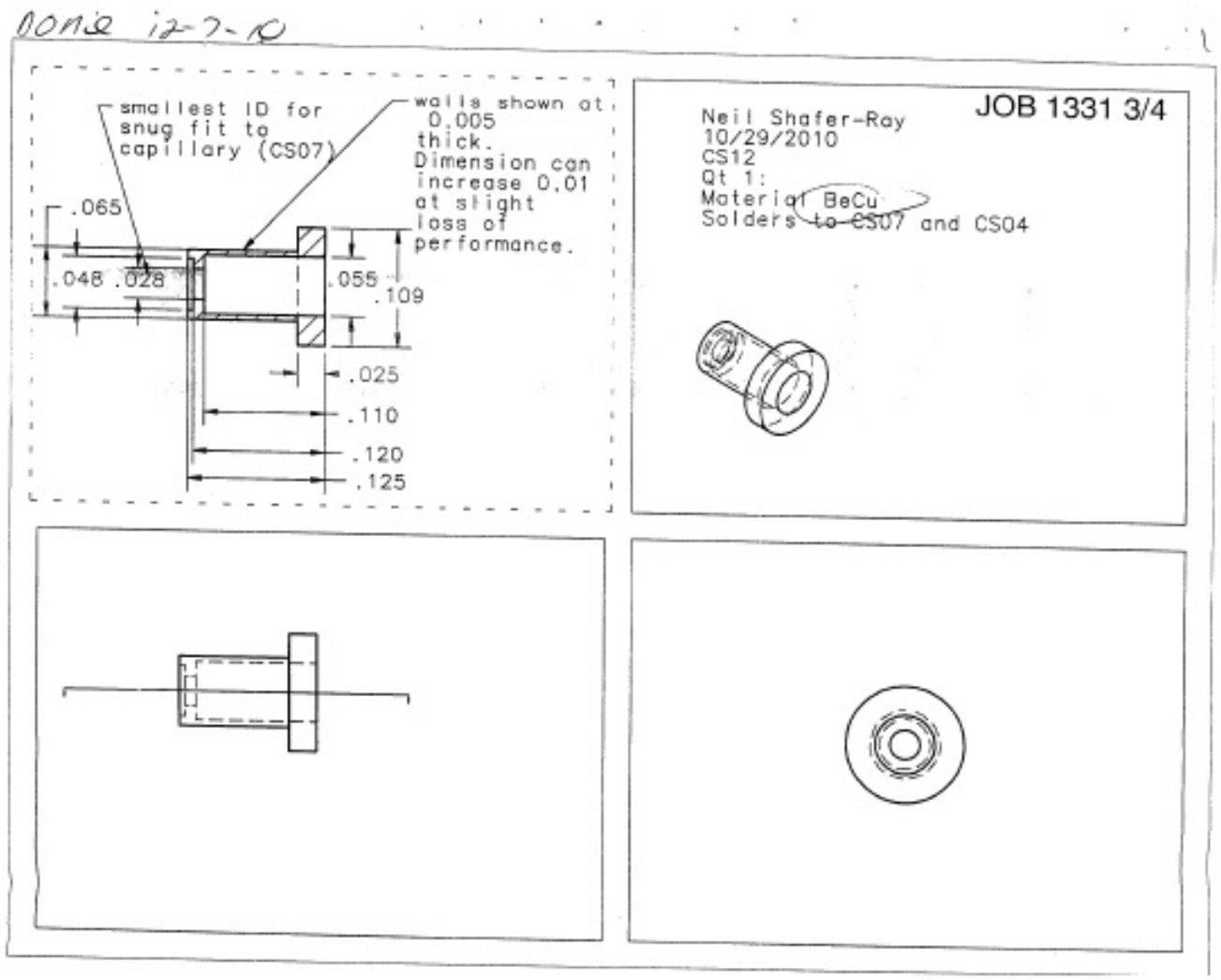
done 12-7-10
smallest ID for snug fit to capillary (CS07)
walls shown at 0.005 thick. Dimension can increase 0.01 at slight loss of performance.
.065
.048
.028
.055
.109
.025
.110
.120
.125
JOB 1331 3/4
Neil Shafer-Ray
10/29/2010
CS12
Qt 1:
Material BeCu
Solders to CS07 and CS04

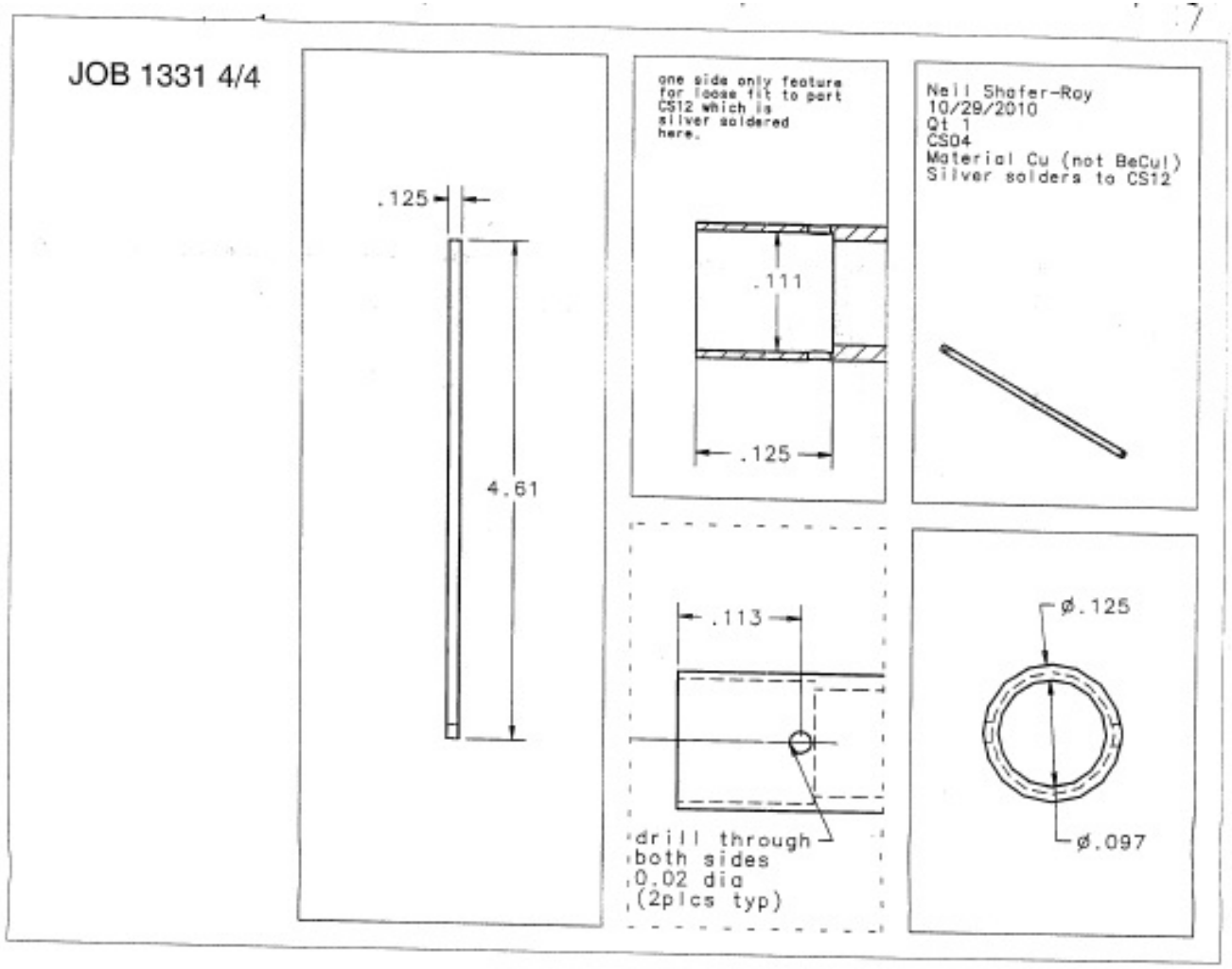
JOB 1331 4/4
.125
4.61
one side only feature for loose fit to part CS12 which is silver soldered here.
.111
.125
Neil Shafer-Roy
10/29/2010
Qt 1
CS04
Material Cu (not BeCu)
Silver solders to CS12
.113
drill through both sides .0.02 dia (2plcs typ)
ø.125
ø.097

apply silver solder to ensure electrical contact.
silver solder
CS07
CS12
CS04
glue provided TC wire and thread to back.
CS13 (provided currently soldered to old (long) version of CS04.)
CS04
4.600
CS04, CS07, CS12, CS13 and TC wire assembly.

Appendix I

Preprint ready for submission

Two preprints are ready for submission. One is related to the simulation of the Π state of neutral paramagnetic molecules such as NO in the hexapole guide and magnetic trap. It is also related to the simulation of the charged particles in the electromagnetic field to calculate the time of flight in the detection region. The other paper is related to the experimental production of the laserless source of cold molecules for further experiments such as buffer gas cooling and magnetic trapping.